Progress in Synthesis of Ferroelectric Ceramic Materials via High-Energy Mechanochemical Technique

L. B. Kong[a, *], T. S. Zhang[b, †], J. Ma[b] and Y. C. F. Boey[b]

[a]*Temasek Laboratories, National University of Singapore, 10 Kent Ridge Crescent, Singapore 119260*

[b]*School of Materials Science and Engineering, Nanyang Technological University, Nanyang Avenue, Singapore 639798*

Abstract

Ferroelectric ceramics are important electronic materials that have found a wide range of industrial and commercial applications, such as high-dielectric constant capacitors, piezoelectric sonar or ultrasonic transducers, pyroelectric security sensors, medical diagnostic transducers, electro-optical light valves, and ultrasonic motors, to name a few. The performances of ferroelectrics are closely related to the ways they are processed. The conventional solid state reaction method requires high calcination and sintering temperatures, resulting in the loss of lead, bismuth or lithium components due to their high volatilities, thus worsening the microstructural and subsequently the electrical properties of the ferroelectric materials. Various wet chemistry based routes have been developed to synthesize ultra-fine and even nano-sized ferroelectric powders. However, most of the chemistry based routes still involve calcinations, although at relatively lower temperatures. High energy mechanochemical milling process has shown that some ferroelectric materials can be synthesized directly from their oxide precursors in the form of nano-sized powders, without the need for the calcination at intermediate temperatures, thus making the process very simple. A large number of ferroelectric materials, including lead-containing ferroelectrics, antiferroelectrics and relaxors, and bismuth-containing Aurivillius families, have been synthesized by the high-energy milling process. Some ferroelectrics, such as barium titanate ($BaTiO_3$ or BT), lead iron tungstate [$Pb(Fe_{2/3}W_{1/3})O_3$ or PFW], and several bismuth-containing materials, that cannot be directly produced from their oxide mixtures, have been formed at relatively low temperatures. Ferroelectric ceramics derived from the activated precursors demonstrated better microstructure and electrical properties than those without mechanochemical treatment. This review presents an overview of the recent progress in the synthesis of ferroelectric ceramic powders using various high-energy milling techniques. The progress includes several aspects: (i) direct synthesis of nano-sized powders with better sinterability, (ii) promoted reactive sintering due to the modification of the precursors, (iii) amorphization of the precursors, and (iv) refinement of the precursors with high homogeneity. The underlying mechanisms of mechanochemical synthesis of ferroelectric materials are discussed. Further research emphasises on issues related to the synthesis of ferroelectric ceramic powders are suggested.

Keywords: Mechanochemical synthesis, ferroelectric ceramics, nano-sized powders, microstructure, sintering, calcination, grain growth, piezoelectricity, pyroelectricity, electro-optical, dielectric constant,

*Email: tslklb@nus.edu.sg, Tel: 65-65166910, Fax: 65-65166840

[†]Present address: Present address: Institute of Materials Research and Engineering, 3 Research Link, Singapore 117602

Contents

Nomenclature

AFE	Antiferroelectric
AFE_O	Antiferroelectric orthorhombic
BET	Brunauer-Emmett-Teller
BiM	Bismuth molybdate, Bi_2MoO_6
BiMW	Bismuth molybdate tungstate, $Bi_2Mo_{1-x}W_xO_6$
BiT	Bismuth titanate, $Bi4Ti_3O_{12}$
BiTN	Bismuth titanate niobate, Bi_3TiNbO_9
BiV	Bismuth vanadate, $Bi_2VO_{5.5}$
BST	Barium strontium titanate, $Ba_{1-x}Sr_xTiO_3$
BT	Barium titanate, $BaTiO_3$
CBiT	Calcium bismuth titanate, $CaBi_4Ti_4O_{15}$
$d_{33,}\, d_{31}$	Piezoelectric coefficient
D_0	Initial grain size
DTA	Differential thermal analysis
D_t	Grain size at time *t*
E_C	Coercive electric field
EPR	Electron paramagnetic resonance
FE	Ferroelectric
FE_{Rh}	Ferroelectric rhombohedral
FE_{Tet}	Ferroelectric tetragonal
K_p	Planar coupling coefficient
LN	Lithium niobate, $LiNbO_3$
MPB	Morphotropic phase boundary
n	Exponential coefficient of grain growth
NN	Sodium niobate, $NaNbO_3$
PE	Paraelectric
PE_{Cubic}	Paraelectric cubic
PFN	Lead iron niobate, $Pb(Fe_{1/2}Nb_{1/2})O_3$
PFW	Lead iron tungstate, $Pb(Fe_{2/3}W_{1/3})O_3$
PT	Lead titanate, $PbTiO_3$
PLT	Lead lanthanum titanate, $Pb_{1-x}La_xTiO_3$
PLZST	Lead lanthanum zirconate stannate titanate, $Pb_{0.97}La_{0.02}(Zr_{0.65}Sn_{0.31}Ti_{0.04})O_3$
PLZT	Lead lanthanum zirconate titanate, $(Pb_{1-y}La_y)(Zr_{1-x}Ti_x)O_3$
PMN	Lead magnesium niobate, $Pb(Mg_{1/3}Nb_{2/3})O_3$
PMW	Lead magnesium tungstate, $Pb(Fe_{1/2}W_{1/2})O_3$
PNZST	Lead lanthanum zirconate stannate titanate, $Pb_{0.99}Nb_{0.02}(Zr_{0.85}Sn_{0.13}Ti_{0.02})_{0.98}O_3$
PST	Lead scandium tantalate, $Pb(Sc_{1/2}Ta_{1/2})O_3$
PZ	Lead zirconate, $PbZrO_3$

P_r	Remanent polarization
P_s	Saturation polarization
PZN	Lead zinc niobate, $Pb(Zn_{1/3}Nb_{2/3})O_3$
PZT	Lead zirconate titanate, $Pb(Zr_{1-x}Ti_x)O_3$
RFE	Relaxor ferroelectric
SBiN	Strontium bismuth niobate, $SrBi_2Nb_2O_9$
SBiT	Strontium bismuth titanate, $SrBi_4Ti_4O_{15}$
SBT	Strontium bismuth tantalate, $SrBi_2Ta_2O_9$
SEM	Scanning electron microscopy
SPS	Spark plasma sintering
ST	Strontium titanate, $SrTiO_3$
T_C	Curie temperature
TEM	Transmission electron microscopy
TGA	Thermal gravity analysis
TMA	Thermal mechanical analysis
XRD	X-ray diffraction

1. Introduction

1.1. Ferroelectrics

To understand the definition of ferroelectricity, it is necessary to mention piezoelectricity and pyroelectricity because they have interesting relationship in terms of crystal structures. All crystals can be categorized into 32 different classes, i. e. pints groups divided by using the symmetry elements: (i) center of symmetry, (ii) axies of rotation, (iii) mirror planes and (iv) several combinations of them. The 32 pint groups are subdivisions of seven basic crystal systems that are, in order of ascending symmetry, triclinic, monoclinic, orthorhombic, tetragonal, rhombohedral (trigonal), hexagonal and cubic. 21 classes of the 32 point groups are noncentrosymmetric, which is a necessary condition for piezoelectricity to exist. 20 of them are piezoelectric. Of the 20 piezoelectric crystal classes, 10 crystals are of pyroelectric properties. Within a given temperature range, this group of materials is permanently polarized. Compared to the general piezoelectric polarization produced under stress, the pyroelectric polarization is developed spontaneously and kept as permanent dipoles in the structure. Because this polarization varies with temperature, the response is termed as pyroelectricity. Ferroelectric group is a subgroup of the spontaneously polarized pyroelectric crystals. On one hand, the polarization of ferroelectric is similar to the polarization of pyroelectric. On the other hand, there is difference between the two polarizations because the ferroelectric polarization is reversible by an external applied electric field, provided that the applied field is less than the dielectric breakdown of the materials. Therefore, materials that can be defined as ferroelectrics must have two characteristic: the presence of spontaneous polarization and reversibility of the polarization under electric field [1, 2].

In the group of ferroelectric materials, there are four subcategories: perovskite group, pyrochlore group, tungsten-bronze group and bismuth layer structure group, among which the perovskite group is the most important and thus the most widely studied. Perovskite is usually expressed as ABO_3. A typical ABO_3 unit-cell structure is shown in Fig. 1, taking $PbTiO_3$ as an example [1, 2]. It consists of a corner-linked network of oxygen octahedra, creating an octahedral cage (B-site) and the interstices (A-sites). Ti^{4+} ions occupy the B-site while Pb^{2+} ions occupy the A-site. Fig. 1 also shows the paraelectric and ferroelectric states of $PbTiO_3$. Most ferroelectric materials undergo a structural phase transition from a high temperature paraelectric phase into a low temperature ferroelectric phase. The paraelectric phase always has a higher symmetry than the ferroelectric phase. The temperature of the phase transition is called as the Curie temperature (T_C). Different ferroelectric materials have different values of T_C, which can be either lower than liquid nitrogen (LN) temperature or higher than 1000 ℃. For a given material (composition), the T_C is closely related to microstructure (grain size and distribution, density, porosity and pore size and distribution, and impurity, and so on). Generally, the T_C of a given material decreases with decreasing grain size [54]. The phase transition of ferroelectrics often leads to strong anomalies in dielectric, elastic, thermal and other properties of the materials, among which dielectric variation before and after a phase transition is the most significant and thus usually used as an indication of phase transition [143].

In the ferroelectric state, the ability of displacement of the central Ti^{4+} ion is the causes the reversibility of polarization. The switch of many adjacent unit cells is referred to as domain reorientation or switching. The homogeneous areas of the material with the same polarization orientation are referred to as domains, with domain walls existing between areas of unlike polarization orientation [1, 2]. For ferroelectric ceramics, the domains are randomly oriented and thus the net polarization of materials is zero because of their cancellation

effect. Therefore, the as-prepared ferroelectric ceramics are neither piezoelectric nor pyroelectric. To show piezoelectric and pyroelectric properties, polycrystalline ferroelectric ceramics must be poled at a strong external DC electric field (10-100 kV/cm). Poling is to electrically align the orientation of the randomly distributed domains within the grains and to make ferroelectric ceramics act like a single crystal possessing both ferroelectric and piezoelectric properties. Poling is usually conducted at elevated temperatures, because polarization would be more compliant at high temperatures [1, 2].

1.2. Brief history of ferroelectrics and ferroelectric ceramics

The history of ferroelectrics can be tracked back to Rochelle salt (sodium potassium tartrate tetrahydrate, $KNa(C_4H_4O_6)\cdot 4H_2O$), which was synthesized more than 400 years ago, initially for medicinal purpose. It is n this same crystalline material that pyroelectric (thermal-polar), piezoelectric (stress-polar) and ferroelectric were discovered subsequently. Before this discovery, ferroelectricity was only a hypothetical property of solid materials at the turn of the 20^{th} century. However, the practical application of this material is largely limited due to its water solubility. It was after the discovery of ferroelectric ceramics (barium titanate, BaTiO3), this class of materials became extremely useful for a variety applications.

The first ferroelectric ceramic material is barium titanate ($BaTIO_3$ or BT), which was discovered in the mid-1940s [1, 2, 249]. Before the discovery of $BaTiO_3$, the most widely used materials for capacitors were steatite, mica, TiO_2, $MgTiO_3$ and $CaTiO_3$, with dielectric constant of $\leq$100. During the World War II, there was pressing needs for high dielectric constant materials to fabricate high capacitance capacitors. Before publication was available in the literature, $BaTiO_3$ has already been studied as a high dielectric constant material concurrently. In the later open publications, it was concluded that the source of the high dielectric constant in $BaTiO_3$ is due to its ferroelectric properties [1].

The history of ferroelectric ceramics also includes the report of lead zirconate titanate ($PbZr_{1-x}Ti_xO_3$, or PZT) piezoelectric ceramics, the development of transparent electro-optical lead lanthanum zirconate titanate ($Pb_{1-x}La_xZr_{1-y}Ti_yO_3$, or PLZT), the research on lead magnesium niobate ($PbMg_{1/3}Nb_{2/3}O_3$, or PMN) relaxor ferroelectric ceramics and the discovery of many other non-perovskite ferroelectric ceramics. For more details, the readers are referred to Refs [1, 249] and literatures therein.

Ferroelectric ceramics have been found to be useful for various practical applications, such as high dielectric constant capacitors, piezoelectric sonar and ultrasonic transducers, radio and communication filters, pyroelectric devices, medical diagnostic transducers, positive temperature coefficient (PTC) sensors, ultrasonic motors and electroopitic light valves, to name a few [1, 2].

1.3. Properties of ferroelectric ceramics

1.3.1. Microstructure

Microstructure refers to density, grain shape, grain size and distribution, porosity, pore size and distribution and sometimes anisotropic grain growth (texture).

Fully dense ferroelectric ceramics (>95% of theoretical density) are required by most applications, which is because of several reasons. Firstly, a full densification of ferroelectric ceramics ensures to achieve the maximized performance. For example, the dielectric constant of ferroelectric ceramics usually increases with increasing density. This is because the relative dielectric constant of pores/vacuums is unit. Secondly, the presence of pores is generally a cause of high loss tangent, since porosity could form provide conduction path for electricity and thus could be a main contribution to dielectric loss tangent, as conduction loss. Moreover,

electrical conduction caused by porosity is also responsible for degraded electrical breakdown strength. Optical properties of transparent ferroelectric ceramics are extremely sensitive to porosity. Pores reduced the transparency of ferroelectric ceramics by acting as scattering centers. Finally, mechanical strength, sometimes a critical requirement for some specific applications, such as piezoelectric actuators and actuators, is directly determined by the density of the materials used.

Generally, the densities of ferroelectric ceramics increase with increasing sintering temperature. However, too high temperature is not suitable for lead- and bismuth containing ferroelectric materials, which is due the volatility characteristic of lead and bismuth. High temperature also leads to abnormal grain growth (secondary grain growth). The presence of exaggeratedly grown grains is harmful to the performance for most ferroelectric ceramics. To effectively enhance the densification of ferroelectric ceramics at relatively low temperatures, various attempts have been made and have been widely reported in the literature. The main strategies that have been employed to reduce the sintering temperature of ferroelectric ceramics are the use of fine/ultrafine powders and the addition of sintering aids. Fine/ultrafine powders can be synthesized by various wet-chemical methods, as discussed later. Sintering aids are required to have relatively low melting points and no reaction with ferroelectric phases during sintering process.

Grain size is another important factor that determines the properties, such as dielectric constant, tetragonality (c/a ratio), phase transition temperature (T_C), polarization, piezoelectric and pyroelectric coefficients, of ferroelectric ceramics [5, 54]. The variation in grain size with sintering temperature is similar to that of density, i. e. grain size increases with increasing sintering temperature. There is a critical grain size for most ferroelectric ceramics below which many properties, such as piezoelectric and pyroelectric, can be well developed. There is also a critical grain size beyond which most properties are saturated, i. e. the properties of ferroelectric materials do not always increase with grain size. Both critical sizes are depending on types of materials or compositions of given materials. In contrast to many other ferroelectrics, there is an anomalously high dielectric constant for $BaTiO_3$ ceramics of fine grains, which has not been fully understood till now. Several models, including the presence of internal stresses in fine-grained ceramics, which are due to the absence of 90 ° domain walls, increased domain-wall contributions to the dielectric response in fine-grained ceramics, and shifts of the phase transition temperatures with grain size, have been suggested to explain this phenomenon [2, 5, 172].

1.3.2. Electrical and optical properties

1.3.2.1. Dielectric constant

Ferroelectric ceramics are characterized by (i) high dielectric constant (200-10,000) [1, 62-70] compared to ordinary insulating materials (5-100), (ii) relatively low dielectric loss tangent (0.1%-7%), (iii) high DC resistivity, (iv) moderate dielectric breakdown strength (100-120 kV/cm) and (v) nonlinear electrical, electromechanical and electro-optic behavior.

1.3.2.2. P-E hysteresis loops

The polarization versus electric field (P-E) hysteresis loop is one of the most important electrical characteristic of ferroelectric ceramics. Because the hysteresis loop of ferroelectric materials is similar to the magnetic loop (magnetic versus magnetic field) of ferromagnetic materials, the term ferroelectric follows the name ferromagnetic, although iron is not a major component of ferroelectric materials.

Hysteresis loops come in various sizes and shapes, which can be used to identify the materials. Typical hysteresis loops include (i) linear tracing from a capacitor [1], (ii) highly nonlinear loop from a low-coercive

field memory ferroelectric (e. g. the rhombohedral region of the PZT phase diagram) [1], (iii) slim-loop of ferroelectric quadratic relaxor [1, 96, 98] and (iv) double loop of antiferroelectric materials [1, 113].

Hysteresis loops can provide a plentiful amount of information for the understanding of ferroelectric materials [1]. For example, the materials with a square-like P-E loop have memory ability. A high remanent polarization is related to high internal polarizability, strain, electromechanical coupling, and electrooptic activity. For a given material, the coercive field (E_c) is an indication of the grain size the material (i.e., lower E_c means larger grain size and higher E_c means smaller grain size). A high degree of loop squareness usually indicates better homogeneity and uniformity of grain size of materials. For relaxor ferroelectric materials, the high induced polarization means high electrostriction strain and high electrooptic coefficients. A sudden large change in "apparent" polarization is usually an indication of incipient dielectric breakdown.

1.3.2.3. Piezoelectric and electrostrictive properties

The word "piezoelectricity" is derived from the Greek "*piezein*", which means to squeeze or press. Piezoelectric properties of ferroelectric ceramics are important for many applications [1, 2, 66]. Two effects are operative in ferroelectric ceramics in terms of piezoelectric property. The direct effect (designated as a generator) is identified with the phenomenon whereby electrical charge (polarization) is generated from a mechanical stress, whereas the converse effect (designated as a motor) is associated with the mechanical movement generated by the application of an electrical field. The piezoelectric properties of ferroelectric ceramics are characterized by k_p, k_{33}, d_{33}, d_{31} and g_{33}.

The k factors (e.g., k_{33}, k_{31} and k_p) called piezoelectric coupling factors, are convenient and direct measurements of the overall strength of the electromechanical effects, i.e., the ability of the ceramic transducer to convert one form of energy to another. They are defined as the square root of the ratio of energy output in electrical form to the total mechanical energy input (direct effect), or the square root of the ratio of the energy available in mechanical form to the total electrical energy input (converse effect). Because the conversion of electrical to mechanical energy (or vice versa) is always incomplete, k is always less than unity. Commonly used as a figure-of-merit for piezoelectrics, the higher k values are most desirable and constantly sought after in new materials. For ceramics, k_p is a typical measure used to compare piezoelectric properties of ferroelectric materials–values ranging from 0.35 for $BaTiO_3$ to as high as 0.72 for PLZT [1].

The d coefficients are called piezoelectric coefficients and usually expressed as $\times 10^{-12}$ C/N (or pC/N) for the direct effect and $\times 10^{-12}$ m/V (or pm/V) for the converse effect. d_{31} indicates that this piezoelectric coefficient relates to the generation of polarization (direct effect) in the electrodes perpendicular to the vertical direction (3) and to the stress mechanically applied in the lateral direction (1); while d_{33} indicates the polarization generated in the vertical direction (3) when the stress is applied in the same direction.

g factors are called open-circuit coefficients, another parameters used to evaluate piezoelectric ceramics for their ability to generate large amounts of voltage per unit of input stress. The g constant is related to d constant: $g = d / K\varepsilon_0$ (K is relative dielectric constant and ε_0 is the dielectric constant of free space). High-g-constant ceramics are usually ferroelectrically hard materials that do not switch their polarization readily and possess lower K values.

1.3.2.4. Pyroelectric properties

Pyroelectric effects of ferroelectric materials are manifested in a change in polarization as a function of temperature [1, 2, 188], which results in a reduction of the bound charge required for compensation of the reduced dipole moment on increasing temperature and vice versa on decreasing temperature. The change in voltage on the material's electrodes is a measure of the change in the material's polarization due to absorbed thermal energy. A common figure-of-merit (*FOM*) for pyroelectrics is $FOM = \frac{p}{c(K \tan\delta)^{1/2}}$ (where *p* is the pyroelectric charge coefficient, *c* the specific heat, *K* the dielectric constant and tanδ the dielectric loss tangent). To maintain a high performance, ferroelectric ceramics selected should have a high pyroelectric coefficient and low specific heat, dielectric constant and dielectric loss factor. The most important ferroelectric ceramics that have promising pyroelectric properties are PZT and BST (barium strontium titanate) materials. Besides, PLZT and PMN are also considered viable candidates. The former two materials are considered ferroelectric thermal detectors (absorbed energy generating the temperature dependent change in polarization), whereas the latter two, as well as BST, can be considered dielectric bolometers (electrically induced, temperature-dependent change in dielectric constant materials). Due to their lower cost, availability, ease of processing and good stability, ferroelectric ceramics are considered better choices for thermal imaging applications when compared with crystalline materials, which although have higher pyroelectric coefficients. Ferroelectric ceramics, either in bulk or thin-film forms, are being used in commercial products for law-enforcement, night surveillance, and security applications [1].

1.3.2.5. Optical and electro-optic properties

A special group of ferroelectric ceramics is transparent PLZT ceramics. Optical transparency of a transparent PLZT ceramic is determined by both the concentration of lanthanum and the ratio of Zr/Ti, with a maximum in transparency occurring along the FE-PE phase boundary and beyond [1, 84-96]. Four types of electrooptic effects have been found to be operative in transparent ferroelectric ceramics. They include (i) quadratic, Kerr, and birefringent effects, (ii) depolarization nonmemory scattering, (iii) linear, Pockels, and birefringent effects, and (iv) memory scattering. The first two types utilize relaxor-type, 9/65/35 materials with linearly polarized light; the third type uses a high coercive field, tetragonal, memory material, such as 12/40/60, with polarized light; and the fourth type commonly uses a low coercive field, rhombohedral, memory material, such as 7/65/35, and does not use polarizers, but, rather, relies on the variable-angle scattering of light from different polarized areas to achieve a spatially varying image in the ceramic. Photosensitive phenomena related to the optical properties of transparent ferroelectric ceramics include (i) photoconductivity, (ii) photovoltaic properties, (iii) photo-assisted domain switching, (iv) ion-implantation enhanced photosensitivity, (v) photochromic effects, (vi) photomechanical (photostrictive) behavior, (vii) photorefractive effects, and (viii) photoexcited space charge behavior. Many new applications can be realized due to these special properties of transparent ferroelectric ceramics [1].

1.4. Processing of ferroelectric powders and ceramics

It is well known that materials' performances are closely related to the ways they are processed. Synthesis method of ferroelectric powders has played a significant role in determining the microstructural, electrical and optical properties of ferroelectric ceramics [3-5]. Ferroelectric powders were conventionally synthesized via a solid-state reaction process, using constituent oxides as the starting materials. Due to their

relatively rough grains, these powders require relatively high sintering temperature to obtain ferroelectric ceramics with designed compositions and desired performances [3-5]. For lead-containing ferroelectrics, due to its high volatility, the lead component is very likely lost during the sintering at high temperatures, thus worsening the electrical, optical or other useful characteristics. To reduce the sintering temperature, it is necessary to use powders of ferroelectric compounds with small grain size and narrow size distribution. For this purpose, submicron or even nanosized ferroelectric powders have been synthesized by various wet-chemistry methods in the last decades, including chemical coprecipitation [59, 84, 85, 108], sol-gel process [33, 34, 49, 110], hydrothermal synthesis [50-52, 56-58, 60], microemulsion, combustion [120], thermal pyrolysis spray, molten salt [61, 133], etc.. Although significant progresses have been achieved, there are problems. For example, sol-gel process uses metal alkoxides as the starting materials, which are very expensive and extremely sensitive to the environmental conditions such as moisture, light and heat. Moisture sensitivity makes it necessary to conduct the experiment in dry boxes or clean rooms. Co-precipitation processes involve repeated washing in order to eliminate the anions coming from the precursor salts used, making the process complicated and very time consuming. Furthermore, it is difficult to produce large batches by using most of the chemical solution processing routes. Therefore, exploring alternative methods for the preparation of ferroelectric ceramics is still of technological as well as scientific significances.

1.5. Mechanochemical synthesis of ferroelectric powders and ceramics

Mechanochemical synthesis, which is also known as mechanical alloying, high-energy mechanical milling, high-energy milling, high-energy activation and others (they are not differentiated in the present review unless otherwise stated), was initially invented to prepare oxide-dispersed metallic alloys for structural applications [6-10] and subsequently applied to extensions of metallic solid solubility, synthesis of intermetallics, disordering of intermetallics, solid-state amorphization, nanostructured materials, and mechanochemical synthesis of nanosized oxides or metal powders [11-18]. Recently, this novel technique has been successfully employed to synthesize a wide range of nano-sized ceramic powders, such as ZrO_2 [19, 20], Fe_2O_3 [21, 22], YBCO superconductor [23], ferrite [24-26], as well as various ferroelectrics [47, 62, 64, 94, 126, 137, 140, 155, 180, 188, 194, 196, 201]. The most significant characteristic of this technique is that the formation of the designed compounds is due to the reactions of oxide precursors which are activated by mechanical energy, instead of the heat energy required in the conventional solid-state reaction process. The novel mechanical technique is superior to both the conventional solid-state reaction and the wet-chemistry-based processing routes for several reasons [47, 62, 64]. Firstly, it uses cost-effective and widely available oxides as the starting materials and skips the intermediate temperature calcination step, leading to a simpler process. Secondly, it takes place at room temperature in well sealed containers, thus effectively alleviating the loss of the volatile components, such as lead, bismuth and lithium. This is of particular interest to the synthesis of ferroelectric materials, since most ferroelectric ceramics contain either lead (Pb) [38-42, 62-69, 122-131], bismuth (Bi) [188, 191-202] or lithium (Li) [213] as the major component. Furthermore, due to their nanometer scale size and very high homogeneity, the mechanochemically derived ceramic powders demonstrate much better sinterability than those synthesized by the conventional solid-state reaction and wet-chemical processes. Also, the high-energy milling can greatly improve the reactivity of precursors by reducing the phase formation temperatures of some ferroelectric materials which cannot be directly synthesized, such as $BaTiO_3$ [178-181] and many Arivillius family ferroelectrics [196, 197, 206-210].

Various ferroelectric compounds have been produced via the high-energy mechanical milling processes. Successful examples include: (i) direct synthesis of $PbTiO_3$ (PT) [39-42], $PbZr_{1-x}Ti_xO_3$ (PZT) [62-70], $Pb_{1-y}La_yZr_{1-x}Ti_xO_3$ (PLZT) [94-96, 98], $Pb(Mg_{1/3}Nb_{2/3})O_3$ (PMN) [122-129], $Pb(Zn_{1/3}Nb_{2/3})O_3$ (PZN) [130, 131], $Pb(Fe_{1/2}W_{1/2})O_3$ (PFW) [138-140], and $Bi_3T_4O_{12}$ (BiT) [188, 191]; (ii) improved the reaction of $BaCO_3$ and TiO_2 to form $BaTiO_3$ (BT) [180-182]; and (iii) amorphization of precursors for some Aurivillius family compounds, including BiT, Bi_3TiNbO_9 (BiTN), $SrBi_4Ti_4O_{15}$ (SBiT) and $(SrBi_2Nb_2O_9)_{1-x}(Bi_3TiNbO_9)_x$ [$(SBN)_{1-x}(BTN)_x$] [190, 195-197, 205-212].

1.6. Scope and arrangement of this review

This paper reviews recent progress in the synthesis of various ferroelectric ceramic materials via the high-energy mechanochemical process, arranged in the following orders. A background introduction is followed by a brief description of the experimental procedures. In section 3, synthesis of various ferroelectric materials will be presented. Mechanisms of the direct phase formation and amorphization of the ferroelectrics as a result of high-energy mechanical milling will be discussed in section 4. Finally, the review will be ended with some concluding remarks.

2. Experimental Description

2.1. High-Energy Mechanical Milling

Excellent reviews on the application of high-energy ball milling process to various metallic materials can be found in the open literatures [11-13, 18], where detailed experimental procedures have been discussed. However, to ensure the completeness of the present review, it is still necessary to briefly describe the equipment types, properties and applications of this novel technique. There are various types of high-energy milling machines that have been used and reported in the literature [11, 18]. Different types of mills have different efficiencies and capabilities. The productivity of high-energy mills can be from several grams to as much as thousands of kilograms. High-energy mills that have been widely used for research purpose are vibrational shake mills (SPEX), planetary mills and attitor mills. Other equipments, for example, multi-ring-type mill (Model MICROS: MIC-0, Nara Machinery, Tokyo, Japan), are also used in mechanochemical synthesis of some of the ferroelectric powders [148]. Either stainless steel or tungsten carbide milling media were used in the experiments of high-energy milling.

2.1.1. Vibrational shake mills

SPEX vibrational shake mill is one of the most widely used equipments in the research community of mechanochemical synthesis. The common variety of SPEX shaker mill has one vial, containing the sample and grinding balls, secured by a clamp and swung energetically back and forth several thousand times a minute. The back-and-forth shaking motion is combined with lateral movements at the ends of the vial, so that the vial appears to be following a figure "8" or infinity sign as it moves. With each swing of the vial, the balls impact against the sample and the end of the vial, both milling and mixing the sample. Due to the amplitude (~5 cm) and speed (~1200 rpm) of the clamp motion, the ball velocities are very high (on the order of 5 m/s) and consequently the force caused by the ball's impact is very large, hence, it is a high-energy mill. The only shortcoming of this type of mill is its relatively small throughput, but this problem has been addressed by designing two-vial equipment [11]. Another type of shake mill is Fritsch Pulverizette 0 (provided by Fritsch

GmbH in Germany). Both types of equipments, SPEX 8000 [39, 62, 122-127, 169-171] and Fritsch Pulverizette 0 [195-197, 206-211], have been employed to synthesize ferroelectric nanosized powders.

2.1.2. Planetary ball mills

Planetary ball mills have better capability than the SPEX mill. Vials are arranged on a rotating support disk and a special drive mechanism causes them to rotate around their own axes. The centrifugal force produced by the vials rotating around their own axes and that produced by the rotating support disk both act on the vial contents, which include the materials to grind and the grinding balls. Since the vials and the supporting disk rotate in opposite directions, the centrifugal forces acted alternatively in the same and opposite directions. This causes the grinding balls to run down the inside wall of the vial (the friction effect) followed by the material being ground and grinding balls lifting off and traveling freely through the inner chamber of the vial and colliding against the opposing inside wall (the impact effect). A planetary mill, combined with high-density milling media such as stainless steel and tungsten carbide, also can provide high-energy ball milling. The most popular planetary mills that are reported in the literature are supplied by Fritsch and Retsch in Germany. Various ferroelectric powders have been synthesized using planetary mills [41, 42, 94-96, 149, 155, 195-197, 201-206].

2.1.3. Attritor mills

Although attritor mill has been rarely reported to be used as a tool to synthesize ferroelectric powders, it is of significance to give a brief description. A conventional planetary ball mill consists of a rotating horizontal drum half-filled with small steel balls. As the drum rotates the balls drop on the powders that are being ground; the rate of grinding increases with the speed of rotation. When speeds are too high, however, the centrifugal force acting on the flying balls exceeds the force of gravity, and the balls are pinned to the wall of the drum. As a result, the grinding action stops. An attritor consists of a vertical drum with a series of impellers inside it. Set progressively at right angles to each other, the impellers energize the ball charge, causing powder size reduction because of impact between balls, between balls and container wall, and between balls, agitator shaft, and impellers. Some size reduction appears to take place by interparticle collisions and by ball sliding. A powerful motor rotates the impellers, which in turn agitate the balls in the drum.

One essential advantage of attritor mills is their capable of processing large quantities of powders (from about 0.5 to 40 kg). The operation of an attritor is different from vibration and planetary mills. Powders to be milled are placed in a stationary tank together with the grinding media. During milling process, the mixture is agitated by a shaft with arms, rotating at a speed of about 250 rpm. This causes the media to exert both shearing and impact forces on the material [11].

2.1.4 Process parameters

Mechanical milling process involves a number of variables that can be adjusted to achieve different performances [18]. The important parameters include type of mill, materials used for the milling vial and balls, milling speed, milling time, ball-to-powder weight ratio, milling environment, process control agent (PCA) used, temperature controlling and application of electrical or magnetic field during milling. Typically, for a SPEX shaker mill, 5 g of starting mixture is milled, using a stainless-steel cylindrical vial of 40 mm in diameter and 40 mm in length, with a milling ball of 12.7 mm in diameter. The milling speed is ~900 rpm. Milling time is dependent on the formation abilities of the designed compounds. The planetary mill can mill 20 g of powder at a time. A tungsten carbide vial of 250 ml and tungsten carbide balls with various diameters are used as the milling

media. Typical ball-to-powder weight ratio is 20:1. Milling speed is 200 rpm in most cases. The milling temperature is not controlled intentionally. However, the milling really causes temperature to rise during the milling process. Till now, it remains impossible to monitor the temperature of high-energy milling. However, the raised temperatures should be much lower than the calcination temperatures used in the conventional solid-state reaction process. Unless otherwise specified, milling is generally carried out in air.

2.2. Materials Characterizations

The synthesized materials were characterized by X-ray diffraction (XRD), scanning electron microscopy (SEM), transmission electron microscopy (TEM), differential thermal analysis (DTA), thermal gravity analysis (TGA), thermal expansion/shrinkage, Raman spectrum and Brunauer-Emmett-Teller (BET) specific surface area measurement. Electrical characterizations of ferroelectric ceramics include electrical conductivity, dielectric constant and loss tangent, polarization-electric field hysteresis loop, phase transition characteristics, and so on.

2.2.1. XRD

X-rays are electromagnetic radiation of wavelength about 1 Å (10^{-10} m), which is about the same size as an atom. They are electromagnetic wave in the spectrum between gamma-rays and the ultraviolet. The discovery of X-rays in 1895 enabled scientists to probe crystalline structure at the atomic level. X-ray diffraction (XRD) has been in use in two main areas, for the fingerprint characterization of crystalline materials and the determination of their structure. Each crystalline solid has its unique characteristic X-ray powder diffraction pattern which may be used as a "fingerprint" for its identification. Once the material has been identified, X-ray crystallography may be used to determine its structure, i.e. how the atoms pack together in the crystalline state and what the interatomic distance and angle are. XRD is one of the most important characterization tools used in solid state chemistry and materials science. The information of XRD parameters can also be used to estimate the crystal size of materials with fine crystals. It is based on the Scherrer's formula: $t = \frac{0.98\lambda}{\beta \cos\theta}$ (where t is crystal size, λ the wavelength of X-ray radiation used, β the full width of half maximum (FWHM) peak, θ the diffraction angle). XRD has been extensively employed to characterize the phase composition of ferroelectric powders synthesized.

2.2.2. SEM and TEM

The design principle of TEM is similar to that of a conventional optical microscope. The only difference is that TEM uses a beam of electrons focused by electromagnets, while optical microscopes use a beam of light focused by glass lenses. The wavelike nature of electron is the basis of TEM. The monochromatic wavelength of electron beam is about five orders of magnitude smaller than the wavelength of visible light (400-700 nm) used in optical microscopes. As a result, TEM can resolve much smaller structural details than optical microscopes. The resolution of TEM is about 1 nm or less, as compared to ~0.25 μm, the best resolution achieved by optical microscopes. TEM has been widely used to characterize the morphology, defects, phase structure of various materials, especially for those in nanometer scales.

SEMs usually use an electron beam spot of ~1 μm in diameter, which is scanned repeatedly over the surface of samples. Slight variations in surface topography produce marked variations in the strength of the beam of secondary electrons, which are ejected from the surface of samples by the force of collision with primary electrons from the electron beam. The magnification of SEM is less than that of TEM but much better than that

of an optical microscope. SEM is especially useful for convenient observation of grain and grain boundary structures.

2.2.3. Thermal analysis

The most widely used thermal analysises include differential thermal analysis (DTA), differential scanning calorimetry (DSC), thermogravimetry (TG) and thermomechanical analysis (TMA) or dilatometry (DIL). DTA and DSC monitor the difference in heat flow to or from a sample and to or from a reference as a function of temperature or time, while the sample is subjected to a controlled temperature program. TG is a technique by which the mass of the sample is monitored as a function of temperature or time. TMA is used to measure the dimensional changes of samples as a function of temperature or time. Thermal analysises have been employed to characterize phase formation [68, 70, 123, 125], decomposition, thermal stability [131], and sintering behavior [64, 65, 76, 95] of ferroelectric materials.

2.2.4. Spectra analysis

The most common spectra analysises used to characterize ferroelectric materials are Raman scattering and infrared (IR) reflection/transmission. Raman spectroscopy is a spectroscopic technique used to study vibrational, rotational, and other low-frequency modes in a material system. It relies on inelastic scattering, or Raman scattering of monochromatic light, usually from a laser in the visible, near infrared, or near ultraviolet range. Phonons or other excitations in the material tested are absorbed or emitted by the laser light, resulting in the energy of the laser photons being shifted up or down. The shift in energy gives information about the phonon modes in the system. Infrared spectroscopy yields similar, but complementary information. Raman scattering [40, 64, 169, 235] and infrared (IR) [157, 236] transmission/reflection have been used to phase transition, phase formation and B-site ordering/disordering of normal ferroelectric and relaxors.

2.2.5. Electrical and ferroelectric measurement

Relative dielectric constants of ferroelectric ceramics are usually calculated from the capacitance and dimension of samples. The capacitances are measured using a LCR meter over frequency range of 1 kHz to 1 MHz and temperature range of liquid nitrogen temperature to 500 ℃. Ferroelectric-paraelectric phase transition is characterized by a maximum dielectric constant at a certain temperature. The sharpness or diffuseness of the dielectric constant-temperature curve has been used to distinguish between normal ferroelectric and relaxor [168-171].

Hysteresis loops of ferroelectric materials are recorded while switching with a low-frequency (0.1-60 Hz) sinewave voltage using a Sawyer-Tower circuit or some modified version. The value of polarization measured by this technique usually depends on both the frequency and amplitude of the sine-wave voltage applied. Higher accuracies are obtained at low frequencies (0.1 Hz or less) and high amplitudes (sufficient to produce peak fields at least three times the coercive field), providing the crystal dc resistance at the highest voltage is 10^{12} Ω or higher. The most common equipment for the measurement of P-E curve is supplied by Radiant Technologies [65-67, 94-96, 188].

Piezoelectric coefficients of ferroelectrics can be measured by a so-called resonance method. Resonance method is to measure the resonant and antiresonant frequencies of a poled disc sample. Elastic bodies show numerous resonances. The most pronounced ones are those where the body can just accommodate on half wavelength of a standing elastic wave. Piezoelectric effect is a convenient way to excite such elastic waves to permit observation of the interaction of the mechanical resonance with the electric behavior. In an impedance-

frequency curve, the frequency of minimum impedance is called resonance frequency, while the frequency of maximum impedance is antiresonance frequency. With the resonance and antiresonance frequencies, piezoelectric coefficients can be evaluated. Piezoelectric constant d_{33} can also directly measured using a piezo d_{33}-meter (Channel product, model Berlincourt $_{d33}$-meter).

Pyroelectric property is considered to be generated by the change in the domain polarization in response to a change in temperature. The change in polarization results in a current flow to or from the capacitor as the temperature changes. The traditional method of measuring the pyroelectric response is to monitor the current flow into or out of the capacitor as the temperature is ramped at a constant rate [188]. Radiant Technologies has developed a technique, embodied in the CHAMBER task, whereby the remanent polarization is measured statically over a range of temperatures. The pyroelectric constant can then be calculated from the slope of the remanent polarization versus temperature [Radiant Technologies website].

3. Phase Formation of Ferroelectrics via High-Energy Mechanical Milling

3.1. Normal Ferroelectrics and Antiferroelectrics

3.1.1. Lead titanate and lead lanthanum titanate

Lead titanate ($PbTiO_3$ or PT) ceramics is a typical ferroelectric material, with a phase transition temperature (Curie temperature or T_C) of ~490℃ [27]. The unique properties of PT ceramics, such as high transition temperature, low ratio for the planar-to-thickness coupling factor, low aging rate of the dielectric constant and low dielectric constant, make them useful to a variety of applications. For example, PT ceramics are very good candidates as stable pyroelectric and piezoelectric devices for high temperature or high frequency applications. PT powders have been prepared by various methods. However, it is well known that PT ceramics cannot be prepared via the conventional ceramic process without the addition of other elements. This is due to the anisotropic thermal expansion caused by the phase transition from cubic paraelectric to tetragonal ferroelectric (with a relatively large c/a ratio of ~1.065) during cooling from a high sintering temperature. The phase transition creates large internal stresses, which results in significant fragility and finally destroys the ceramics with numerous microcracks. Modification with other dopants allows for the fabrication of dense PT ceramics using conventional ceramic process [28-32]. However, introduction of other elements into PT ceramics tends to worsen their electrical properties, such as decrease in phase transition temperature and reduction in planar-to-thickness coupling coefficient ratio. Preparation of undoped, dense PT ceramics with good mechanical properties has been attempted by a number of researchers, but very few have succeeded.

Spontaneous cracking in polycrystalline ceramics results from internal stress among the grains, which is caused by incompatible strains from thermal expansion anisotropy during the phase transformation. The area in which microcracking is likely to initiate is defined by a certain grain size limit. The stress per unit grain boundary area is proportional to the grain volume, as shown in Fig. 2 [33]. PT has been reported to crack spontaneously when the average grain size is larger than ~3 μm and to completely disintegrate into powders when the grains are larger than 10 μm. Therefore, it is suggested that crack-free PT ceramics can only be prepared as the grain seizes of the sintered samples are well controlled below 3 μm [33].

Crack-free PT ceramics has been successfully prepared via a sol-gel process [33]. By carefully controlling the calcination temperature of the derived gels and the sintering parameters of the sol-gel derived powders, the grain sizes of the PT powders and thus the sintered PT ceramics could be less than 0.2 and 1.8 μm, respectively. Since the anisotropic stress due to the phase transition was totally buffered by the grain boundaries,

crack-free PT ceramics could be achieved, which are consistent with the above mentioned suggestion. The PT ceramics had a c/a ratio of 1.064 and a density of 96% of the theoretical value, with a Curie temperature T_C of 486 ℃, a dielectric constant of 64, d_{33}=35 *p*C/N and k_p=0.59. Preparation of crack-free PT ceramics has also been realized by other methods, such as seeding-assisted sol-gel process [34] and refined ceramic process [35]. Additionally, dense PT ceramics with submicrometer grains can be obtained by spark plasma sintering (SPS) [36, 37]. The SPS process is able to sinter a compact powder at relatively low temperature in a very short time (a few minutes), which is very effective in suppressing exaggerated PT grain growth. However, it is found that special caution must be given to control the grain size of the PT powders when sol-gel processes are used [33, 34]. The SPS process uses expensive facilities with relatively low productivity. Comparatively, mechanochemical process is able to synthesize nanosized PT powders directly from oxide precursors.

Synthesis of PT powders via mechanochemical milling has been reported by several research groups. Different types of milling equipments were used by different researchers. In 1995, Desu *et al* [38] investigated the effect of mechanical milling on the formation of PT from oxides. They found that the kinetic energy for the formation of PT compound from PbO/TiO_2 mixture was decreased from 152 to 110 kJ/mol, by milling the mixture for only 30 minutes. They also studied the effect of the starting materials on the reaction kinetics under the same milling condition. Wang *et al* [39, 40] used SPEX vibrating mill to synthesize PT powders from oxides (PbO and TiO_2) and amorphous Pb-Ti-O precursor derived from a coprecipitation process. Kong and co-workers [41, 42] used Fritsch Pulverisette 5 planetary high-energy ball mill for the preparation of PT powders from different TiO_2 precursors. There are other examples that can be found in the open literatures [43-45]. It is also reported that a nanostructured PT with photoluminescence (PL) emission in the visible range can be obtained from crystalline PT powders, via a high-energy ball milling [46]. The experimental results suggested that the high-energy milling resulted in the formation of PT amorphous state, creating localized states in the interfacial region between the crystalline PT and the amorphous PT. The localized states are responsible for the PL phenomenon, which can be readily controlled by adjusting the milling time. This achievement demonstrates an additional function of the high-energy mechanical milling process in creating advanced materials with promising characteristics.

The evolution of PT phase formation from oxide precursor caused by the high-energy ball milling is time dependent. Fig. 3 shows the XRD patterns of the mixture of PbO and TiO_2 powders milled for different durations, using a SPEX shaker-mill [39]. The particle size of the PbO and TiO_2 powders is 3 to 5 μm. To ensure the homogeneity of the oxide mixture, the oxides were thoroughly mixed using a standard laboratory ball mill prior to the high-energy mechanical activation. The unmilled mixture was characterized by sharp diffraction peaks due to the starting PbO and TiO_2, because of their good crystallinity and large particle size. After milling for 5 h, the diffraction peaks of the precursor oxides were greatly broadened and reduced, indicating great refinement in particle/grain size. At the same time, the PT phase appears with relatively weak diffraction intensities. With further milling, the signals from PT perovskite structure increase gradually. After milling for 20 h, single phase PT with a well developed XRD pattern is obtained. TEM image of the 20-h-milled sample shows that the PT powders have a particle size of 20 to 30 nm, as shown in Fig. 4 [39]. Similar result was observed in the samples derived from a coprecipitated amorphous precursor, where 20-h-milling resulted in nanosized PT powders, confirmed by TEM observation and Raman spectroscopy [40]. Short-time milling can promote the crystallization of PT from the precursors during the post-thermal annealing [40].

Kong *et al* [41] compared the PT phase formation behavior with two types of starting TiO_2 powders, namely anatase and rutile, using a Fritsch Pulverisette 5 type planetary high-energy ball mill. XRD patterns of the mixtures of PbO, anatase and rutile milled for different durations are shown in Fig. 5 [41]. The 2-h-milling does not result in the formation of $PbTiO_3$ perovskite phase. However, no TiO_2 peaks are detected in the XRD patterns, due to the weak intensity of TiO_2 as compared to that of PbO. The difference is revealed in their patterns after milling for 20 h. Single phase PT is formed in the PbO-anatase mixture, while a trace of PbO is still observable in the PbO-rutile group. No significant difference is found between the two systems after milling for prolonged durations. This means that the effect of precursors on the formation of PT phase occurs only at the initial stage of the milling process, which can be readily attributed to the different reactivities of anatase and rutile used in the experiments. As shown in Fig. 6 (a) and (b) [41], the average grain sizes of anatase and rutile powders are 0.15 and 2 μm, respectively. The morphologies of the mixture of PbO-anatase milled for 2, 20 and 80 h are shown in Fig. 6 (c) to (e) [41]. For the sample milled for 2 h, there are some large grains with apparent milling scratches on the surface, with many small particles stuck to the surface of the large grains. By increasing the milling durations, the amount of large grains is greatly decreased, due to disintegration into small particles. The grain size estimated from the TEM images varies from 10 to 50 nm, which is similar to that observed by Wang *et al* (Fig. 4) [39]. Prolonged milling does not change the grain morphology and size of the samples significantly. The PT powders derived from the PbO-rutile showed similar characteristics to that of the PbO-anatase mixture.

The effect of PbO/TiO_2 ratio on the phase formation of PT via the high-energy mechanical milling was also investigated [47]. Fig. 7 shows the XRD patterns of the mixtures with PbO/TiO_2 (anatase) ratios from 1.4 to 0.75. It is found that single phase PT can be formed from the mixtures with different PbO/TiO_2 ratios. However, the tetragonality (c/a ratio) of the PT phases obviously decreases from ~1.03 for PbO/TiO_2=1.4 to ~1.01 for PbO/TiO_2=1.00. The samples from the mixtures with PbO/TiO_2 ratio less than 1 are of cubic structure. It is important to note that the PT powders have almost the same grain size, although they have different tetragonalities. It means that high-energy ball milling technique is able to synthesize PT compound with compositions far away from the 1:1 stoichiometric state. Such a wide range of nonstoichiometry has not been reported for PT powders prepared by the conventional solid-state reaction method and wet-chemistry processing routes. This result should also be applicable to other lead containing ferroelectric compounds.

Tetragonality is a measure to specially characterize the lattice structure of materials with a tetragonal structure. Tetragonality is defined as the ratio of c-axial to a-axis (c/a). Depending on the lattice structure, c/a can be either smaller or larger than 1. For most ABO_3 type ferroelectric materials, the tetragonality is usually lager than 1, i. e. c>a. PT has the largest tetragonality (c/a~1.065) among tetragonal ferroelectric materials. The tetragonality is dependent directly on grain size and indirectly on material processing [54, 254-259]. Generally, tetragonality decreases with decreasing grain size. As the grain size reaches a critical value, tetragonality becomes 1, i. e. the material is cubic structure. Other factors, such as composition (ration A:B) and the presence of foreign ions, are also critical in determining the tetragonality of ferroelectrics [257, 259]. For example, Sun *et el* [257] found that excess barium cations in hydrothermal reaction solution was favorable to increase the tetragonalility of barium titanate powders, although a clear understanding of this phenomenon is still unavailable. This observation is similar to the variation with composition in tetragonality of the PT powders synthesized via high-energy ball milling, as discussed above.

It is worth mentioning that crack-free PT ceramics can be obtained from the synthesized PT powders [42]. Fig. 8 shows the SEM images of the PT ceramics derived from the PbO-anatase system sintered at 1100 ℃ for 1 h [42]. The average grain size of the PT ceramics is about 1 μm and decreases gradually with increasing milling time. The grain sizes are less than the critical size of 3 μm, below which crack-free PT ceramics will be produced. The slight decrease in the grain size of PT ceramics with milling time can be understood from the characteristics of the synthesized powders milled for different durations. The formation of crack-free PT ceramics can be attributed to the fact that PT powders synthesized via the high-energy mechanical milling process are of nanometer scale grains. Such powders possess very high sinterability, and hence, can be sintered at relatively low temperature. The low sintering temperature effectively suppressed the grain growth of the PT ceramics. Prolonged milling introduced more defects such as lattice dislocations, stresses, vacancies, etc.. Elimination of these defects might be at the expense of grain growth. Therefore, the grain size of the PT ceramics decreases slightly with increasing milling time on the PT powders. In other words, one can control the final grain size of the PT ceramics by simply adjusting the milling time during the synthesis of the PT powders.

To determine if the formation of the crack-free PT ceramics is due to the contamination of tungsten carbide that comes from the vials and balls during the high-energy milling process, TEM element analysis has been applied to the content of any impurities in the as milled powders. It is found that tungsten content in the sample milled for 80 h was less than 1 at% [47]. Similar observation has been reported by Jiang *et al* [19], who examined the tungsten contamination in ZrO_2 powder milled for as long as 120 h with a tungsten carbide milling media and found that the tungsten content is less than 1 at%. Therefore, it is reasonable to exclude the contribution of contamination to the formation of crack-free PT ceramics using the mechanochemically synthesized PT powders. Additionally, no second phases could be detected by the XRD measurement of the PT ceramics [42]. This has also been supported by the differential thermal analysis (DTA) results of the PT ceramic pieces. As shown in Fig. 9, the DTA curve of the PT ceramics produced from the 20-h-milled powder clearly shows an endothermic peak at 491 ℃ during heating up and an exothermic peak at 471 ℃ during cooling down, respectively. The endothermic peak at 491 ℃ is the Curie temperature T_C of PT, corresponding to the phase transformation from tetragonal ferroelectric state to cubic pyroelectric state. The exothermic peak at 471 ℃ is 20 ℃ below the endothermic peak, due to the hysteresis of the phase transition of PT. Almost similar DTA curves were observed for the samples made from powders milled for longer durations. If there were impurities that have been incorporated into the PT ceramics, their Curie temperatures would have been changed.

Milling enhanced phase formation of PT nanopowders was reported by Wongmaneerung *et al* [237], where the milling was conducted using a vibro-mill, with polypropylene jar and polycrystalline Al_2O_3 ceramic bars as milling media. Due to the fact that it was not really a high-energy milling, the milled powders had to be thermally treated at 600 ℃ for 1 h, in order to form PT phase. However, the milling time duration had a significant effect on the phase formation and particle size of the PT powders. It was found single phase PT powder with uniform particle distribution could be obtained after milling for 25 h.

In summary, high-energy mechanical milling has been shown to be a unique method in the preparation of PT powders and crack-free PT ceramics. As compared to most chemical processing routes such as sol-gel [48, 49] and hydrothermal method [50-52], high-energy mechanical milling technique is much simpler and more cost-effective.

As discussed above, dense PT ceramics can be prepared by addition of other elements, among which lanthanum is widely used. Lanthanum ion (La^{3+}) has a radium of 1.032 Å and substitutes for Pb^{2+} (r=1.19 Å) at A-site, instead of B-site Ti^{4+} ion due to the large difference between La^{3+} and Ti^{4+} (r=0.605 Å). To maintain electrical neutrality, La-doped PT (PLT) is compensated by forming A-site or B-site vacancies. Two formula, $Pb_{1-3x/2}La_xTiO_3$ (PLT-A) and $Pb_{1-x}La_xTi_{1-x/4}O_3$ (PLT-B), are derived for A-site and B-site, respectively. PLT-A had giant relative dielectric constant, while PLT-B demonstrated relaxor ferroelectric characteristics. Due to the volatility of PbO at high temperatures, it is difficult to control over the exact stoichiometry of PLT when using the conventional solid-state reaction process. This problem can be readily addressed by suing high-energy mechanochemical milling to synthesize the compounds, as reported by Wang *et al* in a recent article [238].

3.1.2. Lead zirconate titanate

Lead zirconate titanate ($Pb(Zr_xTi_{1-x})O_3$ or PZT) ceramics, solid solutions of PT and PZ, are important to a variety of applications such as transducers, sonars, micropositioners, rotary actuators and pyroelectric sensors, etc, due to its outstanding ferroelectric, piezoelectric, pyroelectric, and opto-electronic properties, and have been extensively and intensively studied for several decades [1-3]. Although PZT ceramics of different compositions have various functions, one of the salient features of the phase diagram for this solid solution system is the existence of the almost temperature-independent phase boundary around x=0.52-0.53, which separates a rhombohedral Zr-rich phase from a tetragonal Ti-rich phase. Fig. 10 shows a phase diagram of PZT, which is the most classical PZT phase diagram widely cited in the literature [99]. The dielectric constant, piezoelectric constant and electromechanical coupling coefficient all exhibit a pronounced maximum value for the composition corresponding to this phase boundary, which is generally referred to as the morphotropic phase boundary (MPB) in the literature [1, 2, 54]. This is mainly attributed to the existence of a mixture of phases at the boundary and the presence of a larger number of reorientable polarization directions existing in the MPB mixed-phase region [1, 99].

PZT ceramics with the composition of MBP can be used as actuators and transducers with excellent performances. Similar to its end components PT and PZ, PZT has also been prepared by conventional solid state reaction process and various chemical and physical processing routes [53-61]. However, the available results have demonstrated that high-energy milling is a versatile technique to produce PZT powders and ceramics. Synthesis of nano-sized PZT powders and fabrication of PZT ceramics from the synthesized powders have been reported by several groups, using different milling equipments [62-70].

Nano-sized PZT powders have been synthesized from constituent oxides and coprecipitated precursor via high-energy mechanical milling, using either SPEX shaker mill [62, 63, 70, 127] or planetary ball mill [64-67, 241]. The effects of milling and milling duration on the microstrcutural and electrical properties of the PZT ceramics derived from the milled powders have also been studied.

Phase evolution of PZT perovskite in either oxide mixtures or coprecipitated amorphous precursors as a result of high-energy mechanical milling, as shown in Fig. 11 [63] and Fig. 15 [65], which is similar to that of PT, as described above [39], will not be discussed in this section. Instead, some interesting aspects regarding the microstructural and electrical properties of PZT ceramics derived from milled mixtures will be highlighted.

Wang *et al* [63] compared the microstructural and electrical characteristics of PZT ceramics made from the powders milled for different durations. XRD patterns of the mixtures (PbO, ZrO_2 and TiO_2) milled for various durations, using a SPEX shaker mill, with stainless still milling media, are shown in Fig. 11 [63]. The

unmilled sample is a mixture of the precursors, while the 10-h-milled sample consists of perovskite PZT and small amount of the unreacted oxides. Single phase PZT is obtained after milling for 25 h. The XRD patterns of the unmilled and the 10-h milled mixtures calcined at different temperatures are shown in Fig. 12 and Fig. 13, respectively [63]. For the unmilled mixture, PT was formed at 600 ℃-700 ℃ as an intermediate phase before the formation of single phase PZT at 800 ℃. In contrast, direct formation of PZT phase is observed in the mixture milled for 10 h. PZT starts to appear at 500 ℃, while single phase PZT is obtained at 700 ℃, which is 100 ℃ lower than that required by the unmilled sample. These observations indicate that PZT phase formation was greatly enhanced as a result of the high-energy mechanical activation. The enhanced PZT phase formation can be readily attributed to the refinement of the oxide precursors as a result of the high-energy milling.

Besides the enhancement in phase formation, the microstructural and electrical properties of the PZT ceramics are also closely related to milling conditions. Fig. 14 shows the relative density of the PZT ceramics, made from the mixtures milled for different durations, as a function of sintering temperature [63]. Dielectric constant and loss tangent of the PZT ceramics are listed in Table 1 [63]. The milled powders can be sintered to 95% relative density, while the maximum relative density of the samples derived from the unmilled powders is only 76%. The poor densification behavior of the unmilled mixture was attributed to the involvement of intermediate phases (PT or PZ) during calcination. The volume expansion associated with the formation of PT due to the preferential diffusion of PbO was thought to lead to the low sintered density of the samples derived from the unmilled mixture. However, this explanation seems incorrect. In fact, volume expansion is often observed in the formation of many lead-containing and bismuth-containing ferroelectric materials. Some of them do not involve the formation of intermediate phases (PT or PZ), such as PMN (lead magnesium niobate, $PbMg_{1/3}Nb_{2/3}O_3$) [53] and $Bi_4Ti_3O_{12}$. This expansion also takes place in unreacted and partially reacted mixtures as reported in Refs 65 and 67. Dense PZT ceramics can be obtained from the 4-h milled unreacted mixture with a distinct volumetric expansion [65]. The failure in observing a volume expansion in the 10-h-milled mixture reported in Ref [63] may be due to the fact that the method (mass/volume and the Archimedes) is not sensitive enough to detect the small degree of the expansion. Nevertheless, the poor densification behavior of the unmilled system cannot be solely attributed to the volume expansion due to the presence of intermediate phases. Actually, before the final densification of lead containing ferroelectric ceramics due to the sintering at a higher temperature, samples would experience a volume expansion due to the reaction at an intermediated temperature. The poor densification characteristic of the unmilled mixture as compared to its milled counterpart observed in Ref [63] is actually related to the poor densification of the sample during the sintering process at high temperatures. The difference in electrical properties between the samples made from the unmilled and milled powders can be easily attributed to their microstructural difference. For example, the high dielectric loss tangent of the PZT ceramics derived from the unmilled mixture is due to their high porosity.

XRD patterns of the mixtures (PbO, ZrO_2 and TiO_2), milled for different durations, using a Fritsch Pulverisette 5 planetary high-energy ball milling system, with tungsten carbide vials and balls, are shown Fig. 15 [65]. After milling for 4 hours, no PZT is formed, but the diffraction peaks PbO are greatly broadened and weakened, indicating that the starting oxides have been significantly refined as a result of the high-energy ball milling. The diffraction peaks of PbO are further widened and reduced in the 8-h milled sample. At the same time, a trace of PZT can be observed. PZT becomes predominant phase in the samples milled for 15 and 24 h.

The densification behaviors of the mixtures milled for various durations are shown in Fig. 16 [65]. A distinct volumetric expansion is observed in the densification rate curves. The temperature characteristics related to the densification behaviors of the milled mixtures are summarized in Table 2 [65]. This volumetric expansion is undoubtedly attributed to the formation of PZT from the constituent oxides. The volumetric expansion temperatures are 771°C, 763°C and 752°C for the powders milled for 4, 8 and 15 h, respectively. The slight decrease in peak temperature is due to the reduction in particle size of the powders as a result of milling. The degree of the volume expansion decreases with increasing milling duration, implying a decrease in the amount of the unreacted oxides. Almost no volume expansion is detected in the 24-h milled mixture due to the completed reaction induced by the high-energy mill. These observations are in agreement with the XRD results as shown in Fig. 15. The volume expansion is followed by a subsequent densification, which is known as reactive sintering. The degree of reaction of the 8 and 15-h-milled samples is comparable with that of the 10-h-milled mixture reported in Ref [63].

It is demonstrated in Fig. 14 that the volumetric expansion is accompanied by two densification peaks. The first densification maximizes at about 800°C for all four samples, which is attributed to the formation of a PbO-rich liquid phase because of the low melting point of PbO. The main densification mechanism for this sintering stage is related to particle rearrangements with the presence of the PbO-rich liquid phase [82]. The second peak, on the other hand, is related to the intermediate and final stages of sintering under the densification mechanism of volume diffusion [82]. As shown in Table 2, the second shrinkage peak gradually decreases from about 860°C for the 4-hour milled powder to about 800°C for the 24-hour milled sample, which is mainly related to their different degrees of refinement and homogeneity due to the different milling durations. It is necessary mentioning that the temperatures (Table 2) of the second maximum for the ball milled mixtures are much lower than that observed for conventionally derived PZT powders, where the final densification maximum usually occurred at ~1100°C [82]. This observation means that PZT ceramics can be obtained at low temperatures from the high-energy ball milled powders.

It is noted from Fig. 16 that the densification already finished after 900°C, showing the high sinterability of the milled powders. The final linear shrinkages of the four mixtures are very close to one another, which means that they can be sintered to ceramics with almost the same density. This has been confirmed by experiments. Fully dense and phase pure PZT ceramics can be obtained not only from the synthesized nano-sized PZT powder (24 h milled) but also from the partially reacted mixtures (8 h and 15 h milled) and even unreacted precursor (4 h milled). Furthermore, the sintering temperature required is not higher than 1000°C.

Fig. 17 shows the cross-sectional SEM image of the 900°C-sintered PZT ceramics derived from the 4 h milled mixture of Fig. 15. Well developed grains with an average grain size of ~1 μm have been formed at such a low sintering temperature. XRD results showed that the 900°C-sintered is a pure perovskite phase, indicating the completion of PZT phase formation in the unreacted mixture, which is consistent with the dilatometer analysis (Fig. 16). Polarization-electric field (P-E) curves of the PZT ceramics, derived the 4-h milled mixture and sintered at 900-1000°C for 4 h, are shown in Fig. 18 [66]. Saturated P-E curve is already developed in the sample sintered at 950°C, although the polarization is smaller than that of the sample sintered at higher temperatures.

The PZT ceramics prepared from the 4-h-milled oxide mixture sintered at 1000 °C for 4 h have a dielectric constant of 1156, a dielectric loss tangent of 0.03, a remanent polarization of 29 $\mu C/cm^2$ and a coercive field of 18.4 kV/cm. Piezoelectric parameters of the 1000°C-sintered PZT ceramics are considerably promising, with k_{33} of 40.4%, k_{31} of 40.9%, d_{33} of 175 *p*C/N and d_{31} of -148 *p*C/N, respectively [66]. PZT ceramics with similar electrical properties have also been obtained from the mixtures milled for 8 h and 15 h. These properties of the PZT ceramics derived from the mechanically treated oxide mixtures at low sintering temperature are essentially comparable to those reported in the literature, where various additives with low melting points were used to reduce the sintering temperatures of PZT ceramics [71-76].

Rear earth element-doped PZT ($Pb_{0.92}Gd_{0.08}(Zr_{0.53}Ti_{0.47})_{0.98}O_3$, PGZT and $Pb_{0.92}Nd_{0.08}(Zr_{0.53}Ti_{0.47})_{0.98}O_3$, PNZT) [69, 240] nanoceramics derived from mechanically activated precursors were found to possess special dielectric and ferroelectric properties, as compared to those produced via a the conventional ceramic process. It was found that the PGZT ceramics had higher dielectric constant than their counterparts from the un-treated powders [69]. For example, the dielectric constants of the PGZT ceramics derived from the powders, milled for 25, 30 and 35 h, are 9238, 10826 and 10801 (at T_C), respectively, while the value fo the sample prepared by solid-state reaction is only 7296. The authors attributed the high dielectric constants of the MA samples to their nanocrystalline nature and they concluded that MA technique is a promising way to fabricate ferroelectric materials with high dielectric constant [69]. Although the PNZT ceramics showed a nonrelaxor ferroelectric behavior, they had a diffused ferroelectric-paraelectric phase transition. The nanosized PNZT ceramics had very high resistivities, which could be an additional advantage for practical applications [238].

Nanosized phase-pure $Pb(Zr_{0.7}Ti_{0.3})O_3$ (PZT) powders were mechanically synthesized from lead-zirconium-titanium (Pb-Zr-Ti) hydrous oxide precursor in NaCl matrix [241]. Because NaCl is soluble in water, it can be easily removed by repeated washing with deionized water. The authors studied the effect of weight ratio of NaCl and the hydrous oxide precursor and found that the most appropriate ratio is 4:1. The resultant PZT powders had an average grain size of ~110 nm. Fully sintered PZT ceramics could be obtained at 1150 ℃ for 2 h. This temperature is 50 ℃-150 ℃ lower than those widely used in the conventional ceramic process. The electrical properties, such as planar electromechanical coupling coefficient, longitudinal piezoelectric coefficient, relative dielectric constant and dielectric loss tangent, are in a good agreement with the reported data in the literature.

Besides, Branković *et al* [68] found that PZT phase can be obtained after milling for only 1 h by using an intensive milling (i. e. high milling speed and large ball-to-powder weight ratio). The significance of this achievement is that the time consumption can be reduced and the productivity of fabrication will be increased.

3.1.3. Lead lanthanum zirconate titanate

Lead lanthanum zirconate titanate (PLZT) ceramics, with variable dopant concentrations of lanthanum and different Zr/Ti ratios, exhibit a variety of ferroic phases such as ferroelectric (FE), antiferroelectric (AFE) and paraelectric (PE) phases. As a result, PLZT ceramics are widely investigated during the last decades [77-83]. The general formula of PLZT is $(Pb_{1-y}La_y)(Zr_{1-x}Ti_x)_{1-y/4}O_3$, usually being shorted as PLZT100y/1-x/x. Fig. 19 shows a typical room-temperature phase diagram of PLZT solid solution, where various phases exist with different compositions [81]. The phases of great importance include antiferroelectric orthorhombic (AFE_O), ferroelectric rhombohedral (FE_{Rh}), ferroelectric tetragonal (FE_{Tet}), relaxor ferroelectric (RFE) and paraelectric cubic (PE_{Cubic}). Several PLZT ceramics have been studied to show the feasibility of the high-energy milling

technique in synthesizing multicomponent materials. PLZT8/65/36 is a typical relaxor ferroelectric material having high dielectric constant and low coercive field. It can be sintered to transparent ceramics that is a novel electro-optic material and can be used for a variety of applications such electro-optic switches [84-93]. PLZT7/60/40 possesses the highest values of piezoelectric longitudinal coefficient (d_{33}=710 pC/N) and electromechanical planar coupling (k_p=0.72) among the available PLZT ceramics ever reported in the literature [93]. PLZT2/95/5, an antiferroelectric ceramic material [81], is also included in this section to make a comparison with other PLZT materials. PLZT15/65/35 is a paraelectric compound at room temperature [81], which is selected in order to comparatively study the effect of lanthanum content on the phase formation and microstructure development of PLZT ceramics derived from the powders synthesized by mechanochemical reaction. The experiment was conducted using a planetary high-energy ball mill with tungsten carbide milling media, as described in section 3.1.1 and 3.12.

Fig. 20 shows the XRD patterns of the 36-h-milled mixtures for PLZT8/65/35, PLZT15/65/35 and PLZT2/95/5 [94]. PLZT perovskite phases are predominant for all three mixtures after milling for 36 h. The milled samples were examined by SEM and BET to be of an average particle size less than 50 nm. For Mixture for PLZT8/65/35 was also milled for 4 h and 15 h to obtain unreacted and partially reacted samples. PLZT ceramics can also be derived from the partially reacted or unreacted systems via reactive sintering. The reactive sintering characteristics of the mixtures milled for short times (4 h and 15 h) are obviously evidenced by their densification behaviors, as shown in Fig. 21 [95]. A volumetric expansion can be observed in the shrinkage curves of the 4-h and 15-h-milled samples. This observation is similar to that of PZT as described in the previous section. The electrical properties of the PLZT8/65/35 and PLZT2/95/5 ceramics are listed in Table 3 and Table 4, respectively [95]. These results are comparable to the reported values in the literature [78, 81, 84].

Additionally, transparent PLZT8/65/35 ceramics can be obtained from the mixtures milled for 4, 15 and 36 h. Transparent PLZT8/65/35 ceramics are important electro-optic materials. They were conventionally fabricated by either hot-pressing [1, 85] or oxygen atmosphere sintering via two-step or multiple-step processing [84, 86-90]. Hot-pressing is very time consuming, producing only a few pieces of product per week. Therefore, transparent PLZT ceramics obtained in this way are very expensive. Furthermore, hot-pressing derived transparent PLZT ceramics have other unwanted properties, such as optical anisotropy caused by the residual strain and contamination coming from the hot-pressing die materials [1]. Alternatively, oxygen-atmosphere sintering is then widely used. Transparent PLZT ceramics derived from the solid-state reacted powders typically need a sintering temperature of 1250°C and time duration of 60 h in flowing oxygen [87]. The high sintering temperature required by the solid-state reaction powders is due to the coarse PLZT powders. To reduce the sintering temperature, fine PLZT powders must be used [84]. Fine PLZT powders were usually synthesized via chemical methods. Preparation of four-component PLZT via chemical process is still a challenging.

To prepare transparent PLZT8/65/35 ceramics, the milled mixtures were firstly sintered at 900-1000°C for 4 h. The sintered samples were then annealed at 1125°C for 6 h. This annealing was repeated for 4 times [96]. Fig. 22 shows the surface SEM images of the transparent PLZT ceramics. It is interesting to note that the grain size of the annealed samples decreases gradually as the sintering temperature used to pre-sinter the samples increases. In other word, the larger the grain size of the presintered ceramics, the smaller the grain size of the annealed samples. The average grain size of the presintered and annealed PLZT ceramics as a function of

sintering temperature is shown in Fig. 23 [96]. This observation can be explained as following. The grain growth of the sintered PLZT ceramics is very similar to that in a two-step sintering process for Y_2O_3, $BaTiO_3$ and Ni-Cu-Zn ceramics reported by Chen *et al* [97, 226, 227], where samples were initially heated to a certain high temperature for a short time duration and cooled to a relatively lower temperature (both temperatures are selected depending on materials studied) and kept for a longer time duration. Fully sintered Y_2O_3, $BaTiO_3$ and Ni-Cu-Zn ceramics without final-stage grain growth could be achieved [97, 226, 227]. The suppression of the final-stage grain growth has been attributed to the fact that the second-step sintering proceeded in a 'frozen' microstructure with slower kinetics. In other words, the driving force for grain growth decreases with increasing grain size. The higher the sintering temperature at which the ceramics were sintered (first sintering), the larger the grain size is. As a result, the PLZT ceramics sintered at low temperature with smaller grain size will have larger grain size when annealed (second sintering) at the same annealing conditions.

The transparent PLZT8/65/35 ceramics obtained by annealing the low-temperature-sintered samples all showed good transmission properties, as shown representatively in Fig. 24 [96]. A transmittance of about 40% at a wavelength of 550 nm is achieved, which is compatible to the results for the PLZT8/65/35 ceramics prepared by other methods [87-89, 92]. The result further confirms that the milled powders via high-energy milling are not contaminated by the milling media, since optical property is more sensitive to contaminations than electrical properties.

In summary, nano-sized PLZT powders with various compositions can be synthesized from oxide mixtures via a high-energy ball milling process. PLZT8/65/35 ceramics were obtained using the produced powders by sintering at temperatures ranging from 900°C to 1000°C. Transparent PLZT8/65/35 ceramics have been obtained by annealing the sintered PLZT samples via a repeated thermal annealing technique.

Another interesting aspect is the effect of excessive PbO on the microstructural development and electrical properties of PLZT7/60/40 ceramics derived from high-energy ball milled oxide mixtures [98]. It has been found that excessive PbO showed a positive effect on the densification behavior of PLZT ceramics at low temperature (below 1050°C). However, dense samples can be obtained at temperatures above 1050°C without excessive PbO [98]. The PLZT ceramics derived from the precursor without excessive PbO possessed better dielectric and ferroelectric properties than those from the mixture with 20% excessive PbO.

XRD patterns of the high-energy mechanically milled oxide mixtures for PLZT7/60/40 with and without 20% PbO are shown in Fig. 25. About 90% perovskite phases are formed in the two milled powders. To obtain PLZT ceramics, the milled powders were compacted and sintered at 900 to 1150 ℃ for 1 h. Fig. 26 illustrates the cross-sectional surface SEM images of the PLZT ceramics with and without excess PbO sintered at 1100 ℃. The grain size of the sintered ceramics as a function of sintering temperature is plotted in Fig. 27. It shows an almost linear increase with increasing sintering temperature. The grain size of the samples with excessive PbO is slightly smaller than that of those without excessive PbO. Fig. 28 shows the density of the PLZT ceramics as a function of sintering temperature. The mixture with excess PbO exhibits a good densification behavior. The relative density of the sample sintered at 900°C is already ~97%. In contrast, the densification of the sample without excessive PbO is very slow at low temperatures (<1050°C). The relative density of the 900°C-sintered samples is only 83%. SEM images of the 950°C-sintered samples are shown in

Fig. 29 [98]. It is obviously demonstrated that the sample without excessive PbO is very porous while that with 20 mol% excessive PbO is almost pore-free.

This difference in grain size and microstructure can be attributed to the difference in sintering mechanism governing the grain growth in the two groups. A liquid phase is formed at low temperatures when PbO is excessive due its low melting point (850°C). Therefore, the sample with excessive PbO densified via the rapid rearrangement of the particles surrounded by the liquid phase at low temperature. Since the liquid phase wets the grain boundaries, grain growth slows down because the driving force is reduced and the mass transportation only takes place by penetrating the liquid layer, i. e. diffusion path is increased [82]. As a result, samples with excessive PbO densify at low temperature with low grain growth. In contrast, the densification of the sample without excessive PbO is advanced by solid-state sintering process, where contact points are formed between particles. Grain growth is favored because of the contact of particles. However, a rigid skeleton is likely to form due to the formation of the point contacts between particles. This rigid skeleton prevents the sample from further densification. Consequently, samples without excessive PbO have larger grain size and lower density. At higher temperature, the two systems possess similar densification mechanism [82]. This observation can be understood by referring to the schematic diagram of sintering mechanisms as illustrated in Fig. 30.

There is no significant difference observed in dielectric and ferroelectric properties of the PLZT7/60/40 ceramics with and without the 20% excessive PbO, as the sintering temperature is above 1050°C. Additionally, piezoelectric coefficients (d_{33}) of the 1150°C-sintered PLZT ceramics are 702 and 689 *p*C/N for samples without and with excessive PbO respectively, which are comparable with the reported values in the literature for those prepared by the conventional ceramic process [93]. This result therefore indicates that excessive PbO that is necessarily used in conventional solid-state reaction process is not a crucial requirement when PLZT ceramics are prepared from mixtures treated by a high-energy ball milling process. This conclusion should also be applicable to other PbO-containing materials.

3.1.4. Antiferroelectrics

Antiferroelectrics are materials with neighbour spontaneous polarization dipoles anti-parallel to each other. The phase transformation of antiferroelectric ceramic from antiferroelectric (AFE) to ferroelectric (FE) phase can be induced by a sufficiently high electric field [99-102]. This phase transformation is accompanied by a large volumetric change since the unit cell of FE phase is larger than that of AFE phase. As a result, a very large longitudinal strain is associated with the AFE to FE phase transformation, as compared with the strains achieved by ferroelectric materials. This characteristic of antiferroelectric ceramics makes them good candidates for high displacement electromehanical actuator applications [99-103]. In addition, the transformation of antiferroelectrics from AFE to FE phase leads to a significant energy storage, which can be used in energy storage applications [104, 105]. Antiferroelectric ceramics are also studied because of their unique pyroelectric, electrooptical and many other useful properties [99]. It is difficult to synthesize antiferroelectrics, especially for those with multicomponent compositions, using chemical processing methods, such as coprecipitation and sol-gel process. Antiferroelectric materials synthesized via high-energy mechanical milling process include lead zirconate ($PbZrO_3$ or PZ) [99, 100], lead lanthanum zirconate titanate (PLZT2/95/5) [81], and La-/Nb-doped lead zirconate titanate stannate [$Pb(Zr,Ti,Sn)O_3$ or PSZT] [105-107].

PZ is an antiferroelectric material with a Curie temperature of 230°C [99]. The formation of PZ from the mixture of PbO and ZrO_2 activated by the high-energy milling is more difficult than that of PT. Fig. 31 shows the XRD patterns of the mixture of PbO and ZrO_2 milled for 24 hours [113]. The formation of PZ is difficult than that of PT or PZT, which is probably because ZrO_2 is less reactive than TiO_2. However, single phase PZ can be obtained after sintering at 900°C. This temperature is very close to that achieved by most chemical processing routes [108-110]. The particle size of the milled powder is about tens of nanometers, which is similar to those observed in other materials. The microstructure, lattice parameters and dielectric properties of the PZ ceramics derived from the milled PbO and ZrO_2 mixture are well comparable to those reported in the literature [99].

PZST family is another group of antiferroelectric materials, which has drawn much attention due to their good electrical properties [99, 106, 107, 110]. PZST ceramics, with typical compositions of $Pb_{0.99}Nb_{0.02}(Zr_{0.85}Sn_{0.13}Ti_{0.02})_{0.98}O_3$ (PNZST) and $Pb_{0.97}La_{0.02}(Zr_{0.65}Sn_{0.31}Ti_{0.04})O_3$ (PLZST), have been derived from oxide precursors via a high-energy ball milling. Fully dense PNZST and PLZST ceramics were obtained by sintering the milled precursors at 1200 ℃ for 1 h [111]. The two samples demonstrated an maximum polarization of 29 and 53 $\mu C/cm^2$, forward switching field (antiferroelectric to ferroelectric, or E_{AFE-FE}) of 76 and 75 kV/cm, and backward switching field (E_{FE-AFE}) of 33 and 24 kV/cm, respectively, which are comparable to those reported in the literature for the same PZST ceramics [99, 106, 107]. As mentioned above, it is difficult to synthesize multicomponent ceramic powders via wet chemistry routes, such as chemical coprecipitation and sol-gel. Therefore, the successful synthesis of nanosized PNZST and PLZST powders via the high-energy milling process is of great significance. This achievement is especially useful when more components are needed to modify the properties of these materials.

3.2. B-site Perovskite Relaxor Ferroelectrics and Their Derivatives

Relaxor ferroelectrics are complex lead-containing materials with the perovskite structure [114, 115]. Generally, they have a formula of $Pb(B'B'')O_3$, where B' is a low-valence cation, such as Mg^{2+}, Zn^{2+}, Fe^{3+} or Sc^{3+}, and B" is a high-valence cation, such as Nb^{5+}, Ta^{5+} or W^{6+} [116, 119, 130, 132, 134, 141, 142]. Relaxors are characterized by their high dielectric constant, broad and frequency-dispersive temperature dependence of dielectric constant. These properties can be ascribed to the so-called local compositional heterogeneity caused by the lack of ordering among the cations within the B-site sublattice. Their high dielectric constant, together with excellent electrostrictive response, makes relaxor ferroelectrics very useful for a wide range of applications, such as high dielectric constant capacitors, various sensors, transducers and actuators. The main problem for the synthesis of relaxors is the presence of pyrochlore, which seriously degrades the performance of relaxor ferroelectrics. To address this problem, two-step processing routes (e. g. columbite or Wolframite) are used to synthesize single phase or pyrochlore-free perovskite relaxors, via the conventional solid-state reaction process [114, 115]. Many chemistry-based methods, such as co-precipitation, sol-gel, gel combustion and molten salt, have also been developed to produce phase-pure ultra-fine powders of relaxor ferroelectrics [116-121]. Comparatively, high-energy mechanochemical activation has been shown to be an alternative and effective process to prepare a wide range of phase-pure relaxor ferroelectric materials.

Typical relaxor ferroelectrics include lead magnesium niobate [$Pb(Mg_{1/3}Nb_{2/3})O_3$ or PMN], lead zinc niobate [$Pb(Zn_{1/3}Nb_{2/3})O_3$, or PZN], lead iron niobate [$Pb(Fe_{1/2}Nb_{1/2})O_3$ or PFN] and lead scandium tantalate

[$Pb(Sc_{1/2}Ta_{1/2})O_3$ or PST] (PMN), etc.. Base on these basic relaxors, modifications by addition of other components such as PT, PZT, BT ($BaTiO_3$) and ST ($SrTiO_3$) or combination with each other have led to tremendous new types of materials with binary or ternary compositions. The following discussion is arranged in the order of monophase, binary and ternary. At the end of this section, order-disorder transition in some relaxor ferroelectrics, as a result of high-energy mechanical activation, will be described.

3.2.1. Monophase

3.2.1.1. PMN

Pyrochlore-free nano-sized PMN powders have been directly synthesized from the mixture of PbO, MgO and Nb_2O_5 powders, using SPEX shaker-mill (stainless steel) [122-127] and planetary high-energy ball mill (tungsten carbide) [128, 129]. Nanosized PMN powders can be produced either from oxide precursors [122-124, 128, 129] or coprecipitation-derived amorphous precursors [125]. Fig. 32 shows the XRD patterns of the oxide mixture for PMN milled for different times, reported in Ref. [128]. 3-h-milling does not lead to the formation of PMN, while PMN phase appears after milling for 9 h. Single phase PMN is readily obtained after milling for 20 h. Further milling results in no changes in the phase composition. SEM observation indicated that the powders possess similar particle morphology and grain size as the samples were milled for longer than 9 h. Dense PMN ceramics can be fabricated by sintering the PMN powders at 900 ℃. Cross-sectional SEM images of the PMN ceramics sintered at different temperatures are shown in Fig. 33 [128]. Dielectric and ferroelectric parameters of the sintered PMN ceramics are listed in Table 5, which are in good agreement with the literature values. Similar results were also reported in Ref. [122].

The formation mechanism of phase-pure PMN via the high-energy ball milling process is quite different from that via the solid-state reaction of oxides. The reaction is very complex in the solid-state process, where perovskite phase of PMN is not directly formed from the oxides [116, 117]. PbO and Nb_2O_5 firstly react at about 500°C resulting in a cubic pyrochlore ($Pb_3Nb_4O_{13}$). The cubic pyrochlore compound further reacts with PbO leading to a rhombohedral pyrochlore ($Pb_2Nb_2O_7$) at about 600°C. $Pb_2Nb_2O_7$ then reacts with MgO to form perovskite PMN, with the appearance of $Pb_3Nb_4O_{13}$ at higher temperature of 800°C. Although the amount of $Pb_3Nb_4O_{13}$ phase can be reduced by adding excessive amount of PbO and MgO, it is very difficult to obtain single phase PMN by the conventional solid-state process [116, 117]. However, this problem is readily addressed by using the high-energy ball milling technique. The high-energy ball milling technique provides the milled system with energies high enough to trigger the reaction directly, avoiding the formation of pyrochlore phases, which are usually formed at high temperatures. Therefore, the mechanism that governs the formation of PMN via the mechanochemical activation is different from that of the solid state reaction.

3.2.1.2. PZN

It is of particular interest to produce single-phase PZN powder via a mechanical milling process because no one has succeeded in trying to synthesize phase-pure PZN powder by either the conventional solid-state reaction process or chemistry-based routes. So far, molten salt flux is the only technique to grow phase-pure PZN in the form of single crystal. This is because that the conventional solid-state reaction process and most chemistry routes require calcination temperatures of 600-900 ℃. In this temperature range, PZN is unstable. The fact that PZN crystal can be grown in PbO flux at high temperature is due to the unequilibrium state.

Phase formation of PZN was reported by Shinohara *et al* [160], where the authors used a soft-mechanochemical route to prepare PMN-PZN ceramics. Although they noted the formation of perovskite PZN by the mechanical milling, they didn't pay much attention to the observation and made no attempt to synthesize phase-pure PZN powder. The synthesis of perovskite PZN via mechanochemical process was formally reported by Wang *et al* [130, 131]. They found that nanocrystalline PZN powders can be synthesized either from oxide mixture of PbO, ZnO and Nb_2O_5 or a mixture of PbO and $ZnNb_2O_6$. The phase evolution of PZN is similar to that of PT, PZT and PMN, as discussed above. Figs. 34 and 35 show the XRD patterns of the two groups of mixtures milled for various durations. Single phase PZN can be formed in the two systems after milling for 20 h in the oxide mixture and 15 h in the mixture of PbO and $ZnNb_2O_6$, respectively [130]. The synthesized powders have an average grain size of 10-15 nm, with an amorphous layer of 2-5 nm at the boundaries of the PZT nanosized crystallites, as evidenced by TEM examination reported in Ref. [131]. The formation of single phase PZN indicates again the difference in formation mechanism between mechanochemical synthesis and conventional solid state reaction process. However, due to its poor thermal stability, the PZN powder cannot be sintered into phase-pure ceramics. Therefore, no electrical property is available for the synthesized PZN. It is thus concluded that the PZN phase produced by the mechanical activation is a thermally metastable phase, which decomposes at high temperatures.

3.2.1.3. PFN and PFW

Lead iron niobate [$Pb(Fe_{1/2}Nb_{1/2})O_3$, or PFN) and lead iron tungstate [$Pb(Fe_{2/3}W_{1/3})O_3$ or PFW] are important relaxor ferroelectric materials [132-136]. Due to their high dielectric constants, broad ferroelectric-paraelectric phase transition, and especially relatively low sintering temperature, PFN and PFW have been acknowledged to be promising candidates for application of multilayer ceramic capacitors (MLCs). The low sintering temperature of PFN and PFW makes it possible to use low melting temperature inexpensive inner electrodes, leading to a significant reduction in the cost of MLCs products.

Also, these iron containing ferroelectric materials are of particular interests due to their possible magnetic properties. For example, PFN has a diffuse ferroelectric phase transition at ~380 K and an antiferromagnetic phase transition at ~145 K. PFW ceramic sample demonstrates a Curie temperature (T_C) of ~175 K and antiferromagnetic-to-paramagnetic at ~340 K [134]. These multiferroic magnetoelectric materials simultaneously show electric and magnetic polarizations. The coupling between ferroelectric and magnetic activity offers the possibility to manipulate the magnetic properties through electric field and *vice versa*, making these materials potential for a wide range of applications in spintronics, multiple state memory elements or memory devices, which use electric and/or magnetic field for read/write operations [134].

The synthesis of iron containing relaxor ferroelectric phases, via high-energy mechanical milling process, has been demonstrated by Wang *et al* [137-140]. Unlike PMN and PZN, the formation of PFN and PFW follows a relatively complicated reaction sequence.

It has been shown that single phase PFN powder can be formed from oxide mixture via a mechanical activation. But PFN ceramics derived from this PFN powder demonstrated poor microstructural and electrical properties. High performance PFN ceramics can only be obtained from the columbite precursor of PbO and $FeNbO_4$. Figs. 36 and 37 show the XRD patterns of the mixture of PbO, Fe_2O_3 and Nb_2O_5, and the mixture of PbO and $FeNbO_4$, milled for various time durations, respectively [137]. The two mixtures undergo similar reaction sequences. Perovskite PFN is formed after milling for 5 h and the phase formation almost finishes after

10 h, while single phase PFN can be achieved after milling for 30 h. The two products both have an average particle size of <35 nm, with a similar particle morphology. DTA (differential thermal analysis) and XRD results indicated that the powders showed different thermal stabilities. A trace of pyrochlore phase was detected in the PFN powder derived from the oxide mixture after firing at 500 ℃. The pyrochlore phase was stable up to 800 ℃ and finally converted to perovskite phase at 1000 ℃. In contrast, there was no any pyrochlore phase observed in the PFN sample made from the mixture of PbO and $FeNbO_4$. Raman spectra of the two powders showed that the PFN powder derived from the oxide mixture contains small amount of Fe_2O_3, while the powder from the mixture of PbO and $FeNbO_4$ was almost phase pure. It means that the reaction activated by the mechanical milling in the oxide mixture was not complete after milling for 30 h. The presence of the unreacted Fe_2O_3 was not detected by the XRD measurement which is mainly due to the limited sensitivity of the XRD analysis. The residual oxides are responsible for the presence of pyrochlore phase in the sample from the oxide mixture upon thermal treatment. The powders derived from different precursors lead to different microstructures and subsequent electrical properties of the PFN ceramics. The maximum relative density of the PFN ceramics from the oxide mixture is not higher than 93%, while almost fully dense PFN samples can be obtained from the columbite precursor (99%). Fig. 38 [137] shows the SEM images of the 1000 ℃-sintered PFN ceramics made from the 30-h-milled oxide mixture and the columbite precursor of PbO and $FeNbO_4$, respectively. The sample from the oxide mixture has a more porous structure with larger grain size than that from the columbite precursor. This can be related to the characteristics of the PFN powders. The involvement of a pyrochlore phase due to the presence of the residual oxides in the powder from the oxide mixture created pores as it converts into perovskite phase during the sintering at high temperatures, since the molar volume of the pyrochlore phase is larger that that of the perovskite phase. Kirkendall swelling due to the composition inhomogeneity is another contribution to the porous microstructure of the oxide-mixture derived PFN ceramics, since the residual oxides have different diffusion rates. The two PFN ceramics showed similar dc conductivity, dielectric constant and loss tangent as the sintering temperature is lower than 1100 ℃. For the samples sintered at temperature higher than 1100 ℃, the PFN ceramics derived from the oxide mixture are very conductive, with extremely high dielectric conductivity and loss tangent, as compared to those derived from the mixture of PbO and $FeNbO_4$. The high conductivity of the PFN ceramics from the oxide mixture has been attributed to the hopping conduction of charge carriers in association with Fe^{2+}/Fe^{3+}. The interaction between the residual Fe_2O_3 and Fe contamination is responsible for the formation of Fe^{2+}/Fe^{3+} couple. This explanation seems to be quite arguable. As mentioned earlier, the residual oxides (including Fe_2O_3) reacted to PFN at 1000 ℃. In other words, at temperature higher than 1100 ℃, no Fe_2O_3 is available to form Fe^{2+}/Fe^{3+} with iron. In fact, iron contamination has already oxidized at such high temperature. Therefore, if Fe^{2+}/Fe^{3+} really contributed to the conductivity of the PFN ceramics, the two samples should have similar electrical properties. In this respect, it is suggested that the difference in the electrical properties between the two groups of PFN ceramics is most likely associated with their difference in microstructures due to the different properties of the PFN powders. At least, the Fe^{2+}/Fe^{3+} conduction is not the only factor that determines the electrical properties of the PFN ceramics. The porous microstructure of the PFN ceramics from the oxide mixture makes it easy to absorb water vapor or trap other contaminations, which could increase the conductivity of the porous PFN ceramics. In contrast, the samples made from the columbite precursor have dense microstructure and thus low dc conductivity and reasonable dielectric constant and loss tangent.

Unlike PFN, PFW cannot be directly synthesized from oxide mixture of PbO, Fe_2O_3 and WO_3 by using a mechanochemical activation [138]. Instead, nanocrystalline lead tungstate ($PbWO_4$) and pyrochlore ($Pb_2FeWO_{6.5}$) are formed in the oxide mixture as a result of the mechanical activation. However, the subsequent thermal treatment showed that the reactivity of the milled oxide mixture is enhanced for the formation of PFW perovskite phase. This is not surprising because the precursor have been significantly refined as a result of the high-energy milling. XRD patterns of the 20-h-milled oxide mixture of PbO, Fe_2O_3 and WO_3 annealed at different temperatures are shown in Fig. 39. Phase pure PFW is formed after firing at 700 ℃, which is 50 ℃ lower than that required by its unmilled counterpart, as shown in Fig. 40. Although the reduction in calcination temperature leading to the formation of perovskite PFW phase is not very significant, the milled powders result in PFW ceramics with much better electrical properties as compared to those from the unmilled samples. PFW ceramics, with high density, uniform microstructure and better dielectric properties, are obtained from the milled powders, while the ceramics derived from the unmilled mixture have high porosity, rough microstructure and poor electrical properties. This observation is similar to that observed in PFN.

It is very interesting to find that single phase PFW can be formed from oxide mixture of PbO, Fe_2O_3 and WO_3 with 0.4 mol PFW seeding powder, via a high-energy mechanical activation [139]. The PFW seeds were synthesized by the conventional solid state reaction process. Figs. 41 and 42 plot the XRD patterns of the oxide mixture of PbO, Fe_2O_3 and WO_3 with and without PFW seeds, before and after mechanical milling. As discussed above, 20-h mechanical activation leads to the formation of $PbWO_4$ and $Pb_2FeW_{6.5}$ in the oxide mixture, without the formation of perovskite PFW. In contrast, single phase PFW is produced from the 0.4-mol PFW seeded mixture by mechanical activation for 20 h. Comparatively, although perovskite PFW appears essentially as major phase, a trace of $PbWO_4$ is still detected in the 0.3-mol-seeded mixture after milling for 20 h. Therefore, 0.4 mol PFW is a critical amount to produce single phase PFW from oxide mixture. The PFW seeds provided nuclei for the formation of perovskite PFW from the mixture during the high-energy activation. The nuclei also prevented the formation of pyrochlore and other intermediate phases during the milling. The seeding effect was also confirmed by the results of calcination of the seeded and unseeded mixture after milling for 20 h [139]. With the presence of the PFW seeds, intermediate pyrochlore phase $Pb_2FeO_{6.5}$ is not found before the formation of PFW.

One may notice that the seed concentration required by the mechanochemical process here is much higher than those required by precipitation in liquid solution and solid-state reactions, where the seeding levels are mostly less than 1%. This is because the diffusion rate of species in a liquid solution or in a solid state at high temperature is much higher than that in the case of the high-energy milling, since the milling was carried out at relatively low temperatures. Although the exact temperatures of ceramic materials during high-energy milling process are rarely reported, they must be much lower than those used in solid-state reactions. For example, it is reported that the overall temperature rise for mechanical alloy of Al-Mg using a SPEX 8000 mill is always less than 200 ℃ [11]. This observation again indicates that the reactions induced by the high-energy mechanochemical process are different from the reactions in low-temperature liquid solutions and high-temperature solid-state systems.

Attempt has also been made to synthesize PFW from pre-formed constituents [138]. The first example is to use the mixture of PbO and Fe_2WO_6. Unlike the oxide mixture, intermediate phase such as $PbWO_4$ and $Pb_2FeWO_{6.5}$ did not appear in the mixture of PbO and Fe_2WO_6 after high-energy mechanical milling. However,

PFW cannot be formed between PbO and Fe_2WO_6. The activation only results in significant refinement and amorphization of the starting components. This occurrence was attributed to the fact that Fe_2WO_6 phase is more stable than perovskite PFW, $PbWO_4$ and $Pb_2FeWO_{6.5}$ under the mechanochemical activation. In other words, the reaction between PbO and WO_3 might be much easier than reactions between/among other constituents. It was then suggested to use $Pb_3Fe_2O_6$ and WO_3 as the starting materials. Single phase PFW was really obtained. Fig. 43 shows the XRD patterns of the mixture of $Pb_3Fe_2O_6$ and WO_3, milled for different time durations [140]. After milling for 1 h, perovskite phase is already observed, while 4-h-milling results in single phase PFW. Further milling only leads to slight enhancement of the crystallinity of the perovskite phase. This time duration is much shorter than that required by the 0.4 mol PFW seeded mixture. PFW ceramics made from this PFW powder also showed good microstructural and electrical properties.

In summary, phase formation of PFW via the high-energy mechanochemical activation demonstrates a rich feature. Single phase PFW can be obtained neither from the oxide mixture of PbO, Fe_2O_3 and WO_3 nor from the mixture of PbO and Fe_2WO_6. 20-h-milling leads to the formation of $PbWO_4$ and $Pb_2FeWO_{6.5}$ in the oxide mixture and refinement/amorphization in the columbite mixture. It is possible to produce PFW from the oxide mixture with 0.4-mol-PFW seeding or the combination of $Pb_3Fe_2O_6$ and WO_3. Furthermore, PFW formation from the later requires only 5-h activation, which is much faster than that required by the seeded mixtures.

3.2.1.4. PST

Lead scandium tantalate [$Pb(Sc_{1/2}Ta_{1/2})O_3$ or PST] is a typical candidate for investigating the relationship between structural ordering and electrical characteristic of relaxor [141, 142]. Ordered PST behaves as a normal ferroelectric material, whereas disordered PST is a relaxor having properties such as frequency dependent dielectric constant and broad phase transition temperature range. The degree of the B-site ordering in PST can be controlled by thermal annealing, which has been acknowledged to be a very useful way to tailor the electrical properties of PST. The definition and characterization of B-site ordering and disordering will be discussed later (section 3.2.4.)

Single phase PST of perovskite structure has been synthesized from oxide mixture via a mechanical milling [143]. 20-h-milling leads to the formation of single phase PST. However, although the PST phases derived from the mechanical activation and the solid-state reaction both possess the perovskite structure, they have different ordering characteristics. As shown in Fig. 44, an essential superlattice reflection (111), an indication of ordering characteristic, is observed in the sample derived from the Wolframite precursor via the conventional solid-state reaction process, while no such peak is detected in the mechanochemically synthesized phase. The former has an ordering parameter of 0.729, in contrast to a totally immeasurable order parameter of the later. Due to the high sinterability, the mechanical activated derived PST sample has a relative density of 97.1%, as compared to 92.6% of the ceramics made from the Wolframite precursor. After sintering at 1200 ℃ for 2 h, their ordering factors increase to 0.764 and 0.23, respectively. The difference in the disordering characteristics between the PST ceramics is also confirmed by the difference in their dielectric properties [141]. As shown in Fig. 45, the 1200 ℃-sintered PST ceramic sample derived from the 20-h-activated oxide mixture demonstrates a typical relaxation behavior. A maximum dielectric constant of ~14000 was measured at 0.1 kHz, with a dielectric loss tangent of 0.032, which are better than the dielectric properties of its Wolframite counterpart. The most significant aspect of these observations is that the disordering character in the mechanical activated PST can be retented after sintering at high temperatures. Therefore, the mechanochemical technique

offers us an effective and simple way to prepare disordered PST ceramics, without any special treatments used in the conventional solid-state reaction process.

3.2.2. Binary-phase

Numerous binary systems have been created through the combination of relaxors with ABO_3 compounds, such as BT, ST and PT. Combination of relaxor and relaxor is also an effective way to produce materials with desired electrical properties. Representative binary phases, such as PMN-PT [144-148], PZN-BT [153-156] and PMN-PFN [161], will be discussed to show the feasibility of high-energy mechanical activation in synthesizing ferroelectric materials. Three subsections, i. e. PMN family, PZN family and relaxor-relaxor combination, will be discussed.

3.2.2.1. PMN family

(1-x)PMN-xPT binary phases with different compositions demonstrate various dielectric, ferroelectric and piezoelectric properties [144-146]. 0.9PMN-0.1PT is a pronounced candidate to replace BT ($BaTiO_3$) in MLCs (multilayer ceramic capacitors) because it has lower sintering temperature as well as higher dielectric constant than BT. It is also one of the best candidate materials for devices of actuators because of its large electrostrictive and piezoelectric coefficients. (1-x)PMN-xPT system has also a morphotropic phase boundary (MBP) [144-146], similar to that in PZT family [1]. The piezoelectric properties of the (1-x)PMN-xPT system, however, are much higher that of PZT system. 0.65PMN-0.35PT has been shown to exhibit the highest piezoelectric properties among various ferroelectric materials, thus making it important for applications of many actuators and sensors [144-146].

The work reported by Baek *et al* [148] is probably the first example in applying mechanochemical process to synthesis of 0.9PMN-0.1PT, where the authors used a soft mechanochemical route (low-energy) to improve the phase formation of 0.9PMN-0.1PT from a mixture of PbO, TiO_2, $Mg(OH)_2$ and Nb_2O_5. After milling for only 60 minutes, the powder was then processed following the traditional ceramic process in order to obtain 0.9PMN-0.1PT ceramics. They found that the perovskite phase formation, densification behavior and thus the dielectric properties of the 0.9PMN-0.1PT ceramics derived from the 60-min-milled precursors are much better than those of the samples made from the unmilled powders. In fact, formation of perovskite phase was already observed in the 60-min-milled precursor and the authors did mention in the work [148]. The perovskite phase formed as a result of the soft mechanical treatment might act as seeds that suppressed the formation of pyrochlore phase.

More recently, it has been reported that simple phase nanocrystalline 0.9PMN-0.1PT powders can be directly synthesized from oxide precursors via high-energy mechanical milling process [147, 149]. The phase evolution of PMN-PT follows a similar pattern of PMN, as discussed above. The presence of pyrochlore phase is not observed. As summarized in Table 6, the 0.9PMN-0.1PT ceramics, derived from the high-energy mechanically synthesized nano-sized powders, demonstrated very promising dielectric and ferroelectric properties [144-146].

Synthesis of (1-x)PMN-xPT with high concentration of PT was reported by Alguerό *et al* [150] and Kong *et al* [149]. Alguerό *et al* [150] synthesized PMN-0.20PT and PMN-0.35PT powders and obtained ceramics from the powders using pressureless sintering and hot pressing sintering. Their PMN-0.35PT was single phase with a perovskite structure, while a slight trace of pyrochlore phase was observed in the PMN-0.20PT sample. No explanation has been given to the presence of pyrochlore phase in the literature [150]. Noting

that single PMN can be readily derived from oxide precursors, as reported by Wang *et al* [122] and Kong *et al* [128], the formation of the pyrochlore phase in PMN-0.20PT systems is unexpected. It is mainly due to the poor homogeneity of the starting oxide powders. In this respect, it is necessary to mention that the homogeneity of starting components is an important factor in synthesizing single phase compounds like PMN or PMN-PT, via a mechanochemical process.

Normally, the formation of single phase PMN and PMN-PT from oxide precursors required 20-h-milling, using either a planetary mill [128] or a shaker mill [122]. It is found, however, that rapid phase formation of PMN-PT can be realized by simply increasing milling speed. As shown in Fig. 46, the oxide mixtures have been transferred to single phase 0.90PMN-0.10PT and 0.65PMN-0.35PT after milling for only 2 h, at a milling speed of 250 rpm [149]. Compared to general case of 200 rpm, the speed is increased by only 50 rpm, the milling time duration required for the phase formation is shortened greatly. However, very high milling speed is not recommended because temperature rise is too fast. If the heat created during the high speed milling cannot be dissipated to environment, it might damage the milling tools.

It has been found that translucent PMN and PMN-PT ceramics can be obtained from the synthesized powders [129], by using the process to produce transparent PLZT8/65/36 ceramics as presented above [96]. The powders were sintered at 950 ℃ first to have fully dense PMN and PMN-PT ceramics. The sintered ceramics were then annealed at 1100 ℃ for 6 h, which was repeated for 4 times. Fig. 47 shows the variation in the average grain sizes of PMN and PMN-PT ceramics as a function of annealing duration. The average grain sizes were estimated from SEM images of the thermally etched surface of the samples. For the 6-hour-annealed samples, the average grain sizes of PMN, 0.90PMN-0.10PT and 0.65PMN-0.35PT are 0.6, 1.1 and 1.3 μm, respectively. When the annealing time duration increases to 12 hours, the grain size sharply increases to 2.2, 1.9 and 1.8 μm for PMN, 0.90PMN-0.10PT and 0.65PMN-0.35PT, respectively. Further increase in annealing duration leads to only slight increase in grain size for all three samples. Grain growth at a certain temperature follows kinetic equation [162]: $D_t^n - D_0^n = kt$ (where k is a constant, D_0 and D_t are the initial grain size and grain size after time t. n is the exponential constant which is 2-4 depending on both the properties of materials investigated and the parameters used to anneal them). Accordingly, grain size always increases with annealing time. This satisfactorily explains the increase in grain size from 6-hour annealing to 12-hour annealing. The fact that the grain growth slows down as the annealing time increases from 12 hours to 24 hours is mainly related to the volatilization of PbO. This is confirmed by the XRD patterns of the PMN ceramics annealed for different time durations, as shown in Fig. 45. It is noted that perovskite phase in PMN ceramics is stable after annealing for 12 h (Fig. 48 (a) and (b)). Prolonged duration of annealing leads to the formation of pyrochlore phase (Fig. 48 (c)). The amount of pyrochlore phase slightly increases with increasing annealing time duration (Fig. 48 (d)). The appearance of the pyrochlore phase is readily attributed to the volatilization of PbO from the perovskite matrix, which can be expressed as following:

$$Pb(Mg_{1/3}Nb_{2/3})O_3 = 1/6Pb_3Nb_4O_{13}+1/2PbO+1/3MgO \quad (1)$$

This observation implies that, at early stage of annealing, excess PbO (used in the starting mixtures) remained in grain boundaries or grain junctions volatilized. After annealing for 12 hours, excess PbO is almost

depleted. As annealing time increases to 18 hours, PbO will escape from lattice site of PMN or PMN-PT, which caused the decomposition from perovskite to pyrochlore and inhibited grain growth of the samples. In other words, 12-hour annealing is an optimized time duration in order to eliminate the excess PbO and to get translucent PMN-PT ceramics. Representative translucent samples of the PMN and PMN-PT ceramics are shown in Fig. 49. The thickness of the ceramic pellets is 0.3 mm. the transmittances at 600 nm wavelength for the 12-h-annealed (two times) samples are 21, 16 and 11% for PMN, PMN-0.10PT and PMN-0.35PT, respectively. The transmittance decreases with increasing PT content. The translucent characteristics of the PMN and PMN-PT ceramics, together with other electrical properties, might hopefully find uses in electro-optical device applications, like PLZT ceramics.

3.2.2.2. PZN family

As discussed above, although single phase PZN powder has been synthesized from oxide precursor via mechanical activations, it is impossible to have phase pure PZN ceramics from the synthesized powder since it is not stable at high temperatures. However, it has been reported that perovskite structure of PZN can be stabilized by the addition of $BaTiO_3$ (BT) [152], $SrTiO_3$ (ST) [153] and $PbTiO_3$ (PT) [153, 154] to form binary solid-state solutions of PZN-BT, PZN-ST or PZN-PT, via the conventional ceramic process [152, 153] or single-crystal growth [154]. PZN based binary materials have many outstanding properties. For example, 0.91PZN-0.09PT, which is near the morphotropic phase boundary (MPB) at room temperature shows a surprisingly large dielectric and piezoelectric constant and higher electromechanical coupling coefficient than the PZT family of ferroelectrics. Among various additives, BT is the most effective additive to suppress the formation of pyrochlore phase in PZN binary ceramic materials. (1-x)PZN-xBT with x=0.05-0.30 have been synthesized via high-energy mechanical milling process [155-158].

Wang *et al* [157, 158] reported that single phase 0.95PZN-0.05BT and 0.90PZN-0.10BT can be synthesized after milling for 15 h and 10 h. It means that the more BT contained the easier the perovskite formed. The synthesized 0.95PZN-0.05BT powder demonstrates an interesting thermal stable characteristic. Fig. 50 illustrates the percentage of perovskite phase in the 20-h-milled mixture of PbO, ZnO, Nb_2O_5, BaO and TiO_2, after calcining at temperatures ranging from 450 to 1150 ℃ for 1 h. The percentage of perovskite phase is estimated from the diffraction intensities of perovskite (110) and pyrochlore (222) peaks, using equation $\%perovskite=100I_{perov}(110)/[I_{perov}(110)+I_{pyro}(222)]$ [157]. The mechanochemically derived PZN-0.05BT powder starts decomposing at 450 ℃ and the decomposition increases with increasing firing temperature. Perovskite percentage reaches its lowest value of ~20% after calcining at 700 ℃ for 1 h and then increases thereafter. A significant recovery of the perovskite phase is found at 900 ℃. The final value of perovskite percentage is 94% at 1100 ℃. The decomposing behavior of the PZN-0.05BT powder below 700 ℃ has been considered to be the decomposition of PZN, whereas BT was not yet formed in the activated sample. BaO was converted into $BaCO_3$ due to the absorption of CO_2 from air, which is supported by FTIR measurement. At a certain temperature, about 800 ℃, BT was formed and thus its stabilizing effect started to function. As a result, perovskite phase is recovered and the recovery was favored by increasing temperature. However, this does not well explain the cases of high BT concentrations reported in Ref. [155]. Fig. 51 shows the XRD patterns of the 12-h-milled mixtures of PbO, ZnO, Nb_2O_5, $BaCO_3$ and TiO_2 for (1-x)PZN-xBT with x=0.05-0.30 [155]. If BT is not incorporated with PZN to form a solid solution of PZN-BT, $BaCO_3$ should be able to be detected by the XRD analysis. But no $BaCO_3$ can be observed even in the sample with BT concentration of 0.3. This observation at least indicates that

solid solution PZN-BT is formed in the cases of high BT concentrations. To understand this phenomenon, information on the thermal stabilities of all the PZN-BT samples is required. Such information is not available in the literatures to date. Nevertheless, single phase PZN-BT ceramics with perovskite structure can be readily obtained from the milled precursors. As will be discussed later, single phase BT cannot be obtained from the mixture of $BaO/BaCO_3$ and TiO_2 via a high-energy ball milling, but high-energy milling can reduce the formation temperature of BT [180, 181]. Recalling that PZN can be formed by a mechanochemical activation but is not stable at high temperature, it is reasonable to suggest that the formation of the PZN-BT perovskite structures by the high-energy milling is due to the formation of PZN, while they are stable at high temperatures due to the presence of BT. Similar occurrence will be observed in other binary/ternary systems containing PZN component [161].

Fig. 52 illustrates the XRD patterns of the (1-x)PZN-xBT ceramics sintered at 1050℃ for 1 h. All samples with x=0.10 to 0.30 are of single phase perovskite structure [155]. About 5% pyrochlore phase is detected in the 0.95PZN-0.05BT ceramics. Basically, oxide perovskites are ionic compounds. To form a stable perovskite structure of ABO_3 compound, the ionic radii of the cations should be within proper limits and the elements should form strong mutual ionic bond. In addition to this, the stability of perovskite structure is also determined by the degree of ionic character of the chemical bonds in the compound. The percentage of ionic character of the bonds is proportional to the electronegativity difference between cations and anions. Since $BaTiO_3$ has the largest electronegativity difference and tolerance factor it is the most effective candidate to stabilize PZN perovskite structure. It has been reported that the amount of $BaTiO_3$ enough to stabilize PZN in perovskite form is 6 to 7%. 85% perovskite can be achieved in 5% $BaTiO_3$ stabilized PZN system using conventional solid-state reaction process [152]. So the presence of 5% pyrochlore phase in our 0.95PZN-0.05BT ceramics derived from the high-energy ball milled powders is reasonable. This is consistent with that of the PZN-0.05BT derived from the powder produced using a shaker mill [157].

To simplify the calculation of lattice parameters, the structures of perovskite-like solid solutions are usually treated as cubic lattices. For example, the true lattice structure of $PbZr_{1-x}Ti_xO_3$ at $0.10<x<0.40$ is rhombohedral with a axis of 4.13 Å and the deviation of the rhombohedral angle from 90 °by only 16', which is very close to cubic structure [228]. Due to the overlapping of diffraction lines, it is difficult to precisely determine the lattice parameters. Similarly, the (1-x)PZN-xBT ceramics are considered to be of pseudocubic structure. By doing so, the lattice constant of the (1-x)PZN-xBT ceramics can be estimated from the XRD patterns shown in Fig. 52, which are plotted in Fig. 53 [155]. The lattice constant decreases almost linearly as a function of the content of BT, since the (1-x)PZN-xBT ceramics are solid-solutions of PZN and BT. This is in agreement with the fact that PZN (JCPDS 22-662) with a cubic structure has a lattice constant a=4.062 Å, whereas the lattice constant of cubic PT (JCPDS 31-174) is a=4.031 Å.

Cross-sectional SEM images of the (1-x)PZN-xBT ceramics are shown in Fig. 54 [155]. The grain sizes of the PZN-BT ceramics were estimated from the SEM images and are listed in Table 7, together with their relative densities. The 5%-BT contained PZN-BT sample exhibits more or less irregular grain morphology as compared to the samples with high level of BT. The irregularity of the grains in the 0.95PZN-0.05BT ceramics is related to the presence of the pyrochlore phase. Well-developed grains are observed in other five samples. The grain size decreases with increasing content of BT. This observation may be due to the fact that the sintering temperature of BT is higher than that of PZN. It means that BT should be sintered at higher temperature than

PZN to achieve similar grain size. Since the samples were sintered at the same temperature (1050 ℃), the increase in BT content results in a decrease in grain size. Additionally, the dielectric constants of the (1-x)PZN-xBT ceramics derived from the high-energy mechanical milled powders are in a good agreement with the reported values in the literatures.

This achievement demonstrates that the high-energy mechanochemical technique is advantageous over some of the chemical processing routes for the preparation of PZN based ceramics. For example, a new aqueous solution-gel method was recently developed by Werde *et al* to synthesize perovskite 0.75PZN-0.25BT [159], where PZN acetate citrate precursor was combined with an aqueous BT precursor. Although high chemical homogeneity was found in the mixture, the maximum weight percentage of perovskite was 96%, which was only achieved under proper thermal treatment (14 min calcination at 800 ℃ after at fast firing rate of 50 ℃/min). Comparatively, the mechanochemical process is much simple and effective.

Another example of PZN family is $0.92Pb(Zn_{1/3}Nb_{2/3})O_3$-$0.08PbTiO_3$ (0.92PZN-0.08PT) reported by Castro *et al* with a focus on the formation mechanism and thermal stability of the perovskite phase synthesized via a mechanosynthesis process [242]. The authors started with oxide constituents (PbO, ZnO, Nb_2O_5 and TiO_2) and used a Pulverisette 6 model Fritsch planetary mill operating at 300 rpm. All mechanochemical treatments were conducted in air for up to 140 h. It was found that PbO persisted after milling for 20 h and incipient perovskite PZN-PT formation took place after milling for 10 h. Perovskite PZN-PT became major phase after 20 h and single phase perovskite was achieved after milling for 30 h. Prolonged milling time duration from 30 to 70 h led to a slight increase in intensity of the perovskite peaks, which could be attributed to the enhanced crystallization of the perovskite phase. Further milling for up to 140 h did not result in further change in XRD pattern of the powders. A careful examination indicated that the diffraction peak (110) shifted to high angle with increasing milling time duration (from 30 h to 140 h), which implies that the perovskite cell was shrunk. There was no significant difference in grain size among the samples milled for different time durations.

The formation mechanism of the PZN-PT perovskite phase was studied by a combination of XRD and TEM. During the first hour of milling, ZnO, Nb_2O_5 and TiO_2 particles were amorphized during the initial hours of activation. Nanometer-scale chemical homogeneity was formed after milling for 20 h. An increasing level of agglomeration was then developed. Perovskite phase was formed within the agglomerates and full cryatallinization was obtained after 70 h. The cell contraction was ascribed to the contamination of Fe during the milling process. This formation mechanism is similar to that of PT, PZT and PZN proposed by Wang et al [130, 131, 147].

The perovskite PZN-PT synthesized after milling for 30 h was only stable up to 400 ℃ and started to decompose into pyrochlore phase ($Pb_{1.88}Zn_{0.3}Nb_{1.25}O_{5.305}$) at 500 ℃. The authors also found that the thermal stability of the perovskite PZN-PT could be enhanced up to 600 ℃ by a pressure of 50 MPa. The thermal stability of the perovskite PZN-PT is similar to that of PZN [130] and PZN-BT [157, 158].

3.2.2.3. Relaxor-relaxor combination

Relaxor-relaxor combination has shown many particular interests. For example, PMN has a Curie temperature T_C of ~50ºC, where as PZN's T_C is ~140 ℃. It is, therefore, possible to make a relaxor with T_C close to room temperature by combining PMN and PZN. This kind of material is expected to have very high room temperature dielectric constant, which is important for the fabrication of small dimension ceramic capacitors with high values of capacitance [161]. Although normal ferroelectrics such PT, BT or PZT can be used to

modify the properties of relaxors, they alter the relaxor characteristics at the same time. For example, with increasing concentration of BT, PZN-BT will become normal ferroelectric gradually. As discussed above, single phase PFW cannot be directly synthesized from oxide mixture via a mechanochemical process, but the mechanically activated mixture can be used to fabricate PFW ceramics because single phase is formed at high temperature. In contrast, PZN has been successfully derived from the oxide mixture. However, PZN is not stable at high temperature. It is expected that an appropriate combination of PFW and PZN might lead to a relaxor that can be obtained from oxide mixture via a mechanochemical activation and is also stable at high temperatures. so that PZN-PFW ceramics Successful applications of mechanochemical synthesis to these kinds of relaxor binary systems will be presented as following.

Shinohara *et al* [160] reported the phase formation and electrical properties of PMN-PZN binary relaxor ceramics, derived from precursors of PbO, $Mg(OH)_2$, Nb_2O_5 and $2ZnCO_3·3Zn(OH)_2·H_2O$, treated by a soft-mechanochemical processing. It was found that perovskite phase was formed even after milling for only 30 min and became major phase after 3 h of milling. About 80% perovskite phase was achieved for (1-x)PMN-xPZN with $x \leq 0.9$ and ~60% for pure PZN. The thermal stability of the as-milled PMN-PZN powder is greatly dependent on the content of PZN. With increasing PZN, the thermal stability of the PMN-PZN decreases. For example, at x=0.9, perovskite percentage decreases from ~80% for the as-milled powder to ~10% after annealing at 700 ℃ for 1 h, while at this temperature pure PZN totally decomposes. The phase evolution of the samples with $x \geq 0.8$ is similar to that of PZN-0.05BT as mentioned above. The perovskite percentage decreases with increasing annealing temperature first, reaches a minimum value at 700 ℃ or 800 ℃, depending on the composition, and then recovers at higher temperatures. However, the sample with x=0.8, the perovskite percentage can only recover to ~50% at 900 ℃, from ~25% at 800 ℃. Fig. 55 [160] shows the perovskite percentage of the 1100 ℃-sintered PMN-PZN ceramics made from the milled powders, as a function of the composition of PZN. Phase-pure PMN-PZN ceramics with x=0.7 can be obtained from the mechanochemically activated powders. This composition is higher than those produced via the columbite ceramic route (x=0.6), which can be attributed to the better homogeneity of the milled precursors, as compared to its unmilled counterpart [160].

Mechanochemical synthesis of (1-x)PFW-xPZN, together with their thermal stabilities and the properties of the ceramics, was reported by Wang *et al* [161]. Fig. 56 shows the XRD patterns of the oxide mixture (PbO, Fe_2O_3, WO_3, ZnO and Nb_2O_5) for (1-x)PFW-xPZN (with x=0-0.5) mechanically activated for 20 h. The percentage of perovskite phase estimated from the XRD patterns is demonstrated in Fig. 57. No perovskite phase is observed in the mixture with x=0, as demonstrated in section 3.2.2.1 [138]. With increasing PZN content x, the amount of perovskite phase increases gradually. Almost single phase is obtained when x=0.5. The thermal stabilities of the perovskite phase in the mechanically activated powders are closely related to the PZN content x. Fig. 58 shows the XRD patterns of the 20-h-milled mixtures of (1-x)PFW-xPZN with x=0.2 and 0.4, annealed at various temperatures [161]. For the sample with x=0.2, the phase is only pyrochlore after annealing at 500 ℃, perovskite as a minor phase is formed at 700 ℃. Single phase perovskite is observed at 800 ℃ and trance pyrochlore appears at 900 ℃. In comparison, at x=0.4, more perovskite phase sustains at low temperature. The amount of perovskite increases while that of pyrochlore decreases as the annealing temperature increases from 500 ℃ to 800 ℃. However, pyrochlore phase cannot be eliminated with further increasing temperature. The relative content of perovskite phase is the PFW-PZN ceramics as a function of PZN content at

different temperatures are clearly shown in Fig. 59 [161]. To sustain 95% perovskite phase, the PZN content cannot be more than 0.2 and the temperature cannot be higher than 850 ℃. The phase evolution of the PFW-PZN samples is also reflected by their microstructural characteristics [161]. The PFW-PZN ceramics demonstrated relaxor ferroelectric properties-diffusive phase transition. Fig. 60 shows the maximum dielectric constant and Curie temperature of the PFW-PZN ceramics as a function of the content of PZN. The increased Curie temperature with increasing PZN content is due to the fact that PZN has a higher T_C than PFW, while the decreased dielectric constant can be readily contributed to the presence of pyrochlore phase in the samples.

It is, therefore, concluded that the content of PZN required to induce the perovskite phase of (1-x)PFW-xPZN, from the oxide mixture, as a result of the high-energy activation, at low temperature, is at x=0.4-0.5, while the stabilization of the perovskite phase at high temperature requires that the PZN content should be less than x=0.3. When compared with PZN-BT system [155-158], one may note that PZN is a better stabilizer in stabilizing BT than PFW during the mechanochemical activation, while BT is better than PFW to stabilize PZN at high temperatures. This interesting observation might be understood in terms of thermodynamic and kinetic characteristics of the two systems, which however is not within the scope of the present review.

3.2.3. Ternary-phase

The electrical properties of relaxor ferroelectrics can be significantly modified using multi-component compositions [163, 164]. Representative ternary systems prepared by the high-energy mechanochemical process are 0.54PZN-0.36PMN-0.1PT and 0.48PFN-0.36PFW-0.16PZN, reported by Wang's group [131, 165-167, 168].

Single phase 0.54PZN-0.36PMN-0.1PT with perovskite structure can be synthesized either directly form the mixture of oxides (PbO, ZnO, MgO, Nb_2O_5 and TiO_2) [131, 165, 166] or the mixture of PbO, TiO_2 and $Zn_{0.6}Mg_{0.4}Nb_2O_3$ [167]. Figs. 61 and 62 show the XRD patterns of the two mixtures mechanochemically activated for various time durations. Similar phase evolution patterns are observed for the two groups, although the starting materials are slightly different. Single phase PZN-PMN-PT powders with perovskite structure with nanometer scale are obtained from the two mixtures after milling for 20 h. PZN-PMN-PT ceramics with full densification can be fabricated from both activated powders. The ceramics demonstrated a relaxor diffuse phase transition in dielectric constant and a frequency dispersion in both dielectric constant and loss tangent, the typical characteristics of relaxor ferroelectrics. The dielectric properties of the groups of PZN-PMN-PT ceramics sintered at various temperatures are summarized in Table 8. It is found that the two groups of samples possess almost the same maximum dielectric constants at Curie temperature, while the room temperature dielectric constants of the ceramics derived from the oxide mixture are higher than those of the ceramics from the columbite precursor by ~1000. This result suggests that it is not necessary to use the columbite precursor to synthesize PZN-PMN-PT powder via a high-energy mechanochemical milling process.

Ternary system 0.48PFN-0.36PFW-0.16PZN, consisting of three relaxors, is another example that can also be synthesized from oxide mixture of PbO, Fe_2O_3, WO_3, Nb_2O_5 and ZnO, using the mechanical activation technique [168]. It is reported that nearly single with the perovskite structure can be obtained from the multicomponent oxide precursors, after milling 20 h. This is markedly in contrast to the case of conventional solid-state reaction process, where second phases such as Pb_2WO_5 and $ZnFe_2O_4$ are often formed during calcination process. Figs. 63 and 64 illustrate respectively the XRD patterns of the unmilled and 20-h-milled oxide mixture for the PFN-PFW-PZN phase, calcined at different temperatures. XRD results showed that almost single-phase of perovskite structure can be achieved after milling for 20 h. Although the two powders experience

similar phase development with calcining temperature, the amount of the pyrochlore phase is obviously less in the later than in the former. Fig. 65 shows the percentage of perovskite phase of the two powders as a function of the calcination temperature, indicating that it is impossible to achieve a single perovskite phase from the oxide mixture without the mechanical activation. It is also observed that the mechanochemical activation demonstrates a positive effect on the densification behavior of the oxide mixture. This effect is the most pronounced at milling duration of 20 h. Prolonged milling (25 h) results in ceramics with lower relative densities, as shown in Fig. 66. It is probably due to the particle agglomeration caused by the prolonged milling. This explanation is supported by the TEM observation of the powders milled for different durations [168]. Almost fully dense PFN-PFW-PZN ceramic has been made from the 20-h-milled powder after sintering at 820 ℃ for 45 min. The high dielectric constant (~9357 at T_C of 27 ℃) of the PFN-PFW-PZN ceramics derived from the 20-h-milled mixture, as compared to that from its unmilled counterpart (<500), once again demonstrates the advantage of high-energy milling in preparing ferroelectric materials.

3.2.4. Order-disordering transition induced by mechanical activation

A schematic diagram, showing an ordered and a disordered crystal structure of $A(B'_{1/2}B''_{1/2})O_3$, is demonstrated in Fig. 67. In the ordered structure (Fig. 67 (a)), sublattice B' or B" can be readily identified, while in the disordered one (Fig. 67 (b)), no sublattice can be established, because B' and B" ions are distributed randomly. The degree of ordering (disordering) is dependent mainly on the difference in size of the two B-site ions and the difference in their valence states. A large difference in size and valence state is favorable to B-site ordering. Depending on their scales of dimension, B-site ordering can be classified into three groups: (i) random cation distribution for coherence length below 2 nm, (ii) short coherence long-range ordering for nanoscale of 2-50 nm and (iii) long coherence ordering of above 100 nm [229].

The degree and nature of B-site ordering (disordering) can be detected by various methods. The main methods that have been reported in the literature include XRD [229], TEM [230-232] and spectroscopic analysis (Raman and Infrared reflection) [233, 234]. XRD is an effective way that has been widely used to characterize the B-site ordering of relaxor ferroelectric materials. The detection of ordering is limited by its volume fraction and by the scattering factor difference between the two B-site ions. Additionally, it is difficult for XRD to monitor the small crystalline regions due to the line broadening. Therefore, XRD is only useful when ordered regions are in the nanometer scales. Compared to XRD, dark field (DF) TEM can detect long range ordered regions down to 3 nm diameter and has been used to characterize short coherence and long range ordering. One of the disadvantages of TEM is its complicated and time consuming process of sample preparations. Spectroscopic techniques, such Raman spectroscopy and IR reflection, provide us a simple way to measure the B-site ordering of relaxor ferroelectrics. The advantages of spectroscopy methods include simple sample preparation and high accuracy when compared to TEM and XRD respectively. However, a combination of two or more methods is usually used to make a more accurate detection [229-236].

As presented above, the PST ceramics derived from the mechanochemically activated oxides demonstrate disordering characteristics. It is also found that an order-disorder transition can be triggered by high-energy activations in the conventionally synthesized ordered powders of monophase PST [169] and binary system $0.4Pb(Mg_{1/3}Nb_{2/3})O_3$-$0.6Pb(Mg_{1/2}W_{1/2})O_3$ (0.4PMN-0.6PMW) [170, 171].

Fig. 68 shows the long range ordering factor of PST as a function of milling duration [169]. The degree of the disordering increases with increasing milling times. Similar to the PST directly derived from the

mechanical activation of the oxide mixture, the disordering property of the solid-state reaction derived PST can also be retained in sintered ceramics, thus leading to a change in ferroelectric transition behavior from a normal ferroelectric to relaxor ferroelectric, as shown in inset of Fig. 68. By considering the fact that the grain sizes of the PST ceramics were far beyond nanometer scale, the authors claimed the disordering and dielectric behaviors in association with the pre-sintering mechanical activation in the sintered PST ceramics were not due to the particle size effect. Although the discussion on the origin of the disordering caused by the high-energy milling is not within the scope of the present review, it is necessary to mention that the milling induced defects, dislocations, microstress, contaminations (very low content) and many other factors should be all taken into account for this issue. Similar result is observed in 0.4PMN-0.6PMW [171]. This finding offers us an opportunity to tailoring the disordering of PST and PMN-PMW and other relaxor ferroelectric ceramics through proper combinations of mechanical activation and subsequent sintering.

3.3. $BaTiO_3$ and its Derivatives

Barium titanate ($BaTiO_3$ or BT) is the first ferroelectric ceramics [1, 172-174], which is a good candidate for a variety of applications, such as piezoelectric actuators, multiplayer ceramic capacitors (MLC) and positive temperature coefficient resistors (PTCR), due to its excellent dielectric, ferroelectric and piezoelectric properties [1].

$BaTiO_3$ powders were conventionally synthesized by solid-state reaction between $BaCO_3$ and TiO_2 at temperatures higher than 1200°C [1]. The high calcination temperature required by solid-state reaction process leads to many disadvantages of the $BaTiO_3$ powders, such as large particle size, wide size distribution and high degree of particle agglomeration. In this regard, it is desired to lower preparing temperature in order to get $BaTiO_3$ powder with fine and homogenous structures. Various chemistry based methods have been developed to prepare $BaTiO_3$ at low temperatures. Examples include chemical co-precipitation, sol-gel process, hydrothermal, molten salt, microemulsion and auto-combustion [174-177].

Single phase BT can be synthesized from oxide mixture of BaO and TiO_2 via a mechanical milling only under nitrogen environment [178] or vacuum [243]. The phase evolution of perovskite BT is similar to those of PT, PZT and PMN. Fig. 69 shows the XRD patterns of the mixture of BaO and TiO_2 milled for different time durations. BT is already formed after milling for 5 h. 10-h-milling increases the amount of BT phase, while 15-h-milling results in totally single phase BT. The resultant BT phase is at nanometer scale (20-30 nm), as shown in Fig. 70 [178]. Single phase BT can also be directly synthesized in vacuum, as reported by Welham [243]. The author used a vertical 316S stainless steel ball mill to grind the mixtures of alkaline earth metal oxides (Mg, Ca, Sr and Ba) and TiO_2 (rutile) in vacuum at room temperature.

However, high-energy mechanical milling can reduce the phase formation temperature of BT by altering the reaction process [179-182]. An example was shown in Ref [180]. 10-h-milling reduced the diffraction intensities of $BaCO_3$ and TiO_2, indicating a significant refinement the starting $BaCO_3$ and TiO_2 powders. The particle size of the milled powders estimated from the broadened diffraction peaks of $BaCO_3$ is about 35 nm, being in a good agreement with the SEM observation, as shown in Fig. 71 (where the grain size is obviously <50 nm). Thermal analysis result exhibits three endothermic peaks, at 665°C, 810°C and 995°C, as shown in the DTA curve of Fig. 72. The first two peaks are corresponding to weight losses, whereas no weight loss with respect to the last one is observed. The XRD patterns of the milled mixture annealed at temperature

from 600°C to 900°C are shown in Fig. 73. For the sample annealed at 600°C, no reaction was observed because all the diffraction peaks can be easily attributed to $BaCO_3$ and TiO_2. The sharpened diffraction peaks are due to the coarsened grains of $BaCO_3$ and TiO_2 as a result of calcination. After firing at 700°C, an intermediate phase with a composition Ba_2TiO_4 (JCPDS No. 38-1481) is detected. At the same time, TiO_2 and $BaTiO_3$ are also found at this temperature. Further increase in annealing temperature to 800°C, single phase $BaTiO_3$ is formed. This temperature is much lower than that required by conventional solid-state reaction process.

Combining the DTA/TGA curves and the XRD results of the milled mixture, the reaction consequence of the phase formation in the mixture as a result of the post thermal annealing can be described as following [180-181].

$$2BaCO_3 + TiO_2 = Ba_2TiO_4 + 2CO_2 \quad (2)$$

$$Ba_2TiO_4 + TiO_2 = 2BaTiO_3 \quad (3)$$

Eqs. (2) and (3) are corresponding to the endothermic peaks at 665°C and 810°C, respectively. The third peak in the DTA curve is still difficult to explain. DTA/TGA of the milled mixture was performed for two times to confirm the experimental reliability. The results obtained are almost the same. It means that the reaction path of $BaCO_3$ and TiO_2 to form BT was altered in the mixture treated by the high-energy ball milling process.

Fig. 74 shows the XRD patterns of the milled mixture calcined at high temperatures from 1000°C to 1150°C for 2 hours. The lattice constant of the cubic structured $BaTiO_3$ is calculated from the XRD patterns to be a=4.030(5) Å, which is in good agreement with the value reported in the literature (JCPDS No. 31-0174, a=4.031 Å). The cubic structure is remained after annealing at 1000°C. After firing at 1050°C, diffraction peak at $2\theta=45.5°$ becomes slightly wide, an indicative of split of the peak. This implies that $BaTiO_3$ is of tetragonal structure in the 1050°C-annealed sample. But it is still difficult to distinguish between (002) and (200) due to overlap of them. As the annealing temperature is further increased to 1150°C, split of diffraction peaks is obviously observed, meaning that tetragonal $BaTiO_3$ is formed at this temperature. Lattice parameters of $BaTiO_3$ of the 1150°C-annealed sample estimated from the XRD pattern are a=3.996(7) Å, c=4.037(6) Å and c/a=1.01 (IDD No. 5-626). The tetragonality of $BaTiO_3$ is related to the grain size of the samples as a result of thermal annealing.

The calcined samples were examined using SEM, from which the average grain sizes were estimated. Fig. 75 shows the average grain size as a function of annealing temperature. Almost no significant grain growth is observed at 1000°C and the grain size slightly increases at 1050°C. Sharp increase in grain size to about 3 μm is observed as the annealing temperature is increased from 1100°C to 1150°C.

The enhanced reaction of $BaCO_3$ and TiO_2 towards $BaTiO_3$, as a result of a high-energy milling process, using either ZrO_2 or agate milling media, has also been reported by other researchers [176, 177, 181, 182]. Similar results have been observed, which confirms the positive effect of high-energy treatment on the formation of $BaTiO_3$ from mixtures of $BaCO_3$ and TiO_2.

Recently, however, there was a report showing that perovskite BT can be directly synthesized from BaO and TiO_2 via mechanical milling in air [244]. Stojanovic *et al* [244] used ZrO_2 milling media (ZrO_2 vial of 500 cm^3 charged with ZrO_2 balls of a nominal diameter of ~10 mm) to mill TiO_2 (rutile) and BaO with a Fritsch

Pulverisette 5 planetary ball mill. The ball-to powder mass ratio was 20:1. The angular velocity of the supporting disc and vials was 33.2 rad s^{-1} (317 rpm) and 41.5 rad s^{-1} (396 rpm), respectively. The powders were milled for 0.5, 1, 2 and 4 h. Single phase perovskite BT powders with a crystalline size of 20-50 nm were synthesized after milling for only 4 h. Fully dense BT ceramics with a grain size of 0.5 to 1 μm were obtained by sintering pellets of the BT powders at 1330 ℃. The BT ceramics had a room temperature dielectric constant of 2500 at 100 kHz. Curie temperature (T_C) of the BT ceramics (135 ℃) was higher than that of the conventionally obtained BT ceramics (120 ℃-130 ℃), which was ascribed to the consequence of the high-energy activation, without a full understanding at this moment. As shown in Fig. 76, sharp phase transition from ferroelectric to paraelectric state was observed in such BT materials. The samples also had well-developed hysteresis loop, as illustrated in Fig. 77. This is contrast to the previous conclusion that BT phase cannot be derived from mixture of $BaCO_3$ and TiO_2 in air because $BaCO_3$ is stable against mechanical activations. If on uses BaO as the starting material, it finally becomes $BaCO_3$ due to the adsorption of CO_2 from air. Therefore, single phase BT cannot be directly synthesized via high-energy milling in air [178, 243]. No attempt was made by the authors to explain the formation mechanism of BT. Note that the processing parameters used in this study are different from those used by other researchers [178, 180], where the milling speeds are lower and the milling times are longer. These factors should be taken into account when further works are carried out to clarify this observation.

Strontium (Sr) is an element widely used to modify the electrical properties of BT. $SrTiO_3$ (ST) and BT can form solid solutions with perovskite structure in whole composition range ($Ba_{1-x}Sr_xTiO_3$ or BST). First, the addition of Sr reduces the Curie temperature of BT. It has been reported that the Curie temperature of BST ($Ba_{1-x}Sr_xTiO_3$) is almost linearly decreases with increasing concentration of Sr and the composition with a T_C close to room temperature is x=0.25-0.30. Second, BST has a diffused phase transition from ferroelectric to paraelectric state.

Fully dense and fine-grained BST ceramics have been prepared by sintering the nanosized BST powders ($Ba_{1-x}Sr_xTiO_3$ with x=0, 0.25, 0.50, 0.75 and 1), with a spark plasma sintering (SPS) method [245]. The starting materials are BaO_2, SrO and TiO_2 (anatase). The high-energy ball milling was conducted using a Fritsch Pulverisette 6 type planetary mill, with stainless steel vials and balls as milling media. Single phase BST nanosized powders were directly synthesized after milling for 72 h at 200 rpm. The lowest temperature at which fully dense BST ceramics can be produced is only 985 ℃, which is 300 ℃-400 ℃ lower than the sintering temperatures for SBT powders obtained by solid-state reaction or chemical synthesis. By controlling the SPS sintering conditions, the average grain size of the BST ceramics can be less than 200 nm. This provides an effective way to fabricate nanosized BST ceramics.

3.4. Aurivillius Ferroelectrics

Aurivillius type structure compounds have a general formula $[Bi_2O_2][A_{n-1}B_nO_{3n+1}]$, which are built up by *n* pseudo-perovskite $[A_{n-1}B_nO_{3n+1}]^{2-}$ layers alternating with $[Bi_2O_2]^{2+}$ layers. These materials have received great interest due to their high Curie temperatures and excellent piezoelectric properties. Various ferroelectric materials of Aurivillius family have been synthesized via high-energy mechanical milling process. Some of them can be produced directly from oxide mixtures, while others are crystallized from amorphous of oxide precursors created by high-energy activations.

3.4.1. $Bi_4Ti_3O_{12}$

Bismuth titanate ($Bi_4Ti_3O_{12}$, BiT) is the most famous Aurivillius type ferroelectric material with n=3 [183]. It is a good candidate for high-temperature piezoelectric applications, memory storage, and optical displays because of its high Curie temperature (675°C) and good electro-optical switching behavior [184-187]. Nano-sized BiT powders have been synthesized from oxide mixture via a high-energy planetary ball milling process [188, 190, 246, 247]. BiT ceramics with good dielectric and pyroelectric properties are obtained from the nano-sized BiT powders.

Fig. 78 shows the XRD patterns of the oxide mixture for BiT milled for different time durations [188]. The 3-h-milled mixture still consists of the starting oxides, with their particle sizes being reduced to 100-200 nm. Peaks of BiT begin to appear after milling for 9 hours. Single phase BiT is formed after milling for 15 h. This result is very similar to those observed for the lead-containing ferroelectrics. BiT ceramics can be obtained by sintering the 15-h-milled powder at 750°C, 850°C and 950°C for 1 h. The samples exhibit plate-like grains with average grain size increasing with sintering temperature. For the samples sintered at 750°C for 1 hour, a density of 7.7 g/cm^3 (the theoretic density of is 8.04 g/cm^3) is achieved, with an average grain size of about 3.6 μm. Almost fully dense BiT ceramics (7.91 g/cm^3) are obtained at 850°C. The average grain size of the samples increases to about 5.1 μm. The grain size of BiT increases to about 6.8 μm. But the sample's density shows a slight decrease after sintering at 950°C. The slight reduction in density results from the formation of plate-like grains. The sintering temperature of the mechanochemically synthesized BiT is lower than those required by the powders made by other methods [184-186], indicating that the nano-sized BiT powders synthesized by the high-energy ball milling process have better sinterability.

Fig. 79 shows the room temperature P-E loop curves of the BiT ceramics sintered at different temperatures [188]. The P-E loops of the ceramics have been well developed. The electrical properties, as well as the microstructural characteristics, of the sintered BiT ceramics are summarized in Table 9 [188]. The variations in the electrical properties of the BiT ceramics as a function of sintering temperature are related to the variation in microstructure and grain size of the samples. For example, the polarizations of the ceramics are associated with their plate-like structures. Due to its special structure, BiT single crystal is strongly anisotropic in all the ferroelectric properties, including saturated polarization (P_s), remanent polarization (P_r), and coercive field (E_c). The polarization direction of BiT is 4.5° off the base plane of its cell structure, thus giving rise to a much larger in-plane polarization (P_s=50 μC/cm^2) than c-axis polarization (P_s=4.5 μC/cm^2), and the E_c value for in-plane polarization is 50 kV/cm and the E_c value for c-orientation is less than 5 kV/cm [183, 184, 187]. For randomly oriented BiT ceramics or thin films, both P_r and E_c have intermediate values. When the sintering temperature increases from 850°C to 950°C, the BiT ceramics become more plate-like. As a result, the remanent polarization of the samples decreases as the sintering temperature is from 850°C to 950°C.

Ferroelectric materials with layered structures, such as BiT, are prone to develop anisotropic microstructure, especially at high temperatures, which is due to their special anisotropic lattice structures. It is well known for ceramic materials that the grain boundaries generally have higher internal energy than the grain interiors. During sintering at high temperatures, grain growth occurs to reduce the volume fraction of grain boundaries and thus the internal energy of the systems. There is always inhomogeneity in ceramic materials, where some grains are larger than others. Larger grains would grow at the expense of small ones via an Ostwald repening processing. Due to the anisotropy of grain boundary energy of layered structure ferroelectric materials,

their grain growth exhibits a high selectivity, i. e. some surface planes grow faster than others. Specifically for BiT, the (*00l*) crystal planes have lower surface energy than other planes [183-187]. Therefore, grains grow BiT in such a way that mass transport tends to "cover" the surface planes with higher surfacical energies. As a consequence, the (*00l*) crystal planes BiT would develop more fully than others during sintering and thus BiT grains are often characterized by plate-like morphologies [183-188].

The BiT ceramics synthesized via the high-energy milling process showed interesting pyroelectric properties. Fig. 80 shows the curves of pyroelectric coefficient as a function of measuring temperature for the BiT ceramics sintered at 850°C for 1 h [188]. The fresh-sintered sample shows a broadened peak at about 100 °C, which disappears when measured for the second time with a great reduction in the pyroelectric coefficient. The fresh-poled sample exhibits the most distinguished pyroelectric property with a maximum value at about 175°C, which diminishes when measured for the second run. The pyroelectric coefficient measured for the third time of the poled sample keeps almost unchanged, especially at the end of low temperature.

The current peaks of the as-sintered and poled BiT ceramics are attributed to thermally stimulated current, resulting from the defects and trapped charges produced during the preparation process of the ceramics [189]. These charges are not reversible, so the current peaks disappear when the samples are measured for the second time. The poled samples show a higher current and higher temperature at which the current peak occurs than as-sintered one because the poling aligned the dipolar orientations within the BiT ceramics. The almost unchanged pyroelectric characteristic of the poled BiT ceramics versus measurement cycles makes it a potential candidate for practical application of pyroelectric detectors.

Alternatively, Castro *et al* [190] reported the production of amorphous precursors of BiT via mechanochemical activation techniques, using two types of mills (vibrating and planetary mills). Crystalline BiT can be formed from the amorphous precursors at lower temperatures, as compared with conventional solid-state reaction process. They also compared the mechanochemical process with a wet coprecipitation route.

For example, amorphous powder was obtained from the mixture of $2Bi_2O_3{\cdot}3TiO_2$ after milling for 19 h, using a planetary mill. The amorphous powder was post annealed at different temperatures to find out the crystallization temperature of BiT. Fig. 81 shows the XRD patterns of the 19-h-planetary-milled mixture of $2Bi_2O_3{\cdot}3TiO_2$, calcined at different temperatures. The annealing parameters (temperature and time), with which BiT phase starts to form and single phase BiT is obtained, are listed in Table 10 [190]. It is found that the crystallization temperatures of the amorphous precursors, produced using the vibrating mill and the planetary mill, are 600 ℃ and 500 ℃, respectively. These temperatures are lower than that required by the conventional solid-state reaction process by 250-350 ℃ and are comparable with that observed in the coprecipitated precursors. The improved crystallization behavior of BiT from the amorphous precursors produced by the high-energy mechanochemical activations was attributed to the high internal energy (reactivity) of the milled powders caused by the accumulative defects generated during milling process [190].

The authors also found that planetary mill is more powerful than vibrating mill. For example, after milling for 72 h by a vibrating mill, the powder still contains the initial oxides as major phases. Complete amorphization requires prolonged milling duration of as long as 168 h. In contrast, for the planetary mill, amorphization can be finished after milling for only 19 h. This difference in milling efficiency between the vibrating and the planetary mill is attributed to the difference in the energy produced by the two mills. In the

vibrating mill (Fritsch Pulverizette 0), one ball of 5-cm diameter was used, whereas in the planetary mill (Fritsch Pulverizette 6), five balls of 1-cm diameter each were used. For the planetary mill, the milling speed was 200 rpm. 3 g mixtures were used in each experiment.

Nano-sized BiT powders were also synthesized from coprecipitated precursor via mechanochemical activation [191]. The precursor of BiT is coprecipitated from solution of $TiCl_4$ and $Bi(NO_3)_3$ $5H_2O$, using NH_3 as the precipitant. BiT phase is formed from the precursor after milling for 20 h. Similarly, the synthesized BiT powder has a better sinterability than that produced by the solid-state reaction process. BiT ceramics with a relative density of >95%, a dielectric constant of ~1260 at 1 MHz and a Curie temperature of 646 ℃, can be derived from the 20-h-milled precursor after sintering at 875 ℃ for 2 h.

Although BiT nanosized powders have been successfully synthesized via high-energy mechanochemcal activations, no attempt has been made to examine and explain the structural change in detail [188, 190, 246]. The structural variation of the system $2Bi_2O_3{\cdot}3TiO_2$, as a result of high-energy milling, was carefully studied by Zdujic *et al* in a recent article [247]. To have a better understanding of the effect of high-energy milling on the structural evolution, the authors also milled BiT powders synthesized via a reactive sintering method separately. Both the oxide mixture (Bi_2O_3 and TiO_2) and the BiT powder were milled using a Fritsch Pulverisette 5 type planetary ball mill. Stainless steel vials of 500 ml and hardened-steel balls of 13.4 mm in diameter were used as milling media. The ball-to-powder weight ratio was 20:1.

The authors used to two sets of milling experiments to check the effect of milling power. In the first set, the powders were milled up to 15 h initially at an angular velocity of the basic disc of 180 rpm and vials of 225 rpm. After that, the angular velocities of both basic disc and vials were increased to 317 rpm and 396 rpm, respectively. The samples were milled for extra time durations of 1, 3 and 5 h, after which additional 10 h milling was applied at basic disc and vial velocities of 180 rpm and 225 rpm (the initial speed). The second milling set conducted at the maximum speed (317 and 396 rpm) for 20 h, followed by an additional 10-h-milling at low speed (180 and 225 rpm).

It was found that the formation of BiT phase in the $2Bi_2O_3{\cdot}TiO_2$ mixture took place through the crystallization of an intermediate phase $Bi_2(CO_3)O_2$, which was not observed by other researchers [188, 190]. The formation of this intermediate compound was found after milling for 1 h. Further milling resulted in the formation of amorphous BiT phase. The mechanochemical reaction between $2Bi_2O_3$ and TiO_2 was triggered due to the creation of highly reactive fresh surfaces of particles and interfaces between the reactants. An additional high intensity milling induced a partial crystallization of the amorphous BiT phase. Prolonged milling for another 10 h at low speed led to amorphization of the crystalline BiT. The structural evolution of BiT powder as a result of the high-energy milling was similar, with only slight differences in degree and time of amorphization and crystallization transition. The kinetics of the reaction and phase transition were systematically studied by the authors. Interested readers are suggested to refer to the original article [247].

3.4.2. Other Aurivillius type ferroelectrics

Besides $Bi_4Ti_3O_{12}$, many other ferroelectric materials belonging to the Aurivillius family have also been produced using high-energy milling techniques. They include bismuth vanadate ($Bi_2VO_{5.5}$ or BiV) [192-196], bismuth molybdate tungstate ($Bi_2Mo_{1-x}W_xO_6$ or BiMW) [197], calcium and strontium bismuth titanate ($CaBi_4Ti_4O_{15}$ and $SrBi_4Ti_4O_{15}$ or CBiT and SBiT) [198, 199], bismuth titanate niobate (Bi_3TiNbO_9 or BiTN) [200, 201] and $(1-x)Bi_2SrNb_2O_9$-xBi_3TiNbO_9 [(1-x)SBN-xBTN] [202-207].

3.4.2.1. BiV

Shantha *et al* [192, 193] reported the synthesis of BiV from oxide precursors via a planetary ball mill (Fretsh, Pulverisette 6). The milled powders were characterized by XRD, DTA, EPR (electron paramagnetic resonance), TEM, SEM and dielectric and ferroelectric measurement.

It is found that an intermediate phase $BiVO_4$ is formed after milling for 4 h. The formation of the intermediate phase is complete after milling for 16 h. The desired phase BiV starts to form with further milling. 54-h-milling results in single phase BiV. It is interesting that the presence of the intermediate phase $BiVO_4$ cannot be avoided no matter what kind of starting materials are used, which is attributed to the fact that barrier for the nucleation of $BiVO_4$ is lower than that of BiV. Therefore, the formation of BiV from oxide precursors via the high-energy milling process experienced the following reaction sequences [192, 193].

$$Bi_2O_3 + 0.5V_2O_5 \rightarrow BiVO_4 + 0.5Bi_2O_3 \rightarrow Bi_2VO_{5.5} \qquad (4)$$

It is also noted that the as-synthesized BiV powder is of tetragonal structure, instead of the orthorhombic phase, with lattice parameters of a=b=3.9234Å, c=15.4925 Å, which is similar to those reported for the high temperature γ-phase of BiV. This was attributed to the small crystallite size (nanometer scale) and high elastic strain of the as-milled BiV powders. The nano-sized BiV powder is characterized by TEM, as shown in Fig. 82 [192], together with a selected-area electron diffraction (SAED) pattern. It is worth mentioning that the as-synthesized tetragonal BiV phase converted to orthorhombic phase by either a thermal annealing at a moderately high temperature (570 K) or a relatively low pressure (40 MPa) at room temperature.

The nano-sized BiV powders (n-BiV) synthesized by the high-energy milling process demonstrate improved sinterability as compared to those micro-sized powders (m-BiV) produced by the conventional solid state reaction process [192, 194]. The n-BiV leads to fine-grained ceramics (2 μm) with high density (>97%), while the m-BiV results in coarse-grained samples (12 μm) of low density. As listed in Table 11, the fine-grained ceramics possess much better dielectric, ferroelectric and pyroelectric properties than the coarse-grain ones.

Ricote *et al* [195] reported a different phase evolution in the mixture of Bi_2O_3-V_2O_5 system as a result of high-energy milling using a vibrating mill (Fritsch Pulverisette 0). Fig. 83 shows the XRD patterns of the $2Bi_2O_3$-V_2O_5 mixture milled for various time durations. The initial pattern contains diffraction peaks coming from bismuth and vanadium oxides. The peak intensities from bismuth oxide are much stronger than those from vanadium oxide. Neither BiV nor the intermediate phase $BiVO_4$ is detected by the XRD measurement with increasing milling durations. After milling for 72 h, the final product is essentially amorphous. The amorphous product, rather than nano-sized BiV powder, obtained by Ricote *et al*, has been attributed to the fact that the vibrating mill could be more energetic than the planetary ball mill used by Shantha *et al* [192, 193]. SEM examinations indicate that the particle size of the starting materials has been greatly reduced and the size distribution is very uniform. Crystallization of the amorphous powder is observed after post thermal annealing at temperature of as low as 385ºC, with the crystalline phase being identified to be γ-$Bi_2VO_{5.5}$ by XRD measurement [196]. The annealing only leads to crystallization, without the occurrence of grain growth. In fact, the particles of the annealed powder shrink because of the crystallization, as compared to the as-milled sample.

The presence of a majority of amorphous particles in the mechanically activated powder is also confirmed by TEM studies. However, as shown in Fig. 84, the TEM result indicates that some crystalline particles can also be observed, with particle size of 100-200 nm. Due to their small size and small quantities, the crystalline particles cannot be detected by XRD measurement. EDS analysis of the crystalline particles shows that some of them contain only Bi, corresponding to the starting oxide α-Bi_2O_3, others consist of Bi and V, with Bi:V ratios of 2:1 or 1:1, probably corresponding to $Bi_2VO_{5.5}$ or $BiVO_4$. This means that small amount of crystalline $Bi_2VO_{5.5}$ as minor phase has been formed during the high-energy mechanical activation. The presence of the intermediate $BiVO_4$ is in agreement with the observation reported by Shantha *et al* [192, 193]. The amorphous particles have Bi:V ratios ranging from 1:1 to 1.5:1, which are less than the desired composition of 2:1, implying the possible presence of $BiVO_4$ in the amorphous particles.

In terms of XRD measurement, a similar result is obtained in the system of Bi_2O_3-VO_2. The only difference is that Bi_2O_3-VO_2 requires longer time (168 h) to achieve amorphization, as compared to $2Bi_2O_3$-V_2O_5. TEM examination, combined with EDS analysis, shows that the amorphous particles are mostly Bi_2O_3. There are also crystalline particles in the amorphous Bi_2O_3-VO_2 system, which can be observed by TEM while not detectable by XRD due to their small size. The crystalline particles are found to be mainly VO_2, with very small portion of Bi_2O_3, which means that the high-energy mechanical activation produce amorphous Bi_2O_3 and refined VO_2. No amorphous particles corresponding to Bi_2VO_5, or $Bi_2VO_{5.5}$ and $BiVO_4$ are found, which has been attributed to the fact VO_2 particles are all crystallite. This in turn suggests that amorphization of all starting oxides is necessary to form a desired phase during the high-energy mechanical activation, at least, it is for this studied case. After annealing at 275℃ (determined by DTA [195]) in nitrogen environment, a fluorite-type f-Bi_2VO_5 phase is formed. The reaction towards the formation of f-Bi_2VO_5 is accompanied by the occurrence of particle coarsening, which is different from that observed in the $2Bi_2O_3$-V_2O_5 system where the particles shrink.

3.4.2.2. BiM and BiMW

Bi_2MoO_6 is another example of Aurivillius oxide with n=1 that has been synthesized via the high-energy milling technique, which is also reported by Ricote *et al* [195]. The phase evolution of the mixture of Bi_2O_3-MoO_3 as a result of high-energy milling is similar to that observed in the $2Bi_2O_3$-V_2O_5 system. 168-h-milling results in an amorphous product, evidenced by XRD measurement. The composition of the amorphous particles determined by EDS shows Bi:Mo ratios close to the 2:1 of the compound Bi_2MoO_6. Similarly, TEM study also finds the presence of crystalline particles, which are not detectable by XRD. The crystalline particles include the starting oxides Bi_2O_3, MoO_3 and the compound Bi_2MoO_6.

A new type of solid solution ferroelectric material with a formula of $Bi_2Mo_{1-x}W_xO_6$ that belongs to Aurivillius structural family has been synthesized by a mechanochemical synthesis [197]. Bi_2MoO_6 has four polymorphic phases: γ(F), γ(L), γ(I) and γ(H). The presence of these phases for Bi_2MoO_6 depends on material processing methods. Among the polymorphic phases, γ(L) are γ(I) low temperature ferroelectric and high temperature paraelectric states respectively. It is generally to improve the performances of ferroelectric and piezoelectric materials. However, doping of both bismuth and molybdenum positions in Bi_2MoO_6 with cations like antimony or arsenic often results in the stabilization of the unwanted nonferroelectric phase γ(H). Since Bi_2WO_6 is isostructural with the γ(L) of Bi_2MoO_6, it is therefore expected to substitute Mo with W to form solid solution $Bi_2Mo_{1-x}W_xO_6$ with improved properties. The conventional solid state reaction method is firstly used to determine the solid solution range of $Bi_2Mo_{1-x}W_xO_6$. It has been found the solid solution of $Bi_2Mo_{1-x}W_xO_6$ can be

obtained in the range of $0.5<x<1$. As a consequence, only $Bi_2Mo_{0.25}W_{0.75}O_6$ is used to study the synthesis via the high-energy mechanical activation. Fig. 85 shows the TEM image of the mixture of Bi_2O_3-$0.25MoO_3$-$0.75WO_3$ powders milled for 30 days using a vibrating ball mill [197], indicating that the high-energy mechanical activation produces amorphous particles, with particle sizes of 150-300 nm. EDS analysis indicates that the compositions of the amorphous particles are close to the nominal $Bi_2Mo_{0.25}W_{0.75}O_6$. Fig. 86 shows the XRD patterns of the amorphous $Bi_2Mo_{0.25}W_{0.75}O_6$ powders annealed at different temperatures. It is noted that crystallization of the amorphous particles takes place at a temperature of as low as 400 ℃ and the crystallization is almost complete at 425 ℃, which are much lower than required by the conventional solid state reaction process. $Bi_2Mo_{0.25}W_{0.75}O_6$ ceramics, with a relative density of 97-99%, a remanent polarization of 3.8 μC/cm$_2$ and a coercive field of 46 kV/cm, have been derived from the amorphous powder by sintering at 925 ℃ under axial pressure of 200 kg/cm.

3.4.2.3. CBiT and SBiT

Orthorhombic structured $ABi_4Ti_4O_{15}$ (A=Ca, Sr, Ba and Pb) belongs to the Aurivillius family with n=4 [198, 199]. SBiT has a T_C of ~540 ℃ and a very small temperature dependence of dielectric and piezoelectric properties over a wide temperature range, which is widely used as piezoelectric accelerators. Comparatively, the Curie temperature of CBiT is relatively high (~790 ℃), but it has poor piezoelectric property and large temperature dependence. Therefore, solid solutions consisting of CBiT and SBiT can be used to optimize the dielectric and piezoelectric properties for a given application [200]. During the preparation of CBiT and SBiT via the conventional ceramic process, the formation of the orthorhombic phase experiences a multiple reaction step at relatively high temperatures [201]. For example, in a mixture of $SrCO_3$, Bi_2O_3 and TiO_2 for SBiT, $Bi_{12}TiO_{20}$ and $Bi_4Ti_3O_{12}$ are formed at 500 ℃ and 600 ℃, respectively. SBiT starts to form at 700 ℃, while single phase is available at 1000 ℃. Single phase SBiT with average grain size of ~2 μm can also be obtained at 900ºC for 2 h. It is very difficult to sinter the micrometer sized SBiT powders into dense ceramics at low temperatures. High temperature sintering causes decomposition of SBiT due to the evaporation of bismuth component. To prevent the decomposition of SBiT, special carefulness is needed, which makes the process very complicated [201, 202]. This problem is, therefore, expected to be addressed by using nanosized CBiT or SBiT powders, synthesized by high-energy mechanochemical process.

Synthesis and characterization of CBiT and SBiT from oxide precursors via high-energy mechanical activation are reported by Wang *et al* [203, 204]. No intermediate phases such as $Bi_{12}TiO_{20}$ and $Bi_4Ti_3O_{12}$ are found in the milled powders. Single phase CBiT and SBiT with nano-meter size are directly synthesized from their oxide mixtures after milling for 30 h and 20 h, respectively. CBiT and SBiT ceramics with promising microstructures and electrical properties have been derived from the synthesized powders. Properties of the CBiT and SBiT ceramics are listed in Table 12, which are comparable with the reported values.

In contrast to the results reported by Wang *et al*, Castro *et al* [205] produced amorphous SBiT powders. They synthesized the amorphous SBiT powders using vibrating and planetary mill, as well as the conventional solid state reaction process as a comparison. Phase evolutions of the mixture of $SrCO_3$, Bi_2O_3 and TiO_2 for SBiT, as a result of the high-energy mechanical activation, using vibrating (VM) and planetary milling (PM), are listed Table 13 [205]. Phase compositions of the mixture milled via the vibrating milling and planetary milling for various time durations, identified from XRD patterns, are listed in Table 13. In the case of vibrating milling, significant reduction in XRD peak intensities is observed and amorphization takes place after 24-h-activation.

However, trance $SrCO_3$ can be detected until 72 h. Total amorphization is realized after milling 168 h. Compared to vibrating milling, the milling time needed to achieve amorphization by the planetary milling is only 12 h. The authors tried to obtain crystal phase of SBiT by prolonging the milling time to 108 h. However, no crystal phase is detected by the XRD measurement and the final product is still amorphous. Although the prolonged milling does not create crystal phase of the desired SBiT, it is beneficial to the crystallization of SBiT during the subsequent thermal annealing.

The phase evolutions of the milling amorphous powders, together with the sample derived from the solid-state reaction, are summarized in Table 14. It is clearly noted that the conventional solid-state reaction route requires high temperature to form the designed compound. For example, the mixture annealed at 800 ℃ for 12 h consists of Aurivillius phase $Bi_4Ti_3O_{12}$ and the perovskite $SrTiO_3$. Annealing at 1000 ℃ for 12 h still cannot eliminate the presence of $SrCO_3$. Single phase SBiT is obtained at a temperature of as high as 1050 ℃. In contrast to the solid-state reaction route, crystallization of SBiT phase from the amorphous precursors occurs at much lower temperatures. The VM and PM12 samples experience a similar phase evolution behavior during the thermal annealing, where a Sr-Bi-Ti-O fluorite-related phase is present before the formation of SBiT. For the VM sample, the fluorite phase is formed at 400 ℃ and the SBiT phase starts to form at 500 ℃. Although they coexist till 600 ℃, the fluorite is already a minor phase with a trace level after annealing at 600 ℃ for 5 h. Comparatively, the PM12 sample shows a slightly lower temperature at which the fluorite phase disappears and the SBiT crystallizes. Further enhancement in the crystallization of SBiT is observed in the prolonged milled precursor (PM108), with the single phase SBiT being available after 550 ℃. It is interesting to note that the fluorite phase observed in the VM and PM12 samples is not found in the PM108 sample. No explanation has been given for this observation. However, it is believed that the formation of the fluorite could be related to the homogeneity of the precursors. The prolonged milling increases the homogeneity of the system and thus reduces the formation temperature of SBiT.

3.4.2.4. BiTN and (1-x)SBiN-xBiTN

It is well known that Aurivillius compounds are difficult to prepare in form of dense ceramics due to the lack of mass diffusion (e. g. $SrTa_2O_9$ and Bi_3TiNbO_9) [206]. Therefore, to fabricate ceramics with high densification (say >98% of the theoretical density), it is necessary to use hot pressing. Due to their anisotropic crystalline structure and their slab-shape growing habit (the c-axis perpendicular to the largest face), Aurivillius type ceramics derived from hot pressing of powders generally have grains with their largest faces piled mainly perpendicular to the applied pressure during the sintering. This will lead to significant anisotropy in electric, ferroelectric and mechanical properties of the ceramics. The anisotropic characteristics of the Aurivillius ceramics are undesired for applications based on their ferroelectric properties, because the ferroelectric polarization lies on the (a, b) plane. It has been shown that this problem can be readily addressed by using amorphous precursors obtained from their corresponding oxide mixtures, via high-energy mechanochemical milling techniques [206-208]. Well sintered Aurivillius ceramics, with isotropic microstructures and significantly improved elastic, dielectric, ferroelectric and piezoelectric properties, have been fabricated from the corresponding amorphous precursors.

In the Aurivillius family ferroelectric materials, Bi_3NbTiO_9 (BiNT) is a very interesting example, with A and B sites in the perovskite layer being occupied by Bi^{3+} and Nb^{5+}/Ti^{4+}, respectively. It has a Curie temperature (T_C) of as high as 930 ℃. However, due to its extremely high Curie temperature, it is difficult to pole

BiNT ceramics using the poling technique widely used for the piezoelectric ceramics with relatively lower values of T_C. In this respect, components with lower T_C (e. g. $SrBi_2Nb_2O_9$ or SBiN) are needed to incorporate with BiNT, forming piezoelectric ceramics with moderate Curie temperatures. Solid solutions consisting of BiNT and SBiN with various compositions have also been prepared from their mechanochemically activated amorphous precursors [209-212]

Amorphous powders for $(1-x)SrBi_2Nb_2O_9$-xBi_3TiNbO_9 [(1-x)SBiN-xBiTN] with x from 0 to 1 were produced by high-energy ball milling process [206-210]. Similar to the Aurivillius family compounds mentioned above, amorphization in the oxide mixtures for SBiN-BiTN also need long time high-energy activation. Fig. 87 shows an example of the XRD pattern of the mixtures of Bi_2O_3, Nb_2O_5, $SrCO_3$ and TiO_2 milled for various time durations, using a vibrating mill (Fritsch Pulverisette 0). No significant variation in the XRD patterns can be observed after milling for 72 h. However, an essentially amorphous powder is obtained after milling for 168 h. 336-h-milling result in a complete amorphization. The milling time duration in this case is much longer than those required for the lead-containing ferroelectric materials.

The milling time duration has an obvious effect on the phase evolution of the oxide mixtures during the subsequent thermal annealing. For the unmilled oxide mixture, calcination temperature required to yield single phase BiTN is 1050 ℃. After milling for 72 h, BiTN is already the major phase at 800 ℃ and single phase can be obtained at 900 ℃. The annealing temperatures to form BiTN from the 168-h and 336-h-milled amorphous powders are 800 ℃ and 700 ℃, respectively, clearly indicating the increased reactivity of the powders as a result of the increased milling time duration.

The high-energy mechanical milling not only greatly reduces the phase formation temperature of the Aurivillius BiNT, but also has a direct influence on the microstructure and subsequent electrical properties of the BiNT ceramics. As stated above, due to the high calcinations, the BiNT powder derived from the conventional solid state reaction method possesses a lamellar morphology, which makes it difficult to produce dense ceramics since a high degree of packing of the grains is not easy by the normal cold-pressing. Therefore, the conventional sintering of the solid-state reacted powder leads to porous BiNT ceramics, which have low dielectric constant, low polarizability and poor piezoelectric response, due to the presence of porosity [206]. To produce dense ceramics, a hot-pressing sintering is required, where pressures and high temperatures are applied simultaneously. However, during a hot-pressing process, the lamellar grains tend to pile on top of each other with the c-axis parallel to the applied pressure, thus causing the hot-pressed ceramics with a texture structure which is of less polarization and mechanically anisotropic as well. Aurivillius ceramics fabricated in this way mostly have no piezoelectric properties. This problem has been addressed by using amorphous precursors. In contrast, if the amorphous precursor is used, dense ceramics can be readily obtained via a pressureless sintering. Due to the simultaneous occurrence of crystallization and sintering, the grain growth takes place in a constrained environment cause by the surrounding grains. The highly close packing of the grains results in lower porosity of the ceramics made from the amorphous precursor as compared to the solid-state reacted process. The reduced porosity of the ceramics, together with the higher homogeneity and isotropic character of the precursor, prevent the anisotropic grain growth. Owing to their lower porosities, such ceramics can be poled at higher electric field, thus leading to much better piezoelectric properties. These samples also demonstrate higher mechanical strength. A comparison of the microstructure of BiNT ceramics derived from the solid-state reacted powders and the high-energy ball milled amorphous precursors can be found in Fig. 88 [206].

It has been shown that a combination of hot-pressing and post thermal annealing can additionally improve the mechanical strength of the Aurivillius type ceramics while their electrical properties are not affected. An example is $(SBiN)_{0.35}(BiTN)_{0.65}$. The improved mechanical properties are ascribed to the reduction in porosity as a result of the recrystallization after hot-pressing. Detailed presentation can be referred to Ref. [211].

3.4.2.5. SBiT

Strontium bismuth tantalate ($SrBi_2Ta_2O_9$, SBT) was a promising candidate for non-volatile ferroelectric dynamic random access memory (DRAM), because of its high fatigue resistance and polarization retention up to 10^{12} switch cycles with Pt electrodes. SBT powders were synthesized from oxide precursors at temperatures of >1000 ℃ via the conventional ceramic processing. Ball milling seemingly produced a metastable, supersaturated solid solution of SrO and Ta_2O_5 in Bi_2O_3 matrix. Phase formation of SBT was not observed after milling for 50 h. But the milled precursor was able to form single phase SBT at 650 ℃, which is at least 300 ℃ lower than that required by the conventional ceramic processing [248].

3.5. $LiNbO_3$ and $NaNbO_3$

Lithium niobate ($LiNbO_3$ or LN) is a ferroelectric material with a variety of attractive properties, such as high pyroelectric, piezoelectric electro-optical and photo-elastic coefficients, large acoustic-optic figure-of-merit, and significant photorefractive effects. Conventional synthesis of LN requires high temperatures. Similar to lead containing ferroelectric materials, the high temperature required causes loss of Li element. The loss of stoichiometry by Li_2O evaporation, together with the formation of Nb-rich grain boundaries is seriously harmful to the planar coupling coefficient (K_p) and piezoelectric coefficient (d_{33}) of LN ceramics. Although ultrafine LN powders can be produced by wet-chemical routes, such as sol-gel, coprecipitation and Pechini's method, problems are similar to those encountered by lead containing ferroelectrics. Therefore, high-energy milling is an alternative way to synthesize LN powder. The work reported by de Figueiredo *et al* [213] is probably the only example. The starting materials used were Nb_2O_5 and Li_2CO_3 and milling duration varied from 2 to 42 h. A planetary mill (Fritsch Pulverisette 5) and stainless steel milling media were used [213]. XRD analysis indicates that LN crystalline phase is formed after milling for only 2 h and 42-h-milling results in LN as an essentially major phase with traces of amorphous phase and unreacted Nb_2O_5. The nano-sized crystalline LN synthesized by the high-energy ball milling process was also confirmed by IR (infrared spectroscope) and DTA. However, no information is available on the ferroelectric and piezoelectric properties of LN ceramics derived from the LN powder. Further work is necessary to clarify the quality of the mechanochemically synthesized LN powder.

Sodium niobate ($NaNbO_3$ or NN) is another example of niobate ferroelectric materials synthesized via mechanochemical milling, reported by Castro *et al* [214]. Unlike LN, NN crystalline phase cannot be produced from the mixture of Na_2CO_3 and Nb_2O_5, using a vibrating mill (Fritsch Pulverisette 0). After 7-day-milling, the phase composition of the milled powder consists of crystalline Nb_2O_5 and amorphous Na_2CO_3. No NN is detected by XRD measurement after milling even 30 days. However, due to the significant refinement of Nb_2O_5 and the amorphization of Na_2CO_3 as a result of the high-energy milling, NN phase formation derived from the milled powder becomes much easier via a subsequent thermal annealing. Perovskite phase NN starts to form at a temperature as low as 410 ℃ and single phase is obtained at 600 ℃ from the 30-day-milled mixture. In contrast, to synthesize NN phase from the unmilled mixture of Na_2CO_3 and Nb_2O_5 requires calcination of 750 ℃ for 12 h.

Combined with a hot-uniaxial-pressing, dense NN ceramics with promising piezoelectric properties has been fabricated from the 30-day-milled powder at ~200 kg/cm^2 and 1000 ℃ for 2 h.

3.6. Improved Sintering Properties of Ferroelectric Powders by Mechanical Milling

Besides the direct synthesis and assisted synthesis of ferroelectric powders, high-energy milling has also been used to treat commercial and lab-synthesized ferroelectric materials, such as PZT [250], BT [251] and BST [252]. It is found that high-energy milling is an effective way to modify the morphology, reduce the grain/particle sizes and thus enhance the densification behavior of ferroelectric powders, which will be discussed in this section, taking PZT as an example.

A commercially available PZT powder ($PbZr_{0.52}Ti_{0.48}O_3$, American Piezo Ceramics, Inc., Mckeyville, PA 17750) was milled for 10 h, 20 h and 40 h, using a Fritsch Pulverisette 5 planetary ball milling system in air at room temperature. A 250 ml tungsten carbide vial and 10 tungsten carbide balls with diameter of 20 mm were used as a milling medium. PZT powder without any additives was placed in the vial with the ball-to-powder weight ratio of 20:1. The milling speed was set at 200 rpm. The milling was stopped for 5 minutes for every 25 minutes to cool down the milling system.

The commercial powder consists of spherical particles with particle size ranging from 10 μm to 50 μm. Every particle contains a number of PZT grains of <1 μm in size, as shown in Fig. 89 (a). Not only the PZT spherical particles were destroyed by the high-energy mill, the PZT grains were also refined as well. Fig. 89 (b) shows that the PZT grain size is less than 100 nm, after milling for 10 h. Prolonged milling did not result in further reduction in PZT grain size. XRD results indicated that no the high-energy ball milling has no effect on the phase composition of the PZT powder. However, the diffraction peaks were all greatly reduced and broadened, which means that the PZT grains were significantly refined.

The consequence of the high-energy milling is the improved sinterability of the PZT powder. As shown in Fig. 90, the original PZT powder has only about 2% linear shrinkage before 1050°C, while almost full densification is achieved by the milled powder just above 900°C. At the same time, the maximum linear shrinkage rate occurs at about 810°C for the milled powder, whereas no such maximum is observed up to 1050°C. The sinterability of the commercial PZT powder is enhanced by about 250°C by high-energy ball milling process.

The enhanced sinterability of the milled PZT powder is also evidenced by the microstructure of the PZT ceramics. The cross-sectional SEM images of the PZT ceramics derived from the PZT powder before and after milling are shown in Fig. 91 and Fig. 92, respectively. The densities of the PZT ceramics as a function of sintering temperature are plotted in Fig. 93. The samples derived from the unmilled powder have many pores in microstructure as the sintering temperature was ≤1000°C, while full dense PZT ceramics are produced from the milled powders. The enhanced densification of the PZT powder as result of high-energy ball milling is readily attributed to the refined particles/grains. This is because refined particles/grains are more reactive. It is also observed that prolonged milling (20 h and 40 h) is not necessary.

The high-energy ball milling also led to PZT ceramics with different dielectric properties. The dielectric constant of the ceramic sample derived from the milled powder and sintered at 950°C is 1150, while the value for the sample from the unmilled powder and sintered at 1000°C in only 910 [250]. Moreover, the high dielectric loss tangent for the PZT ceramics made from the unmilled powder makes them distinctly different from the

samples from milled powder. Ferroelectric property is another indication to show the difference. As shown in Fig. 94 and Fig. 95, very lossy P-E hysteresis loops are demonstrated by the unmilled samples sintered at 950°C and 1000°C, while well-developed loop is observed for the milled sample sintered at 1000°C.

The lower dielectric constant and higher dielectric loss of the sample from unmilled powder are attributed to the porous structure. The presence of porosity usually decreases the dielectric constant of materials because the relative dielectric constant of pores/vacuum is unit. Water vapor absorbed and impurities trapped by open or interconnected pores are generally responsible for high dielectric loss tangent since they usually cause high conductive loss. This conduction is also responsible for the lossy P-E hysteresis loop of the unmilled samples.

The enhanced sinterability of commercial PZT powders is of interest to thick film and multilayer PZT devices. Thick films are usually fabricated by screen printing technique with PZT paste consists of PZT powders, sintering aids and organic binders. The sintering aids, which are glasses with low melting temperature, are used to lower the sintering temperature of thick films by forming liquid phase during sintering process. These glasses which compose of non-ferroelectric phases, however, are harmful to the performance of the final devices. As a result, PZT powders that can be sintered at low temperature (<1000°C) without any glasses additives will be attractive to thick films PZT based devices. Such powders are also important to multilayer PZT devices for at least two reasons. First consideration is cost reduction. Multilayer PZT devices are fabricated in such a way that the PZT layers and electrode layers are alternatively stacked via tape casting and screen printing and then co-fired (sintered) at high temperatures. If the sintering temperature is too high (>1000°C), only expensive metal like Pt, Au, Pd and Ag can be used as electrode layers, leading to higher cost devices. The reduction of device cost needs to use cheaper metals like Ni, Cr, and Cu as electrode materials. In this case, the sintering temperature of ferroelectric materials must be sufficiently low. Additionally, with the development of modern microelectronics, multilayer structured ferroelectric devices have to be able to work at low-driving voltage, to meet the requirement of miniaturization and hybridization. The pre-requisition is to reduce the thickness of the PZT active layer from hundreds (currently) to tens of micrometers. As the thickness of ferroelectric layer is reduced to 20 μm or less, the grain size of ferroelectric materials should not be larger than 1 μm. Otherwise, the electrode will be very easily shorting through the ferroelectric layers and hence the yield of the device will drop. Therefore, low temperature sintering is also desired to prevent grain growth.

4. Mechanisms

Having presented various examples of ferroelectric materials derived from the high-energy mechanical milling process, it is necessary to briefly describe the mechanisms that govern the phase formation process. Two categories of phase formation can be identified: activation-induced phase formation and activation-assisted phase formation, both of which are due to the introduction of high defect densities, shorter diffusion distances, more intimate contacts, creation of fresh/cleansed surface/interface, as a consequence of high-energy activations.

4.1. Direct Phase Formation Induced by Mechanochemical Activation

Phase formations by thermal activation in the conventional solid-state reaction and wet chemistry-based process are through various interfacial reactions or diffusions at boundaries between/among the precursor components, where one or more intermediate phases were usually formed preferentially prior to the formation of desired compounds. In contrast, the direct production of nano-sized ferroelectric phases activated by various

high-energy mechanochemical milling involves nucleation and subsequent growth of the ferroelectric crystallites, without the occurrence of interfacial reactions and diffusions.

However, high-energy mechanochemical reaction in the formation of designed ferroelectric compounds from oxide precursors is a complicated process. There are no well-established theoretic explanations available for these phenomena. The phase formation of ferroelectric materials via high-energy milling experiences two stages. At first stage, the milling is to greatly reduce the grain/particle sizes of the starting oxides. The fragmentation of the starting materials results in the formation of high defect densities, shorter diffusion distances, more intimate contacts of precursors. At the same time, fresh/cleansed surfaces/interfaces are created. All these factors contribute to the enhanced reactivity of the precursors. After a certain period of activation, depending on the materials involved and facilities used, reactions towards desired ferroelectric phases start to occur. Following this, nucleation and growth of the ferroelectric crystallites take place. Amorphization, an extreme defect state, is sometime also observed in the milled powders, such as those clearly identified by TEM examinations in Refs. [39, 41, 62, 123]. It has been suggested that localized heating at the points of collision could be an additional contribution to the reactions. This is because although the overall temperature of a milling system is normally lower than 100ºC, the "in-situ" impact temperature can be sufficiently high to activate the solid-state reactions [62, 215]. The reaction might also be facilitated by the very high localized-pressure created by the strong collision during the milling process [62, 216].

It is reported that, when a planetary mill is used to synthesize lead containing ferroelectric compounds, the final products are usually hard agglomerates, instead of loose powders [64-67, 94, 95, 217]. The hard layers are strongly stuck at the bottom of tungsten carbide vials. However, the agglomerates can be easily pulverable into powders. Fig. 96 shows a typical SEM image of surface profiles of a piece of $PbZr_{0.7}Ti_{0.3}O_3$ (PZT) derived from oxide mixture of PbO, ZrO_2 and TiO_2 after milling for 20 hours [217]. Areas of both dense (Fig. 96 (a)) and porous (Fig. 96 (b)) morphologies can be observed in the agglomerate. The dense area consists of rod-like particles with a length of 0.2-0.5 μm and a thickness of less than 100 nm. The appearance of such hard layers means that sintering of the formed PZT powder occurred during the milling process. This is a strong support to the suggestion of high localized-temperature caused by the high-energy ball milling [62, 215]. In this case, PZT phase is first formed incidentally at the bottom of the WC vial where the flying balls could collide at all time. After a certain number of nanosized PZT crystallites were formed, they would act as nuclei from which grain growth takes place. High local temperature and high pressure produced by the collision could cause the growth and densification of the PZT grains.

However, the local temperature is not higher than that required by the conventional solid-state reactions (>800 ℃). The formation of PZN can be an evidence to support this hypothesis. It is well known that single phase PZN crystals can be formed in excess PbO at high temperature [218], which has been successfully explained by the Ostward's step rule, as shown schematically in Fig. 97 [219]. The PZN single crystal is precipitated from supercooled melt under unequilibrium state. The variation in free energy in the molten system follows the thick line from high temperature. At a certain temperature, the supercooled melt becomes supersaturated so that crystallization will take place in the supercooled melt. According to the Ostwald's step rule, the phase precipitated from the supercooled melt is that with smaller free energy difference from the supercooled melt. Therefore, PZN perovskite, rather than pyrochlore, is precipitated from the molten state, as indicated by the arrow in the figure. Since the free energy of perovskite PZN is higher than that of pyrochlore,

the precipitated PZN is in a metastable state. As a result, the PZN crystals grown from excess PbO flux will be decompose to pyrochlore phase, a state of lower free energy. However, Fig. 84 also indicates, the free energy-temperature curves of perovskite and pyrochlore cross each other at a point. Below this point, perovskite has a lower free energy than pyrochlore. According to Jang *et al* [218], this temperature is ~600 ℃. Therefore, the synthesis of PZN via the high-energy mechanochemical process takes place at a temperature at least not high than 600 ℃. Otherwise, PZN cannot be obtained via a high-energy milling.

From the above discussion, it is concluded that a number of lead-containing ferroelectric powders can be directly synthesized from their oxide precursors as a result of high-energy mechanochemical process. It is the high-energy milling that effectively suppresses the grain growth of the synthesized phases. Therefore, ferroelectric powders produced in this way possess nanosized crystalline grains, thus having very high sinterabilities. Ferroelectric ceramics derived from the nanosized powders have demonstrated promising electrical, dielectric, ferroelectric, piezoelectric and pyroelectric properties. This group of nanosized powders mainly includes lead-containing ferroelectric [39-42, 62-70, 95, 96], antiferroelectric [111, 113] and relaxor ferroelectric materials [122-131, 155-158].

4.2. Assisted Phase Formation in the Activated Precursors

Some ferroelectric compounds cannot be directly synthesized via a high-energy milling process. However, the phase formation temperatures of these compounds can be significantly reduced as compared to that required by conventional solid-state reactions from unmilled precursors. This can be called activation-assisted phase formation. It is easy to understand the assisting effect of a high-energy milling in the formation of compounds, since the precursors are greatly refined by the mechanical activation. The refinement not only means the reduction in grain or particle size, but also means the creation of defects, dislocations, lattice distortions and microstrains in the precursor lattice. An extreme case of the refinement is amorphization of the precursors.

Amorphous metallic alloys or metallic glasses are solid alloys, with a liquid-like or non-crystalline atomic structures, have been extensively investigated [11, 12, 220]. Three critical requirements for the production of metallic glasses, via rapid solidification method, are (i) multiconmponent systems with three or more constituent elements, (ii) significantly different atomic size ratios typically with difference exceeding ~13% and (iii) negative heats of mixing among constituents. Recently, mechanochemical activation is found to be very effect way to produce amorphous metallic alloys. Metallic alloys can be even made in the systems with a positive heat of mixing. Mechanical alloying can produce amorphous alloys with wider composition ranges than those made by rapid solidification process. The mechanochemical activation has also been applied to amorphization of semiconductors, such as Se [221], Si [222] and SiC [223], oxides, such as mullite [224] and zoelite [225]. High-energy milling can induce not only accumulation of vast lattice and point defects but also chemical disordering of lattice. If the rate of dynamic recovery is less than the rate of defect production, the accumulation of the topological and chemical disorders will lead to a collapse of crystalline structure. This explanation is also applicable to the above mentioned amorphization behaviors of the Arivillius precursors. The amorphous precursors activated by the high-energy mechanical treatment have high degree of homogeneities and thus result in lower phase formation temperatures [190, 195, 205-211].

It has been shown that the Arivillius family ferroelectrics can be either directly synthesized from oxide mixtures by the high-energy milling [188, 191, 192,193, 203, 204] or from the mechanochemcallly derived amorphous precursors by post thermal annealing [109, 195-197, 205-211], suggesting that the crystallization and

the amorphization competed each other during the milling process. Which is favorable, crystallization or amorphization, depends on the processing parameters used, such as milling media, speed and ball-to-powder weight ratio. This dependency need further and systematic investigations.

5. Concluding Remarks

High-energy mechanochemical activation is a versatile and reliable technique to synthesize various ferroelectric materials. Many lead-containing ferroelectric compounds can be directly synthesized from oxide precursors via a high-energy ball milling. The synthesized powders have nanometer-scale grain size. Using these powders, ferroelectric ceramics can be fabricated at relatively lower sintering temperatures and possess better dielectric, ferroelectric, pyroelectric and piezoelectric properties. Successful examples include nanosized PZT powders which can be fully sintered at 900 ℃ and lead to PZT ceramics with promising electrical properties at 950 ℃, nanosized PT powders resulting in dense and crack-free PT ceramics that cannot be obtained from the conventionally synthesized powder, nanosized multicompoent antiferroelectric PNZST and PLZST powders that are not easily produced by wet chemistry processing routes such as precipitation and sol-gel, and nano-sized PMN powder that cannot be one-steply obtained via the conventional solid-state reaction process.

Ferroelectric ceramics, with promising microstructural and electrical properties, can be fabricated not only from the synthesized powders, but also from partially reacted or even unreacted mixtures activated by a high-energy ball milling. The fabrications of ferroelectric ceramics from the partially reacted or unreacted precursors are realized via reactive sintering.

Some interesting aspects have been observed in the synthesis of relaxor ferroelectrics via a high-energy mechanochemical process. PZN, a low-temperature stable and high-temperature unstable phase, that can never be synthesized via the conventional solid-state reaction process, has been directly obtained from the oxide mixture via a high-energy milling, evidencing that the mechanochemical process is a low-temperature process. Single phase PFN can be formed from oxide mixture via a mechanical activation, but high performance PFN ceramics can only be derived from the columbite precursor of PbO and $FeNbO_4$. Single phase PFW can be obtained neither from the oxide mixture of PbO, Fe_2O_3 and WO_3 nor from the mixture of PbO and Fe_2WO_6. It is only possible to produce PFW from the combination of $Pb_3Fe_2O_6$ and WO_3. PFW is also available when 0.4-mol-PFW was used as seeds. Mechanochemical activation can result in order-disorder in some relaxors.

Bismuth-containing ferroelectrics, belonging to the Arivillius family, have been either directly synthesized from oxide/carbonate precursors via the high-energy milling, or from the mechanochemically amorphized precursor powders through post thermal annealing, depending on the milling parameters used. The phase formation of amorphous powders occurs at relatively lower temperatures due to the great refinement and homogeneity of the precursors. The amorphous precursors can also be used to prepare ceramics without the requirement of the post thermal calcinations.

The mechanism that governs the phase formation of ferroelectric materials via high-energy mechanical milling process is still not clear. As a material system is subjected to a high-energy milling, the milling is first to refine the milled component, which results in fragmentation/refinement of the starting materials. The fragmentation/refinement leads to the formation of high defect densities, shorter diffusion distances, more intimate contacts of precursors, and the creation of fresh/cleansed surface/interface, all of which will increase the reactivity of the precursors. The occurrence of nucleation and growth of ferroelectric crystallines will be triggered after a sufficient activation. If crystalline phase is not formed, the accumulation of structural and

chemical disordering will lead to the collapse of the crystalline structure of the precursors, amorphization. Amorphous precursors have high reactivity due to their high degree of refinement and homogeneity.

Significant progress has been made in the preparation of ferroelectric materials using the high-energy mechanochemical process. Future studies should be focused on (i) systematically investigating the effect of various processing parameters on the ferroelectric phase formation, microstructure of the synthesized powders, as well as the microstructural and electrical properties of the final ceramic products, (ii) developing mechanisms/models to account for the phase evolution of ferroelectric compounds as a result of high-energy mechnaochemical milling.

Acknowledgements

The authors would like to thank Elsevier Science, Institute of Physics (IOP), World Scientific, AIP, American Ceramic Society (ACerS), American Ceramic Society (ACS), Royal Society of Chemistry (RCS), Kluwer, American Institute of Physics (AIP), Wiley Interscience and Springer for their permissions of reprinting diagrams and figures. One of the authors (L. B. K.) would like to sincerely thank Prof. T. Mohri for his constant encouragement in the preparation of the manuscript and the anonymous referee for his thorough reviewing of the manuscript and his constructive suggestions to revise the manuscript.

References:

[1] Haertling G H. Ferroelectric ceramics: history and technology. J Am Ceram Soc 1999; 82 (4): 797-818.

[2] Damjanovic D. Ferroelectric, dielectric and piezoelectric properties of ferroelectric thin films and ceramics, Rep Prog Phys 1998; 61: 1267-1324.

[3] Keizer K, Janssen E H, de Vries K J, Burggraaf A J. Influences of particle size and structure of ZrO_2 on microstructure development and dielectric constant of $Pb(Zr_{0.5}Ti_{0.5})O_3$. Mater Res Bull 1973; 8: 533-544.

[4] Yamamoto T. Optimum preparation methods for piezoelectric ceramics and their evaluation. Am Ceram Soc Bull 1992; 71 (6): 978-985.

[5] Arlt G. The influence of microstructure on the properties of ferroelectric ceramics. Ferroelectrics 1990; 104: 217-227.

[6] Czyrska-Filemonowicz A, Dubiel B. Mechanically alloyed, ferritic oxide dispersion strengthened alloys: structure and properties. J Mater Process Tech 1997; 64 (1-3): 53-64.

[7] Grahle P, Arzt E. Microstructural development in dispersion strengthened NiAl produced by mechanical alloying and secondary recrystallization. Acta Mater 1997; 45: 201-11.

[8] Welham N J, Willis P E, Kerr T. Mechanochemical formation of metal-ceramic composites. J Am Ceram Soc 2000; 83 (1): 33-40.

[9] Muñoz-Morris M A, Oca C G, Morris D G. Microstructure and room temperature strength of Fe-40Al containing nanocrystalline oxide particles. Acta Mater 2003; 51: 5187-5197.

[10] Ryu H J, Hong S H. Fabrication and properties of mechanically alloyed oxide-dispersed tungsten heavy alloys. Mater Sci Eng A 2003; 363: 179-84.

[11] Suryanarayana C. Mechanical alloying and milling. Prog Mater Sci 2001; 46: 1-184.

[12] Weeber A W, Bakker H. Amorphization by ball milling: a review. Phys. B 1988; 153: 93-135.

[13] Zhang D L. Processing of advanced materials using high-energy mechanical milling. Prog Mater Sci 2004; 49: 537-560.

[14] Harris J R, Wattis J A D, Wood J V. A comparison of different modes for mechanical alloying, Acta Mater 2001; 49: 3991-4003.

[15] Froes F H, Senkov O N, Baburaj E G. Synthesis of nanocrystalline materials-an overview. Mater Sci Eng A 2001; 301: 44-53.

[16] Koch C C. Intermetallic matrix composites prepared by mechanical alloying-a review. Mater Sci Eng A 1998; 244: 39-48.

[17] Hong L B, Fultz B. Two-phase coexistence in Fe-Ni alloys synthesized by ball milling. J Appl Phys 1996; 79 (8): 3946-3955.

[18] Suryanarayana C, Ivanov E, Boldyrev V V. The science and technology of mechanical alloying, Mater Sci Eng A 2001; 304-306: 151-158.

[19] Jiang J Z, Poulsen F W, Mørup S. Structure and thermal stability of nanostructured iron-doped zirconia prepared by high-energy ball milling. J Mater Res 1999; 14: 1343-1352

[20] Kong L B, Ma J, Zhu W, Tan O K. Phase formation and thermal stability of $(Zr_{1-x}Ti_x)O_2$ solid solution via a high-energy ball milling process. J Alloy Comp 2002; 335 (1-2): 290-296

[21] Janot R, Guérard D. One-step synthesis of maghemite nanometric powders by ball-milling. J. Alloy Comp 2002; 333: 302-307.

[22] Zdujić M, Jovalekić Ć, Karanović L, Mitrić M, Poleti D, Skala D. Mechanochemical treatment of α-Fe_2O_3 powder in air atmosphere. Mater Sci Eng A 1998; 245: 109-117.

[23] Simoneau M, L'Esperance G, Trudeau J L, Schulz R. Structural and magnetic characterization of granular $YBa_2Cu_3O_{7-\delta}$ nanocrystalline powders. J Mater Res 1994; 9:535-540.

[24] Jin Z Q, Tang W, Zhang J R, Lin H, Du Y W. Magnetic properties of isotropic $SrFe_{12}O_9$ fine particles prepared by mechanical alloying. J Magn Magn Mater 1998; 182: 231-237.

[25] Wang S, Ding J, Shi Y, Chen Y J. High coercivity in mechanically alloyed $BaFe_{10}Al_2O_{19}$. J Magn Magn Mater 2000; 219: 206-212.

[26] Fatemi D J, Harris V G, Browning V M, Kirkland J P. Processing and cation redistribution of MnZn ferrites via high-energy ball milling. J Appl Phys 1998; 83: 6767-6769.

[27] Shirane G, Hoshino S. On the phase transition in lead titanate, J Phys Soc Jpn 1951; 6: 265-270.

[28] Takeuchi H, Yamauchi H. Strain effects on surface acoustic wave velocities in modified $PbTiO_3$ ceramics. J Appl Phys 1981; 52 (10): 6147-6150.

[29] Chu S Y, Chen T Y. The influence of Cd doping on the surface acoustic wave properties of Sm-modified $PbTiO_3$ ceramics. J Eur Ceram Soc 2004; 24: 1993-1998.

[30] Yoo J H, Hong J I, Suh S. Effect of MnO_2 impurity on the modified $PbTiO_3$ system ceramics for power supply. Sens & Actuat 1999; 78: 168-171.

[31] Zeng Y, Xue W, Benedetti A, Fagherazzi G. Microstructure study of Sm, Mn-modified $PbTiO_3$ piezoelectric ceramics by XRD profile-fitting technique. J Mater Sci 1994; 29: 1045-1050.

[32] Ikegami S, Ueda I, Nagata T. Electromechanical properties of $PbTiO_3$ ceramics containing La and Mn. J Acoust Soc Am 1971; 50: 1060-1066.

[33] Kim S, Jun M, Hwang S. Preparation of undoped lead titanate ceramics via sol-gel processing, J Am Ceram Soc 1999; 82 (2): 289-296.

[34] Tartaj J, Moure C, Lascano L, Durán P. Sintering of dense ceramics bodies of pure lead titanate obtained by seeding-assisted chemical sol-gel, Mater Res Bull 2001; 36: 2301-2310.

[35] Udomporn A, Pengpat K, Ananta S. Highly dense lead titanate ceramics form refined processing. J Eur Ceram Soc 2004; 24: 185-188.

[36] Takeuchi T, Takahashi M, Ado K. Tamari N, Ichikawa K, Miyamoto S, Kawahara M, Tabuchi M, Kageyama H. Rapid preparation of lead titanate sputtering target using spark-plasma sintering. J Am Ceram Soc 2001; 84(11): 2521-2525.

[37] Takeuchi T, Tabuchi M, Kondoh I, Tamari N, Kegeyama H. Synthesis of dense lead titanate ceramics with submicrometer grains by spark plasma sintering. J Am Ceram Soc 2000: 83 (3): 541-544.

[38] Aning A O, Hong C, Desu S B. Novel synthesis of lead titanate by mechanical alloying. Mater Sci Forum 1995; 179-181: 207-214.

[39] Xue J M, Wan D M, Wang J. Mechanochemical synthesis of nanosized lead titanate powders form mixed oxides. Mater Lett 1999; 39: 364-369.

[40] Yu T, Shen Z X, Xue J M, Wang J. Nanocrystalline $PbTiO_3$ powders form an amorphous Pb-Ti-O precursor by mechanical activation. Mater Chem Phys 2002; 75: 216-219.

[41] Kong L B, Zhu W, Tan O K. Direct formation of nano-sized $PbTiO_3$ powders by high-energy ball milling, Ferroelectrics 1999; 230: 281-286.

[42] Kong L B, Zhu W, Tan O K. $PbTiO_3$ ceramics derived from high-energy ball milled nano-sized powders. J Mater Sci Lett 2000; 19: 1963-1966.

[43] Komatsubara S, Isobe T, Senna M. Effect of preliminary mechanical treatment on the microhomogenization during heating of hydrous gels as precursors for lead titanate. J Am Ceram Soc 1994; 77 (1): 278-282.

[44] Hamada K, Senna M. Mechanochemical effects on the properties of starting mixtures for $PbTiO_3$ ceramics by using a novel grinding equipment. J Mater Sci 1996; 31: 1725-1728.

[45] Durović D, Dostić E, Kiss S J, Zec S. Mechanochemical synthesis of $PbTiO_3$ from PbO and TiO_2. J Alloy Comp 1998; 279 (2): L1-L3.

[46] Leit E R, Santos L P S, Carreño, Longo E, Paskocimas C A, Varela J A, Lanciotti F, Campos Jr C E M, Pizani P S. Phololuminescence of nanostructured $PbTiO_3$ processed by high-energy mechanical milling. Appl Phys Lett 2001; 78 (15): 2148-2150.

[47] Kong L B *et al*. unpublished work.

[48] Löbmann P, Glaubitt W, Fricke J. Densification and crystallization of lead titnate aerogels. J Am Ceram Soc 1997; 80 (10): 2658-2666.

[49] Blum J B, Gurkovich S R. Sol-gel-derived $PbTiO_3$. J Mater Sci 1985; 20: 4479-4483.

[50] Sato S, Murakata T, Yanagi H, Miyasaka F. Hydrothermal synthesis of fine perovskite $PbTiO_3$ powder with a simple mode of size distribution. J Mater Sci 1994; 29: 5657-5663.

[51] Moon J, Li T, Randall C A, Adair J H. Low temperature synthesis of lead titanate by a hydrothermal method. J Mater Res 1997; 12 (1): 189-197.

[52] Peterson C R, Slamovich E B. Effect of processing parameters on the morphology of hydrothermally derived $PbTiO_3$ powders. J Am Ceram Soc 1999; 82(7): 1702-1710.

[53] Shrout T R, Papet P, Kim S, Lee G S. Conventionally prepared submicrometer lead-based perovskite powders by reactive calcinations. J Am Ceram Soc 1990; 73 (7): 1862-1867.

[54] Randall C A, Kim N, Kucera J P, Cao W, Shrout T R. Intrinsic and extrinsic size effects in fine-grained morphotropic-phase-boundary lead zirconate titanate ceramics. J Am Ceram Soc 1998; 81 (3): 677-688.

[55] Polli A D, Lange F F, Levi C G. Metastability of the fluorite, pyrochlore, and perovskite structures in the PbO-ZrO_2-TiO_2 system. J Am Ceram Soc 2000; 83 (4): 873-81.

[56] Wu A, Vilarinho P M, Miranda Salvado I M, Baptista J L. Sol-gel preparation of lead zirconate titanate powders and ceramics: effect of alkoxide stabilizers and lead precursors. J Am Ceram Soc 2000; 83 (6): 1379-1385.

[57] Muralidharan B G, Sengupta a, Rao G S, Agrawal D C. Powders of $Pb(Zr_xTi_{1-x})O_3$ by sol-gel coating of PbO. J Mater Sci 1995; 30: 3231-3237.

[58] Zimmermann-Chopin R, Auer S. Spray drying of sol-gel precursors for the manufacturing of PZT powders. J Sol-Gel Sci Technol 1994; 3: 101-107.

[59] Camargo E R, Frantti J, Kakihana M. Low-temperature chemical systhesis of lead zirconate titanate (PZT) powders free from halides and organics. J Mater Chem 2001; 11: 1875-1879.

[60] Chen D R, Jiao X L, Xu R R. Hydrothermal synthesis of $PbZr_xTi_{1-x}O_3$ (x=0.45-0.65) powders without using alkaline mineralizer. J Mater Sci Lett 1998; 17: 53-56.

[61] Arendt R H, Rosolowski J H, Szymaszek J W. Lead zirconate titanate ceramics from molten salt solvent synthesized powders. Mater Res Bull 1979; 14 (5): 703-709.

[62] Xue J M, Wan D M, Lee S E, Wang J. Mechanochemical synthesis of lead zirconate titanate form mixed oxides. J Am Ceram Soc 1999; 82 (7): 1687-1692.

[63] Lee S E, Xue J M, Wan D M, Wang J. Effects of mechanical activation on the sintering and dielectric properties of oxide-derived PZT. Acta Mater 1999; 47 (9): 2633-2639.

[64] Kong L B, Zhu W, Tan O K. Preparation and characterization of $Pb(Zr_{0.52}Ti_{0.48})O_3$ ceramics from high-energy ball milling powders. Mater Lett 2000; 42: 232-239.

[65] Kong L B, Ma J, Zhang T S, Zhu W, Tan O K. $Pb(Zr_xTi_{1-x})O_3$ ceramics via reactive sintering of partially reacted mixture produced by a high-energy ball milling process. J Mater Res 2001; 16 (6): 1636-1643.

[66] Kong L B, Ma J, Huang H T, Zhu W, Tan O K. Lead zirconate titanate ceramics derived from oxide mixture treated by a high-energy ball milling process. Mater Lett 2001; 50: 129-133.

[67] Kong L B, Ma J, Zhu W, Tan O K. Reaction sintering of partially reacted system for PZT ceramics via a high-energy ball milling. Scripta Mater 2001; 44: 345-350.

[68] Branković Z, Branković G, Jovalekić Č, Maniette Y, Cilense M, Varela J A. Mechanochemical synthesis of PZT powders. Mater Sci Eng A 2003; 345: 243-8.

[69] Parashar S K S, Choudhary R N P, Murty B S. Ferroelectric phase transition in $Pb_{0.92}Gd_{0.08}(Zr_{0.53}Ti_{0.47})_{0.98}O_3$ nanoceramic synthesized by high-energy ball milling, J Appl Phys 2003; 94 (9): 6091-6096.

[70] Xue J M, Wang J, Toh W. Synthesis of lead zirconate titanate form an amorphous precursor by mechanical activation. J Alloy Comp 2000; 308: 139-146.

[71] Kaneki S, Kong D, Murakami K. Effect of simultaneous addition of $BiFeO_3$ and $Ba(Cu_{0.5}W_{0.5})O_3$ on lowering of sintering temperature of $Pb(Zr,Ti)O_3$ ceramics. J Am Ceram Soc 1998; 81 (4) 1013-1018.

[72] Li J F, Wang S, Wakabayashi K, Esashi M, Watanabe R. Properties of modified lead zirconate titanate ceramics prepared at low temperature (800 ℃) by hot isostatic pressing. J Am Ceram Soc 2000; 83 (4) 955-957.

[73] Wittmer D E, Buchanan R C. Low-temperature densification of lead zirconate-titanate with vanadium pentoxide additive. J Am Ceram Soc 1981; 64 (8): 485-490.

[74] Li L, Zhang X, Chai J. Low temperature sintering of PZT ceramics. Ferroelectrics 1990; 101: 101-108.

[75] Cheng S Y, Fu S L, Wei C C, Ke G M. The properties of low-temperature fired piezoelectric ceramics. J Mater Sci 1986; 21: 572-576.

[76] Vaidhyanathan B, Singh A P, Agrawal D K, Shrout T R, Roy R, Ganguly S. Microwave effects in lead zirconium titanate synthesis: enhanced kinetics and changed mechanisms. J Am Ceram Soc 2001; 84 (6): 1197-1202.

[77] Jiang Q Y, Subbarao E C, Cross L E. Effect of composition and temperature on electric fatigue of La-doped lead zirconate titanate ceramics. J Appl Phys 1994; 75 (11): 7433-7443.

[78] Brown L M, Mazdiyasni K S. Cold-pressing and low-temperature sintering of alkoxy-derived PLZT. J Am Ceram Soc 1972; 55 (11): 541-544.

[79] Yao X, Chen Z, Cross L E. Polarization and depolarization behavior of hot pressed lead lanthanum zirconate titanate ceramics. J Appl Phys 1983; 54 (6): 3399-3403.

[80] Viehland D, Jang S J, Cross L E, Wuttig M. Internal strain relaxation and the glassy behavior of La-modified lead zirconate titanate relaxors. J Appl Phys 1991; 69 (9): 6595-602.

[81] Viehland D, Dai X H, Li J F, Xu Z. Effects of quenched disorder on La-modified lead zirconate titanate: long-and short-range ordered structurally incommensurate phases, and glassy polar clusters. J Appl Phys 1998; 84 (1): 458-471.

[82] Hammer M, Hoffmann M J. Sintering model for mixed-oxide-derived lead zirconate titanate ceramics. J Am Ceram Soc 1998; 81 (12): 3277-3284.

[83] Brodeur R P, Gachigi K W, Pruna P M, Shrout T R. Ultra-high strain ceramics with multiple field-induced phase transitions. J Am Ceram Soc 1994; 77 (11): 3042-3044.

[84] Yoshikawa Y, Tsuzuki K. Fabrication of transparent lead lanthanum zieconate titanate ceramics from fine powders by two-stage sintering. J Am Ceram Soc 1992; 75 (9): 2520-2528.

[85] Cerqueira M, Nasar R S, Leite E R, Longo E, Varela J A. Synthesis and characterization of PLZT(9/65/35) by the Pechini method and partial oxalate. Mater Lett 1998; 35: 166-171.

[86] Akbas M A, Lee W E. Synthesis and sintering of PLZT powder made by freeze/alcohol drying or gelation of citrate solutions. J Eur Ceram Soc 1995; 15: 57-63.

[87] Haertling G H, Land C E. Recent improvements in the optical and electrooptic properties of PLZT ceramics, Ferroelectrics. 1972; 3: 269-280.

[88] Snow G S. Improvements in atmosphere sintering of transparent PLZT ceramics. J Am Ceram Soc 1973; 56 (9): 479-480.

[89] James A D, Messer R M. The preparation of transparent PLZT ceramics from oxide powders by liquid-phase sintering. Trans J Br Ceram Soc 1972; 77: 152-158.

[90] Lin W K, Chang Y H. Behavior of PbO in the two-stage sintering of PLZT ceramics. Mater Sci Eng A 1994; 186: 177-183.

[91] Choi J J, Ryu J, Kim H E. Microstructural evolution of transparent PLZT ceramics sintered in air and oxygen atmospheres. J Am Ceram Soc 2001; 84 (7): 1465-1469.

[92] Abe Y, Kakegawa K, Ushijima H, Watanabe Y, Sasaki Y. Fabrication of optically transparent lead lanthanum zirconate titanate ((Pb,La)(Zr,Ti)O_3) ceramics by a three-stage-atmoshere-sintering technique. J Am Ceram Soc 2002; 85 (2): 473-475.

[93] Sun P, Xu C, Akiyama M, Watanabe T. Controlled oxygen partial pressure sintering of (Pb, La)(Zr, Ti)O_3 ceramics. J Am Ceram Soc 1999; 82 (6): 1447-1450.

[94] Kong L B, Ma J, Zhu W, Tan O K. Preparation and characterization of PLZT ceramics using high-energy ball milling. J Alloys Comp 2001; 322: 290-297.

[95] Kong L B, Ma J, Zhu W, Tan O K. Preparation and characterization of PLZT(8/65/35) ceramics via reaction sintering from ball milled powders. Mater Lett 2002; 52: 378-387

[96] (a) Kong L B, Ma J, Zhu W, Tan O K. Transparent PLZT8/65/35 ceramics from constituent oxides mechanically modified by high-energy ball milling. J Mater Sci Lett 2002; 21: 197-199. (b) Kong L B, Ma J, Zhu W, Tan O K. Preparation and characterization of translucent PLZT8/65/35 ceramics from nano-sized powders produced by a high-energy ball-milling process. Mater Res Bull 2001; 36: 1675-1685.

[97] Chen I W, Wang X H. Sintering dense nanocrystalline ceramics without final-stage grain growth. Nature 2000; 404: 168-171.

[98] Kong L B, Ma J, H Huang, Zhang R F. Effect of excess PbO on microstructure and electrical properties of PLZT7/60/40 ceramics derived from a high-energy ball milling process. J Alloys Comp 2002: 345: 238-245.

[99] Jaffe B, Cook W R, Jaffe H. Piezoelectric ceramics, Academic Press Limited, London, 1971.

[100] Li J F, Viehland D, Tani T, Lakeman C D E, Payne D A. Piezoelectric properties of sol-gel-derived ferroelectric and antiferroelectric thin layers. J Appl Phys 1994; 75 (1): 442-448.

[101] Tani T, Li J F, Viehland D, Payne D A. Antiferroelectric-ferroelectric switching and induced strains for sol-gel derived lead zirconate thin layers. J Appl Phys 1994; 75 (6): 3017-3023.

[102] Pokharel B P, Pandey D. Irreversibility of the antiferroelectric to ferroelectric phase transition in $(Pb_{0.90}Ba_{0.10})ZrO_3$ ceramics. J Appl Phys 1999; 86 (6): 3327-3332.

[103] Cross L E. Antiferroelectric-ferroelectric switching in simple 'kittle' antiferroelectrics. J Phys Soc Jpn 1967; 23: 77-82.

[104] Xu B, Moses P, Pai N G, Cross L E. Charge release of lanthanum-doped lead zirconate titanate antiferroelectric thin films, Appl Phys Lett 1998; 72 (5): 593-595.

[105] Berlincourt D, Krueger H H A, Jaffe B. Stability of phases in modified lead zirconate with variation in pressure, electric field, temperature and composition. J Phys Chem Solids 1964; 25: 659-674.

[106] Yang P, Payne D A. Thermal stability of fieled-forced and field-assisted antiferroelectric-ferroelectric phase transformation in $Pb(Zr,Sn,Ti)O_3$. J Appl Phys 1992; 71 (3): 1361-1367.

[107] Markowski K, Park S E, Yoshikawa shoko, Cross L E. Effect of compositional variation in the lead lanthanum zircornate stannate titanate system on electrical properties. J Am Ceram Soc 1996; 79 (12): 3297-3304.

[108] Oren E E, Taspinar E, Tas A C, Preparation of lead zirconate by homogeneous precipitation and calcinations. J Am Ceram Soc 1997; 80 (10): 2714-2716.

[109] Rao Y S, Sunandana C S. Low-temperature synthesis of lead zirconate. J Mater Sci Lett 1992; 11: 595-597.

[110] Ibrahim D M, Hennicke H W. Preparation of lead zirconate by a sol-gel method. Trans J Br Ceram Soc 1981; 80: 18-22.

[111] Kong L B, Ma J, Zhu W, Tan O K. Preparation and characterization of lead zirconate ceramics from high-energy ball milled powder. Mater Lett 2001; 49: 96-101.

[112] Xu Z, Viehland D, Payne D A. An incommensurate-commensurate phase transformation in antiferroelectric tin-modified lead zirconate titanate. J Mater Res 1995; 10 (2): 453-460.

[113] Kong L B, Ma J, Zhang T S, Zhu W, Tan O K. Preparation of antiferroelectric lead zirconate titanate stannate ceramics by high-energy ball milling process. J Mater Sci Mater Electron 2002; 13: 89-94.

[114] Cross L E. Relaxor ferroelectrics. Ferroelectrics 1987; 76: 241-267.

[115] Cross L E, Jang S J, Newnham R E. Large electrostrictive effects in relaxor ferroelectrics. Ferroelectrics 1980; 23: 187-192.

[116] Shrout T R, Halliyal A. Preparation of lead-based ferroelectric relaxors for capacitors. Am Ceram Soc Bull 1987; 66: 704-711.

[117] Swartz S L, Shrout T R, Schulze W A, Cross L E. Dielectric properties of lead magnesium niobate ceramics. J Am Ceram Soc 1984; 67: 311-315.

[118] Chaput F, Boilot J P, Lejeune M, Papiernik R, Hubert-Pfalzgraf L G., Low-temperature route to lead magnesium niobate. J Am Ceram Soc 1989; 72 (8): 1355-1357.

[119] Choy J H, Yoo J S, Kang S G, Hong S T, Kim D G. Ultrafine $Pb(Mg_{1/3}Nb_{2/3})O_3$ (PMN) powder synthesized from metal-citrate gel by thermal shock method. Mater Res Bull 1990; 25 (3): 283-291.

[120] Narenda Y, Messing G L. Kinetic analysis of combustion synthesis of lead magnesium niobate from metal carboxylate gels. J Am Ceram Soc 1997; 80 (4): 915-924.

[121] Han K R, Koo H J, Lim C S. Novel route to lead based ferroelectric compounds via tetragonal lead oxide intermediates. J Am Ceram Soc 2000; 83 (9): 2214-2218.

[122] Wang J, Xue J M, Wan D M, Ng W. Mechanochemically synthesized lead magnesium niobate. J Am Ceram Soc 1999; 82 (5): 1358-1360.

[123] Wang J, Xue J M, Wan D M, Ng W. Mechanochemical fabrication of single phase PMN of perovskite structure. Solid State Ionics 1999; 124: 271-279.

[124] Xue J M, Wang J, Rao T M. Synthesis of $Pb(Mg_{1/3}Nb_{2/3})O_3$ in excess lead oxide by mechanical activation. J Am Ceram Soc 2001; 84 (3) 660-662.

[125] Xue J M, Wang J, Ng W, Wang D. Activation-induced prychlore-to-perovskite conversion for a lead magnesium niobate precursor. J Am Ceram Soc 1999; 82 (8): 2282-2284.

[126] Wang J, Xue J M, Wan D M, Gan B K. Mechanically activating nucleation and growth of complex perovskites. J Solid State Chem 2000; 154: 321-328.

[127] Xue J M, Wan D M, Wang J. Functional ceramics of nanocrystallinity by mechanical activation. Solid State Ionics 2002; 151: 403-412.

[128] Kong L B, Ma J, Zhu W, Tan O K. Preparation of PMN powders and ceramics via a high-energy ball milling process. J Mater Sci Lett 2001; 20: 1241-1243.

[129] Kong L B, Ma J, Zhu W, Tan O K. Translucent PMN and PMN-PT ceramics from high-energy ball milling derived powders. Mater Res Bull 2002; 37: 23-32.

[130] Wang J, Wan D M, Xue J M, Ng W B. Synthesizing nanocryatalline $Pb(Zn_{1/3}Nb_{2/3})O_3$ powders from mixed oxides. J Am Ceram Soc 1999; 82 (2): 477-479.

[131] Wang J, Xue J M, Wan D M. How different is mechanical activation from thermal activation? A case study with PZN and PZN-based relaxors. Solid State Ionics 2000; 127: 169-175.

[132] Jenhi M, Elghadraoui E H, Bali I, Elaatmani M, Rafiq M. Reaction mechanism in the formation of perovskite $Pb(Fe_{1/2}Nb_{1/2})O_3$ by calcining of mixed oxide (CMO). Eur J Solid State Inorg Chem 1998; 35: 221-230.

[133] Chiu C C, Li C C, Desu S B. Molten salt synthesis of a complex perovskite $Pb(Fe_{1/2}Nb_{1/2})O_3$. J Am Ceram Soc 1991; 74 (1): 38-41.

[134] Mitoseriu L, Marré D, Siri A S, Nanni P. Magnetic properties of $PbFe_{2/3}W_{1/3}O_3$-$PbTiO_3$ solid solutions. Appl Phys Lett 2003; 83 (26): 5509-5511.

[135] Zhou L, Vilarinho P M, Baptista J L. Synthesis and characterization of lead iron tungstate ceramics obtained by two preparation methods. Mater Res Bull. 1994; 29 (11): 1193-1201.

[136] Lu C H, Shinozaki K, Mitzutani N. Formation process and microstructural evolution of sol-gel-derived lead iron tungstate ceramics. J Am Ceram Soc 1992; 75: 1003-1006.

[137] Gao X S, Xue J M, Wang J, Yu T, Shen Z X. Sequential combination of constituent oxides in the synthesis of $Pb(Fe_{1/2}Nb_{1/2})O_3$ by mechanical activation. J Am Ceram Soc 2002; 85 (3): 565-572.

[138] Ang S K, Wang J, Wang D M, Xue J M, Li L T. Mechanical activation-assisted synthesis of $Pb(Fe_{2/3}W_{1/3})O_3$. J Am Ceram Soc 2000; 83 (7): 1575-1580.

[139] Ang S K, Wang J, Xue J M. Seeding effect in the formation of $Pb(Fe_{2/3}W_{1/3})O_3$ via mechanical activation of mixed oxides. Solid State Ionics 2000; 132: 55-61.

[140] Ang S K, Xue J M, Wang J. $Pb(Fe_{2/3}W_{1/3})O_3$ by mechanical activation of coprecipitated $Pb_3Fe_2O_6$ and WO_3. J Alloys Comp 2002; 343: 156-163.

[141] Chu F, Reaney I M, Setter N. Spontaneous (zero-field) relaxor-to-ferroelectric-phase transition in disordered $Pb(Sc_{1/2}Nb_{1/2})O_3$. J Appl Phys 1995; 77 (4): 1671-1676.

[142] Park Y, Knowles K M, Cho K. Particle-size effect on the ferroelectric phase transition in $Pb(Sc_{1/2}Nb_{1/2})O_3$ ceramics. J Appl Phys 1998; 83 (11): 5702-5708.

[143] Lim J, Xue J M, Wang J. Ferroelectric lead scandium tantalate from mechanical activation of mixed oxides. Mater Chem Phys 2002; 75: 157-160.

[144] Kelly J, Leonard M, Tantigate C, Safari A. Effect of composition on the electromechanical properties of $(1-x)Pb(Mg_{1/3}Nb_{2/3})O_3$-$xPbTiO_3$ ceramics. J Am Ceram Soc 1997; 80 (4): 957-964.

[145] Guha J P. Effect of compositional modifications on microstructure development and dielectric properties of $Pb(Mg_{1/3}Nb_{2/3})O_3$-$PbTiO_3$ ceramics. J Eur Ceram Soc 2003; 23: 133-139.

[146] Suh D H, Lee K H, Kim N K. Phase development and dielectric/ferroelectric responses in the PMN-PT system. J Eur Ceram Soc 2002; 22: 219-223.

[147] Wang J, Wan D M, Xue J M, Ng W B. Mechanochemical synthesis of $0.9Pb(Mg_{1/3}Nb_{2/3})O_3$-$0.1PbTiO_3$ from mixed oxides. Adv Mater 1999; 11 (3): 210-213.

[148] Baek J G, Isobe T, Senna M. Synthesis of pyrochlore-free $0.9Pb(Mg_{1/3}Nb_{2/3})O_3$-$0.1PbTiO_3$ ceramics via a soft mechanochemical route. J Am Ceram Soc 1997; 80 (4): 9739-81.

[149] Kong L B, Ma J, Zhu W, Tan O K. Rapid formation of lead magnesium niobate-based ferroelectric ceramics via a high-energy ball milling process. Mater Res Bull 2002; 37: 459-465.

[150] Alguerό M, Alemany C, Jiménez B, Holc J, Kosec M, Pardo L. Piezoelectric PMN-PT ceramics from mechanochemically activated precursors. J Eur Ceram Soc 2004; 24: 937-940.

[151] Kuwata J, Uchino K, Nomura S. Phase relations in the $Pb(Zn_{1/3}Nb_{2/3})O_3$-$PbTiO_3$ system. Ferroelectrics 1981; 37: 579-582.

[152] Halliyal A, Kumar U, Newnham R E, Cross L E. Stabilizaion of the perovskite phase and dielectric properties of ceramics in the $Pb(Zn_{1/3}Nb_{2/3})O_3$-$BaTiO_3$ system. Am Ceram Soc Bull 1987; 66: 671-676.

[153] Belsick J R, Halliyal A, Kumar U, Newnham R E. Phase relations and dielectric properties of ceramics in the system $Pb(Zn_{1/3}Nb_{2/3})O_3$-$SrTiO_3$-$PbTiO_3$. Am Ceram Soc Bull 1987; 66: 664-667.

[154] M Ozgul, Tekemura K, Trolier-Mckinstry S, Randall C A. Polarization fatigue in $Pb(Zn_{1/3}Nb_{2/3})O_3$-$PbTiO_3$ ferroelectric single crystal. J Appl Phys 2001; 89 (9): 5100-5106.

[155] Kong L B, Ma J, Huang H, Zhang R F. (1-x)PZN-xBT ceramics derived from mechanochemically synthesized powders. Mater Res Bull 2002; 37: 1085-1092.

[156] Kong L B, Ma J, Huang H, Zhang R F. Lead zinc niobate (PZN)-barium titanate (BT) ceramics from mechanochemically synthesized powders. Mater Res Bull 2002; 37: 2491-2498.

[157] Tan Y L, Xue J M, Wang J. Stablization of perovskite phase and dielectric properties of 0.95PZN-0.05BT derived from mechanical activation. J Alloys Comp 2000; 297: 92-98.

[158] Xue J M, Tan Y L, Wan D M, Wang J. Synthesizing 0.9PZN-0.1BT by mechanically activating mixed oxides. Solid State Ionics 1999; 120: 183-188.

[159] Van Werde K, Vanhoyland G, Nelis D, Mondelaers D, Van Bael M K, Mullens J, Van Pouche L C. Phase formation of ferroelectric perovskite $0.75Pb(Zn_{1/3}Nb_{2/3})O_3$-$0.25BaTiO_3$ prepared by aqueous solution-gel chemistry. J Mater Chem 2001; 11: 1192-1197.

[160] Shinohara S, Baek J G, Isobe T, Senna Mamoru. Synthesis of phase-pure $Pb(Zn_xMg_{1-x})_{1/3}Nb_{2/3}O_3$ up to x=0.7 from a single mixture via a soft-mechanochemical route. J Am Ceram Soc 2000; 83 (12): 3208-3210.

[161] Ang S K, Wang J, Xue J M. Phase stability and dielectric properties of (1-x)PFW+xPZN derived from mechanical activation. Solid State Ionics 2000; 127: 285-293.

[162] Senda T, Bradt R C. Grain growth in sintered ZnO and ZnO-Bi_2O_3 ceramics. J Am Ceram Soc 1990; 73 (1): 106-114.

[163] Jang H M, Lee K, Lee M. Stabilization of perovskite phase and dielectric properties of $Pb(Zn,Mg)_{1/3}Nb_{2/3}O_3$-$PbTiO_3$ ceramics prepared by excess constituent oxides. J Mater Res 1994; 9 (10): 2634-2644.

[164] Escure P, Lattard E, Lejeune M, Baumard J F. Stability of the perovskite phase in PZN-PMN-PT ceramics. J Mater Sci 1996; 31: 3937-3943.

[165] Wan D M, Xue J M, Wang J. Synthesis of single phase $0.9Pb[(Zn_{0.6}Mg_{0.4})_{1/3}Nb_{2/3}O_3]$-$0.1PbTiO_3$ by mechanically activating mixed oxides. Acta Mater 1999; 47 (7): 2283-2291.

[166] Wan D M, Xue J M, Wang J. Nanocrystalline 0.54PZN-0.36PMN-0.1PT of perovskite structure by mechanical activation. Mater Sci Eng A 2000; 286; 96-100.

[167] Wan D M, Xue J M, Wang J. Mechanochemical synthesis of $0.9[0.6Pb(Zn_{1/3}Nb_{2/3})O_3$-$0.4Pb(Mg_{1/3}Nb_{2/3})O_3]$-$0.1PbTiO_3$. J Am Ceram Soc 2000; 83 (1): 53-59.

[168] Ang S K, Wang J, Xue J M. Mechanical activation and dielectric properties of 0.48PFN-0.36PFW-0.16PZN from mixed oxides. J Alloys Comp 2000; 311: 181-187.

[169] (a) Gao X S, Xue J M, Wang J, Yu T, Shen Z X. B-site disording in $Pb(Sc_{1/2}Ta_{1/2})O_3$ by mechanical activation. Appl Phys Lett 2003; 82 (26): 4773-5. (b) Gao X S, Xue J M, Wang J. The B-site order-disorder transformation in $Pb(Sc_{1/2}Ta_{1/2})O_3$ triggered by mechanical activation. J Mater Sci 2004; 39: 5267-5270.

[170] Gao X S, Xue J M, Yu T, Shen Z X, Wang J. Mechanical activation-induced B site order-disorder transition in perovskite $Pb(Mg_{1/3}Nb_{2/3})O_3$-$Pb(Mg_{1/2}W_{1/2})O_3$. Mater Chem Phys 2002; 75: 211-215.

[171] Gao X S, Xue J M, Yu T, Shen Z X, Wang J. B-site order-disorder transition in $Pb(Mg_{1/3}Nb_{2/3})O_3$-$Pb(Mg_{1/2}W_{1/2})O_3$ triggered by mechanical activation. J Am Ceram Soc 2002; 85 (4): 833-838.

[172] Alrt G, Hennings D, de With G. Dielectric properties of fine-grained barium titanate ceramics. J Appl Phys 1985; 58 (4): 1619-1625.

[173] Maurice A K, Buchanan R C. Preparation and stoichiometry effects on microstructure and properties of high-purity $BaTiO_3$. Ferroelectrics 1987; 74: 61-75.

[174] Bergström L, Shinozaki K, Tomiyama H, Mizutani N. Colloidal processing of a very fine $BaTiO_3$ powder-effect of particle interactions on the suspension properties, consolidation, and sintering behavior. J Am Ceram Soc 1997; 80 (2): 291-300.

[175] Clark I J, Takeuchi T, Ohtori N, Sinclair D C. Hydrothermal synthesis and characterization of $BaTiO_3$ fine powder: precursors, polymorphism and properties. J Mater Chem 1999; 9: 83-91.

[176] Brzozowski E, Castro M S. Synthesis of barium titanate improved by modifications in the kinetics of the solid state reaction. J Eur Ceram Soc 2000; 20: 2347-2351.

[177] Brzozowski E, Castro M S. Lowering the synthesis temperature of high-purity $BaTiO_3$ powders by modification in the processing conditions. Thermochimica Acta 2003; 389: 123-129.

[178] Xue J M, Wang J, Wang D M. Nanosized barium titnate powder by mechanical activation. J Am Ceram Soc 2000; 83 (1) 232-234.

[179] Abe O, Suzuki Y. Mechanochemically assisted preparation of $BaTiO_3$ powder. Mater Sci Forum 1996; 225: 563-568.

[180] Kong L B, Ma J, Huang H, Zhang R F, Que W X. Barium titanate derived from mechanochemically activated powders. J Alloys Comp 2002; 337: 226-230.

[181] Berbenni V, Marini A, Bruni G. Effect of mechanical milling on solid state formation of $BaTiO_3$ from $BaCO_3$-TiO_2 (rutile) mixtures. Thermochimica Acta 2001; 374: 151-158.

[182] van Hal H A M, Groen W A, Maassen S, Keur WC. Mechanochemical synthesis of $BaTiO_3$, $Bi_{0.5}Na_{0.5}TiO_3$ and $Ba_2NaNb_5O_{15}$ dielectric ceramics. J Eur Ceram Soc 2001; 21: 1689-1692.

[183] Dorrian J F, Newnham R E, Smith K K. Crystal structure of $Bi_4Ti_3O_{12}$. Ferroelectrics 1971; 3: 17-27.

[184] Cummings S E, Cross L E. Electrical and optical properties of ferroelectric $Bi_4Ti_3O_{12}$ single crystals. J Appl Phys 1968; 39 (5): 2268-2274.

[185] Shulman H S, Testorf M, Damjanovic D, Setter N. Microstructure, electrical conductivity and piezoelectric properties of bismuth titanate. J Am Ceram Soc 1996; 79 (12): 3214-3218.

[186] Jiang A Q, Li H G, Zhang L D. Dielectric study in nanocrystalline prepared by chemical doprecipitation. J Appl Phys 1998; 83 (9): 4878-83.

[187] Du X, Chen I W. Ferroelectric thin films of bismuth-containing layered perovskites: part I, $Bi_4Ti_3O_{12}$. J Am Ceram Soc 1998; 81 (12): 3253-59.

[188] Kong L B, Ma J, Zhu W, Tan O K. Preparation of $Bi_4Ti_3O_{12}$ ceramics via a high-energy ball milling process. Mater Lett 2001; 51: 108-114.

[189] Shaw C P, Gupta S, Stringfellow S B, Navarro A, Alcock J R, Whatmore R W. Pyroelectric properties of Mn-doped lead zirconate-lead titanate-lead magnesium niobate ceramics. J Eur Ceram Soc 2002; 22: 2123-2132.

[190] Lisoni J G, Millán P, Vila E, Martín de Vidales J L, Hoffmann T, Castro A. Synthesis of ferroelectric $Bi_4Ti_3O_{12}$ by alternative routes: wet no-coprecipitation chemistry and mechanochemical activation. Chem Mater 2001; 13: 2084-2091.

[191] Ng S H, Xue J M, Wang J. Bismuth titanate from mechanical activation of a chemically coprecipitated precursor. J Am Ceram Soc 2002; 85 (11): 2660-2665.

[192] Shantha K, Varma K B R. Preparation and characterization of nanocrystalline powders of bismuth vanadate. Mater Sci Eng B 1999; 56: 66-75.

[193] Shantha K, Subbanna G N, Varma K B R. Mechanically activated synthesis of nanocrystalline powders of ferroelectric bismuth vanadate. J Solid State Chem 1999; 142: 41-47.

[194] Shantha K, Varma K B R. Characterization of fine-grained bismuth vanadate ceramics obtained using nanosized powders. J Am Ceram Soc 2000; 83 (5): 1122-1128.

[195] Ricote J, Pardo L, Castro A, Millán P. Study of the process of mechanochemical activation to obtain Aurivillius oxides with n=1. J Solid State Chem 2001; 160: 54-61.

[196] Castro A, Millán P, Ricote J, Pardo L. Room temperature stabilization of γ-$Bi_2VO_{5.5}$ and synthesis of the new fluorite phase f-Bi_2VO_5 by a mechanochemical activation. J Mater Chem 2000; 10: 767-771.

[197] Castro A, Béguié P, Jiménez B, Ricote J, Jiménez R, Galy J. New $Bi_2Mo_{1-x}W_xO_6$ solid solution: mechanosynthesis, structural study, and ferroelectric properties of the x=0.75 member. Chem Mater 2003; 15: 3395-3401.

[198] Zhao M L, Wang C L, Zhong W L, Zhang P L, Wang J F, Chen H C. Dielectric and pyroelectric properties of $SrBi_4Ti_4O_{15}$-based ceramics for high-temperature applications. Mater Sci Eng B 2003; 99: 143-146.

[199] Zhu J, Mao X Y, Chen X B. Properties of vadadium-doped $SrBi_4Ti_4O_{15}$ ferroelectric ceramics. Solid State Comm 2004; 129: 707-710.

[200] Zheng L Y, Li G R, Zhang W H, Chen D R, Yin Q R. The structure and piezoelectric properties of $(Ca_{1-x}Sr_x)Bi_4Ti_4O_{15}$ ceramics. Mater Sci Eng B 2003; 99: 363-366.

[201] Lu C H, Wu C H. Preparation, sintering, and ferroelectric properties of layer-structured strontium bismuth titanatium oxide ceramics. J Eur Ceram Soc 2002; 22: 707-714.

[202] Gelfuso M V, Thomazini D, Eiras J A. Synthesis and structural, ferroelectric, and piezoelectric properties of $SrBi_4Ti_4O_{15}$ ceramics. J Am Ceram Soc 1999; 82: 2368-2372.

[203] Sim M H, Xue J M, Wang J. Layer structured calcium bismuth titanate by mechanical activation. Matter Lett 2004; 58: 2032-2036.

[204] Ng S H, Xue J M, Wang J. High-temperature piezoelectric strontium bismuth titanate from mechanical activation of mixed oxides. Mater Chem Phys 2002; 75: 131-135.

[205] Ferrer P, Iglesias J E, Castro A. Synthesis of the Aurivillius phase $SrBi_4Ti_4O_{15}$ by a mechanochemical activation route. Chem Mater 2004; 16: 1323-1329.

[206] Castro A, Millán P, Pardo L, Jiménez B. Synthesis and sintering improvement of Aurivillius type structure ferroelectric ceramics by mechanochemical activation. J Mater Chem 1999; 9: 1313-1317.

[207] Ricote J, Pardo L, Moure A, Castro A, Millán P, Chateigner D. Microcharacterization of grain-oriented ceramics based on Bi_3TiNbO_9 from mechanochemically activated precursors. J Eur Ceram Soc 2001; 21: 1403-1407.

[208] Moure A, Pardo L, Alemany C, Millán P, Castor A. Piezoelectric ceramics based on Bi_3TiNbO_9 from mechanochemically activated precursors. J Eur Ceram Soc 2001; 21: 1399-1402.

[209] Jiménez B, Castro A, Pardo L, Millán P, Jiménez R. Electric and ferro-piezoelectric properties of $(SBN)_{1-x}(BTN)_x$ ceramics obtained from amorphous precursors. J Phys Chem Solids 2001; 62: 951-958.

[210] Pardo L, Castro A, Millán P, Alemany C, Jiménez R, Jiménez B. $(Bi_3TiNbO_9)_x(SrBi_2Nb_2O_9)_{1-x}$ Aurimillius type structure piezoelectric ceramics obtained from mechanochemically activated oxides. Acta Mater 2000; 48: 2421-2428.

[211] Moure A, Castro A, Pardo L. Improvement by recrystallization of Aurivillius-type structure piezoceramics from mechanically activated precursors. Acta Mater 2004; 52: 945-957.

[212] Moure A, Alemany C, Pardo L. Electromechanical properties of SBN/BTN Aurivillius-tpye ceramics up to the transition temperature. J Eur Ceram Soc 2004; 24: 1687-1691.

[213] de Figueiredo R S, Messai A, Hernandes A C, Sombra A S B. Piezoelectric lithium miobate by mechanical alloying. J Mater Sci Lett 1998; 17: 449-451.

[214] Castro A, Jiménez B, Hungría T, Moure a, Pardo L. Sodium niobate ceramics prepared by mechanical activation assisted methods. J Eur Ceram Soc 2004; 24: 941-945.

[215] Takacs L. Multiple combustion induced by ball milling. Appl Phys Lett 1996: 69: 436-438.

[216] Thadhani N N. Shock-induced and shock-assisted solid-state chemical reactions in powder mixtures. J Appl Phys 1994; 76: 2129-2138.

[217] Kong L B, Ma J, Zhu W, Tan O K. Phase formation of lead zirconate titanate via a high-energy ball milling process. J Mater Sci Lett 2002; 21: 25-27.

[218] Jang H M, Oh S H, Moon J H. Thermodynamic stability and mechanisms of $Pb(Zn_{1/3}Nb_{2/3})O_3$ formation and decomposition of perovskite prepared by the PbO flux method. J Am Ceram Soc 1992; 75: 82-88.

[219] Wakiya N, Ishizawa N, Shinozake K, Mizutani N. Thermal stability of $Pb(Zn_{1/3}Nb_{2/3})O_3$ (PZN) and consideration of stabilization conditions of perovskite type compounds. Mater Res Bull 1995; 30: 1121-1131.

[220] Sundararaman D. Nanocrystalline state and solid state amorphization. Mater Sci Eng B 1995; 32: 307-313.

[221] Fukunaga T, Ussumi M, Akatsuka H, Misawa M, Mizutani U. Structure of amporphous Se prepared by milling. J Non-Cryst Solids 1996; 205-207: 531-535.

[222] Huang J Y, Yasuda H, Mori H. Deformation-induced amorphization in ball-milled silicon. Phil Mag Lett 1999; 79: 305-314.

[223] Yang X Y, Wu Y K, Ye H Q. Localized amorphization in SiC induced by ball milling. J Mater Sci Lett 2001; 20: 1517-1518.

[224] Schmücker M, Schneider H, Mackenzie K J D. Mechanical amorphization of mullite and thermal recrystallization. J Non-Cryst Solids 1998; 226: 99-104.

[225] Kosanovic C, Bronic J, Cizmek A, Subotic B, Smit I, Stubicar M, Tonejc A. Mechanochemistry of zeolites: part 2. change in particulate properties of zeolites during ball milling. Zoelites 1995; 15: 247-252.

[226] Wang X H, Chen P L, Chen I W. Two-step sintering of ceramics with constant grain-size, I. Y_2O_3. J Am Ceram Soc 2006; 89: 431-437.

[227] Wang X H, Deng X Y, Bai H L, Zhou H, Qu W G, Li L T, Chen I W. Two-step sintering of ceramics with constant grain-size, II. $BaTiO_3$ and Ni-Cu-Zn ferrite. J Am Ceram Soc 2006; 89: 4381-4343.

[228] Karmazin L, James W J. Precise measurement of lattice parameters of pseudocubic lattices. Acta Cryst 1972; A28: 183-187.

[229] Reaney I M, Petzelt J, Voitsekhovskii V V, Chu F, Setter N. B-site order and infrared reflectivity in $A(B'B'')O_3$ complex perovskite ceramics. J Appl Phys 1994; 76 (4): 2086-2092.

[230] Bidault O, Perrin C, Caranoni C, Menguy N. Chemical order influence on the phase transition in the relaxor $Pb(Sc_{1/2}Nb_{1/2})O_3$. J Appl Phys 2001; 90 (8); 4115-4121.

[231] Montgomery J K, Akbas M A, Davies P K. 1:1 ordered domain growth in $Pb(Mg_{1/3}Nb_{2/3})O_3$-$La(Mg_{2/3}Ta_{1/3})O_3$ relaxor ferroelectric perovskites. J Am Ceram Soc 1999; 82 (12): 3481-3484.

[232] Cantoni M, Bharadwaja S, Gentil S, Setter N. Direct observation of the B-site cationic order in the ferroelectric relaxor $Pb(Mg_{1/3}Ta_{2/3})O_3$. J Appl Phys 2004; 96 (7): 3870-3875.

[233] Farber L, Davies P. Influence of cation order on the dielectric properties of $Pb(Mg_{1/3}Nb_{2/3})O_3$-$Pb(Sc_{1/2}Nb_{1/2})O_3$ (PMN-PSN) relaxor ferroelectrics. J Am Ceram Soc 2003; 86 (11): 1861-1866.

[234] Xu Z, Gupta S M, Viehland D, Yan Y, Pennycook S J. Direct imaging of atomic ordering in undoped and La-doped $Pb(Mg_{1/3}Nb_{2/3})O_3$. J Am Ceram Soc 2000; 83 (1): 181-188.

[235] Guttler B, Mihailova B, Stosch R, Bismayer U, Gospodinov M. Local phenomena in relaxor-ferroelectric $PbSc_{0.5}B"_{0.5}O_3$ (B"=Nb, Ta) studied by Raman spectroscopy. J Molecular Structure 2003; 661-662: 469-479.

[236] Dias A, Moreira R L. Far-infrared spectrodcopy in ordered and sisordered $BaMg_{1/3}Nb_{2/3}O_3$ micowave ceramics. J Appl Phys 2003; 94 (5):2414-2421.

[237] Wongmaneerung R, Yimnirun R, Ananta S. Effect of vibro-milling time on phase formation and particle size of lead titanate nanopowders. Mater Lett 2006; 60: 1447-1452.

[238] Soon H P, Xue J M, Wang J. Dielectric behaviors of $Pb_{1-3x/2}La_xTiO_3$ derived from mechanical activation. J Appl Phys 2004; 95 (9): 4981-4988.

[239] Kim M H, Golovhanski A, Lee S I, Park T G, Song T K. Synthesis of $Pb(Zr,Ti)O_3$ nanopowders by milling coprecipitation method. J Electroceramics 2004; 13: 367-371.

[240] Parashar S K S, Choudhary R N P, Murty B S. Size effect of $Pb_{0.92}Nd_{0.08}(Zr_{0.53}Ti_{0.47})_{0.98}O_3$ nanoceramic synthesized by high-energy ball milling. J Appl Phys 2005; 98 (10): 104305-1-8.

[241] Liu X, Akdogan E K, Safari A, Riman R E. Mechanically activated synthesis of PZT and its electromechanical properties. Appl Phys A 2005; 81: 531-537.

[242] Alguero M, Ricote J, Castro A. Mechanosynthisis and thermal stability of piexoelectric perovskite $0.92Pb(Zn_{1/3}Nb_{2/3})O_3$-$0.08PbTiO_3$ powders. J Am Ceram Soc 2004; 87 (5): 772-778.

[243] Welham N J. Mechanically induced reaction between alkaline earth metal oxides and TiO_2. J Mater Res 1998; 13 (6): 1607-1613.

[244] Stojanovic B D, Jovalekic C, Vukotic V, Simoes A Z, Varela J A. Ferroelectric properties of mechanically synthesized nanosized barium titanate. Ferroelectrics 2005; 319: 65-73.

[245] Hungria T, Alguero M, Hungria A B, Castro A. Dense, fine-grained $Ba_{1-x}Sr_xTiO_3$ ceramics prepared by the combination of mechanosynthesized nanopowders and spark plasma sintering. Chem Mater 2005; 17: 6205-6212.

[246] Stojanovic B D, Paiva-Santos C O, Jovalekic C, Simoes A Z, Filho F M, Lazarevic Z, Varela J A. Mechanically activating formation of layered structured bismuth titanate. Mater Chem Phys 2006; 96: 471-476.

[247] Zdujic M, Poleti D, Jovalekic C, Karanovic L. The evolution of structure induced by intensive milling in the system $2Bi_2O_3{\cdot}3TiO_2$. J Non-Cryst Solids. 2006; 352: 3058-3068.

[248] Chew C L, Srinivas A, Sritharan T, Boey F Y C. Mechanochemical activation of strontium bismuth tantalate synthesis. Scripta Mater 2005; 53: 1197-1199.

[249] Cross L E and Newnham R E. History of ferroelectrics, Ceramics and Civilization, Volume III, High-Technology Ceramics - Past, Present and Future, American Ceramic Society, Westerville, OH, 1987, p289-305.

[250] (a) Kong L B, Ma J, Zhu W, Tan O K. Highly enhanced sinterability of commercial PZT powders by high-energy ball milling. Mater Lett 2000; 46: 274-280. (b) Kong L B. unpublished works.

[251] Pavlovic C V P, Nikolic M V, Pavlovic V B, Labus N, Zivkovic Lj, Stojanovic B D. Correlation between densification rate and microstructure evolution of mechanically activated $BaTiO_3$. Ferroelectrics 2005; 319: 75-85.

[252] Tusseau-Nenez S, Ganne J P, Maglione M, Morell A, Niepce J C, Pate M. BST ceramics: effect of attrition milling on dielectric properties. J Eur Ceram Soc 2004; 24: 3003-3011.

[253] Stojanovic B D, Simoes A Z, Paiva-Santos C O, Quinelato C, Longo E, Varela J A. Effect of processing route on the phase formation and properties of $Bi_4Ti_3O_{12}$ ceramics. Ceram Int 2006; 32: 707-712.

[254] Goto F J, Real C, Dianez M J, Criado J M. Repationships between the texture and structure of $BaTiO_3$ and its tetragonal-cubic transition enthalpy. J Solid State Chem 1996; 123: 301-305.

[255] Lee B I, Wang X, Kwon S J, Maie H, Kota R, Hwang J H, Park J G, Hu G. Synthesis of high tetragonality nanoparticle $BaTiO_3$. Microelectronic Eng 2006; 83: 463-470.

[256] Suzuki K, Kijima K. Phase transformation of $BaTiO_3$ nanoparticles synthesized by RF-plasma CVD. J Alloys Comp 2006; 419: 234-242.

[257] Sun W, Li C, L J, Liu W. Microwave-hydrothermal synthesis of tetragonal $BaTiO_3$ under various conditions. Mater Chem Phys 2006; 97: 481-487.

[258] Maison W, Kleeberg R, Heimann R B, Phanichphant S. Phase content, tetragonality, and crystalline size of nanoscaled barium titanate synthesized by the catecholate process: effect of calcination temperature. J Eur Ceram Soc 2003; 23: 127-132.

[259] Buscaglia M T, Buscaglia V, ViViani M, Nanni P, Hanuskova M. Influence of foreign ions on the crystal structure of $BaTiO_3$. J Eur Ceram Soc 2000; 20: 1997-2007.

Figure Captions:

Fig. 1 The perovskite structure of $PbTiO_3$, having a cubic structure in the paraelectric phase and tetragonal structure in the ferroelectric phase [2].

Fig. 2 Schematic diagram of residual stress distribution of $PbTiO_3$ ceramics with coarse grains (A) and fine grains [33].

Fig. 3 XRD patterns of the mixture of PbO and TiO_2 powders milled for different times, using a SPEX shaker-mill operated at ~900 rpm (open circle: PbO, filled rhombus: TiO_2, filled circle: PT) [39].

Fig. 4 TEM image of the 20-hour-milled PbO and TiO_2, showing an average particle size of 20-30 nm of the PT powders, using a SPEX shaker-mill [39].

Fig. 5 XRD patterns of the mixtures of PbO and TiO_2 milled different times: (a) anatase and (b) rutile [41].

Fig. 6 TEM images and diffraction pattern of starting TiO_2 and milled powders: (a) anatase, (b) rutile; (c), (d) and (e): PbO/TiO_2 (anasase) milled for 2, 20 and 80 h; (f) diffraction pattern of sample (e) [41].

Fig. 7 XRD patterns of the 20-h-milled mixtures with different PbO/TiO_2 (anatase) ratios [47].

Fig. 8 SEM images of the surface microstructure of the $PbTiO_3$ ceramics sintered at 1100 ℃ for 1 h, derived from the powders milled for (a) 20 h, (b) 40 h, (c) 60 h and (d) 80 h [42].

Fig. 9 DTA curves of the $PbTiO_3$ ceramics derived from the 20-h-milled powders [42].

Fig. 10 Phase diagram of $PbZr_{1-x}Ti_xO_3$ [2, 99].

Fig. 11 XRD patterns of the mixture of PbO, ZrO_2 and TiO_2 powders milled for different times using a SPEX shaker-mill operated at ~900 rpm (open circle: PbO, filled rhombus: ZrO_2, open down triangle: TiO_2 and fill circle: PZT) [62, 63].

Fig. 12 XRD patterns of the unmilled mixture of PbO, ZrO_2 and TiO_2 powders mixture of calcined at different temperatures (open circle: PbO, filled rhombus: ZrO_2, open down triangle: TiO_2, fill square: $PbTiO_3$ and filled circle: PZT) [63].

Fig. 13 XRD patterns of 10-h-milled mixture of PbO, ZrO_2 and TiO_2 powders calcined at different temperatures (open circle: PbO and filled circle: PZT) [63].

Fig. 14 Relative density of the PZT ceramics made from the mixture of PbO, ZrO_2 and TiO_2 powders, milled for 0, 10 and 25 h using a SPEX shaker-mill, as a function of sintering temperature (5 ℃/min, 1 h) [63].

Fig. 15 XRD patterns of the mixtures for PZT milled for different times, using a planetary high-energy ball mill and tungsten carbide media [65].

Fig. 16 Densification behaviors of the mixtures for PZT milled for different times, using a planetary high-energy ball mill and tungsten carbide media [65].

Fig. 17 SEM image of the PZT ceramics made from the 4-h-milled mixture of PbO, ZrO_2 and TiO_2 powders sintered at 900 ℃ for 4 h [47].

Fig. 18 P-E hystersis curves of the PZT ceramics derived from the 4-h-milled powders sintered at different temperatures for 4 h [47].

Fig. 19 Room temperature phase diagram of PLZT solid solution (AFE_O: antiferroelectric orthorhombic, FE_{Rh}: ferroelectric rhombohedral, PE_{Cubic}: paraelectric cubic, FE_{Tet}: ferroelectric tetragonal and RFE: relaxor ferroelectric) [1, 80].

Fig. 20 XRD patterns of the 36-h-milled mixtures for (a) PLZT8/65/35, (b) PLZT15/65/35 and (c) PLZT2/95/5 [94].

Table Captions:

Table 1. Relative dielectric constant (ε) and dielectric loss (tan δ) of the sintered PZT made from the powders that were mechanically activated for 0, 10 and 25 h, respectively (SPEX shaker-mill, stainless steel media). All values were measured at room temperature at frequency of 1 kHz [63].

Table 2. Summary of the densification behaviors of the mixtures for PZT milled for different times, using a planetary high-energy ball mill with tungsten carbide media [65].

Table 3. Ferroelectric parameters of the PLZT8/65/35 ceramics derived from the 36-h-milled mixture [95].

Table 4. Antiferroelectric parameters of the PLZT2/95/5 ceramics [94].

Table 5. Dielectric and ferroelectric parameters of the PMN ceramics sintered at different temperatures [94].

Table 6. Dielectric properties of the 0.9PMN-0.1PT ceramics derived from the mechanochemically synthesized powder [147].

Table 7. Properties of the (1-x)PZN-xBT ceramics [155].

Table 8. Dielectric properties of the PZN-PMN-PT ceramics derived from the mixtures with different starting materials [165-167].

Table 9. Properties of the $Bi_4Ti_3O_{12}$ ceramics sintered at different temperatures [188].

Table 10. Annealing conditions (temperature and time) for BiT phase formation and single phase from different precursors [190].

Table 11. Dielectric ferroelectric and pyroelectric properties of coarse- and fine-grained BiV ceramics [192].

Table 12. Properties of the CBiT and SBiT ceramics derived from the synthesized nano-sized powders [203, 204].

Table 13. Phase composition of mixture of $SrCO_3$, Bi_2O_3 and TiO_2 for SBiT after mechanical activation for different times, using a vibrating mill (VM) and a planetary mill (PM) [205].

Table 14. Phase compositions after thermal annealing of the samples obtained by solid-state reaction (SSR), mechanical activation by vibrating milling for 168 h (VM) and planetary milling for 12 h (PM12) and for 108 h (PM108)* [205].

Table 1.

Sintering temperature (℃)	ε			tanδ (%)		
	Mechanical activation time (h)			Mechanical activation time (h)		
	0	10	25	0	10	25
1000	/	1034	1174	/	1.1	1.4
1050	/	1065	1334	/	1.5	1.1
1100	574	1094	1384	42	1.0	1.0
1150	588	1113	1287	24	1.1	1.0
1200	635	1106	1174	18	1.0	0.7
1250	667	/	/	9	/	/
1300	616	/	/	6	/	/

Table 2.

Milling time (h)	Expansion peak (°C)	First shrinkage peak (°C)	Second shrinkage peak (°C)
4	771	813	858
8	763	808	837
15	752	797	807
24	/	791	801

Table 3.

	900°C	1000°C	1100°C	1200°C
P_S (μC/cm^2)	9.7	18.8	24.3	32.8
P_r (μC/cm^2)	2.1	6.3	11.8	22.1
E_C (kV/cm)	6.9	9.6	8.7	8.2

Table 4.

	900°C	1000°C	1100°C	1200°C
P_S (μC/cm^2)	12	51	58	65
E_{AFE-FE} (kV/cm)	/	86	79	63
E_{FE-AFE} (kV/cm)	/	45	33	24

Table 5.

Sintering temperature (°C)	950	1000	1050	1100
Relative density (%)	96.1	96.8	97.7	97.5
Average grain size (μm)	1.2	2.1	3.6	4.8
Dielectric constant	10317	10750	13873	13979
Dielectric loss (%)	5.94	5.64	6.2	6.6
Remanent polarization (μC/cm^2)	2.3	2.8	3.3	4.6
Coercive field (kV/cm)	9.8	8.3	6.1	5.3

Dielectric properties were measured at 1 kHz at room temperature.

Table 6.

Sintering temp. (℃)	K_{max} at T_C	T_C (℃) K at room temp.	K at room temp.	$tan\delta$ at room temp.
950	5763	49	5100	0.045
1000	7870	49	7282	0.047
1050	18700	47	14322	0.040
1100	21150	46	16847	0.046
1150	26500	45	17252	0.048

Table 7.

Composition x	Percentage of perovskite (%)	Grain size (μm)	Relative density (%)	Dielectric constant (1 kHz)
0.05	95	4.5	93	3105
0.10	100	3.1	95	4623
0.15	100	2.6	95	9254
0.20	100	2.1	96	5983
0.25	100	1.6	96	4135
0.30	100	1.2	97	3306

Table 8.

Sintering temp. (℃)	Curie temp. (℃)	ε_{max} at T_C	ε at room temp.	tanδ at room temp.
		Oxide mixture		
900	109	11091	3272	0.0654
950	108	13109	3316	0.0465
1000	107	14194	3469	0.0460
1050	106	16852	3627	0.0625
1100	103	18986	3820	0.0485
		Colubite mixture		
930	116	8515	2305	0.0430
950	115	11270	2536	0.0470
1000	114	16500	2635	0.0560
1050	113	17266	2721	0.0540
1100	112	18580	2852	0.0460

Table 9.

	750 ℃	850 ℃	950 ℃
d (g/cm^3)	7.7	7.91	7.79
G (μm)	3.6	5.1	6.8
K (at 1 kHz)	189	243	312
tanδ (at 1 kHz)	0.015	0.017	0.021
Pr (μC/cm^2)	20	24	13
V_C (kV/cm)	15	11	10
k_{33} (%)	37	56	47
k_{31} (%)	38	58	48

Table 10.

Sample	BiT formation (℃/h)	Single phase BiT (℃/h)
n-butylamine precursor	600/1	750/1
Solid-state reaction	600/12	850/12
Vibrating milling for 72 h	500/12	600/12
Vibrating milling for 168 h	500/12	600/3
Planetary milling for 19 h	400/1	600/1
Planetary milling for 72 h	460/3	550/1

Table 11.

	Coarse-grained ceramics	Fine-grained ceramics
Dielectric constant at RT (10 kHz)	130	190
Dielectric constant at T_C (10 kHz)	6500	20000
Pyroelectric figure of merit ($mC\ m^{-2}\ K^{-1}$)	140	2650
Remanent polarization (P_r) ($C\ cm^{-2}$)	2.25×10^{-8}	24.6×10^{-8}
Coercive field (E_C) ($V\ cm^{-1}$)	650	480

Table 12.

	CBiT	SBiT
Sintering temperature (℃)	1175	1175
Relative density (%)	93.4	98
Curie temperature T_C (℃)	774	539
Maximum dielectric constant at T_C	1049 at 1 MHz	2770 at 100 kHz

Table 13.

Time (h)	VM	PM
1		M
2		M
4		M+A
5	M	M+A
6		A+C
7		A+C
10		A+C
11		A
12		A
18		A
24	M+A	A
48	A+C	A
72	A+C	A
108		A
168	A	

*M=mixture of initial oxides, A=amorphous and C=$SrCO_3$. Major components are listed first.

Table 14.

Annealing (℃/h)	SSR	VM	PM12	PM108
300/1		A+C	A+C^{tr}	A
350/1		F+C	F+C^{tr}	A
400/1		F+C	F+C^{tr}	A+n4tr+$n3^{tr}$
450/1		F+n4+C	F+n4+C^{tr}	n4+n3
500/1		F+n4+C	F+n4	n4+n3
550/1		F+n4	n4+F	n4
600/1		n4+F^{tr}	n4	n4
600/5		n4	n4	n4
800/12	S+n3+n4	n4	n4	n4
900/12	n4+S+$n3^{tr}$	n4	n4	n4
1000/12	n4+S	n4	n4	n4
1050/12	n4	n4	n4	n4
1100/12	n4	n4	n4	n4

*A=amorphous, C=$SrCO_3$,S=$SrTiO_3$, F=Sr-Bi-Ti-O fluorite, n3=$Bi_4Ti_3O_{12}$, n4=$SrBi_4Ti_4O_{15}$, ^{tr}=traces. SSR treatments are cumulative, VM, PM12 and PM108 treatments are not cumulative.

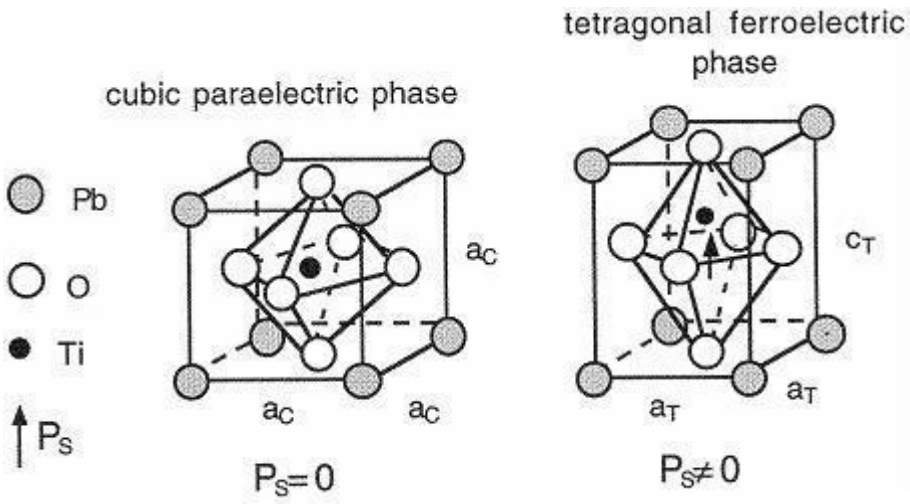
tetragonal ferroelectric phase
cubic paraelectric phase
Pb
O
Ti
P_S
a_C
a_C
a_C
$P_S = 0$
c_T
a_T
a_T
$P_S \neq 0$

Fig. 1

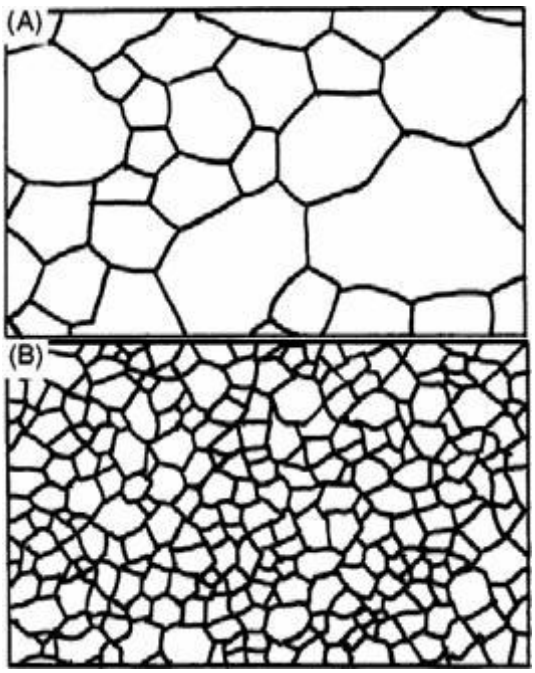
(A)
(B)

Fig. 2

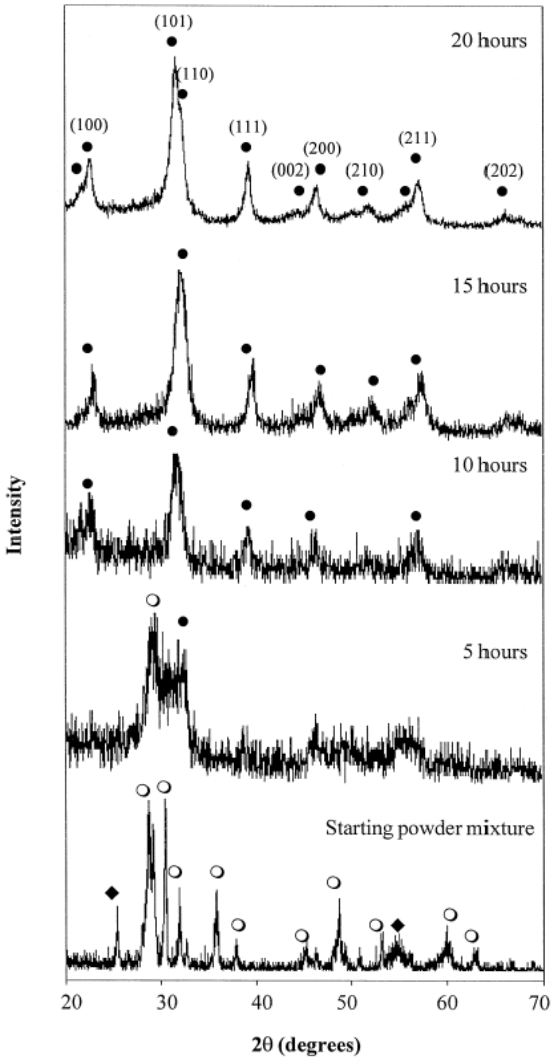
(101)
(110)
(100)
(111)
(200)
(002)
(210)
(211)
(202)
20 hours
15 hours
10 hours
5 hours
Starting powder mixture
Intensity
20
30
40
50
60
70
2θ (degrees)

Fig. 3

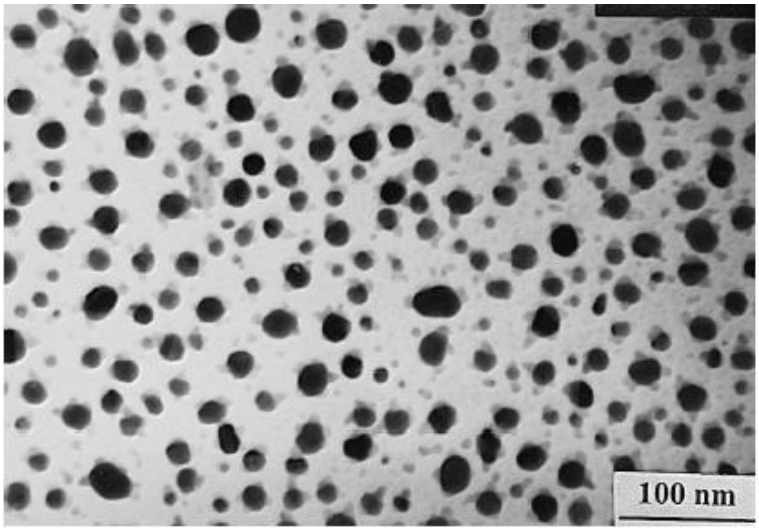
100 nm

Fig. 4

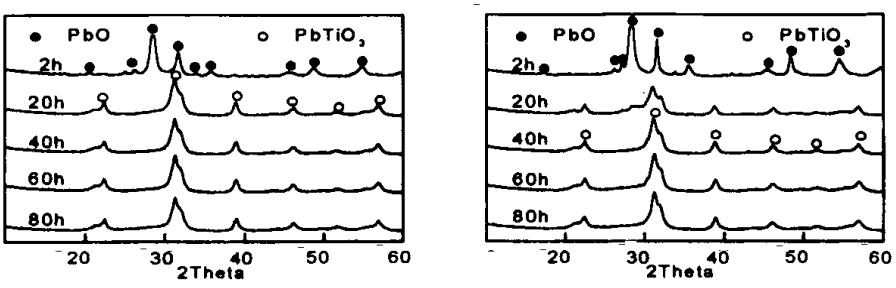
PbO
PbTiO3
2h
20h
40h
60h
80h
20
30
40
50
60
2Theta
PbO
PbTiO3
2h
20h
40h
60h
80h
20
30
40
50
60
2Theta

(a) (b)

Fig. 5

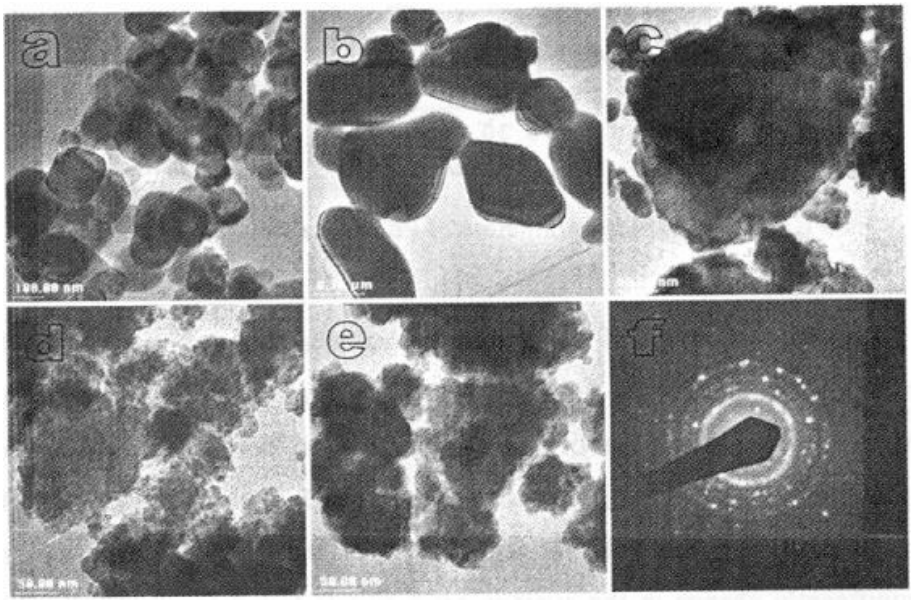
a
b
c
d
e
f

Fig. 6

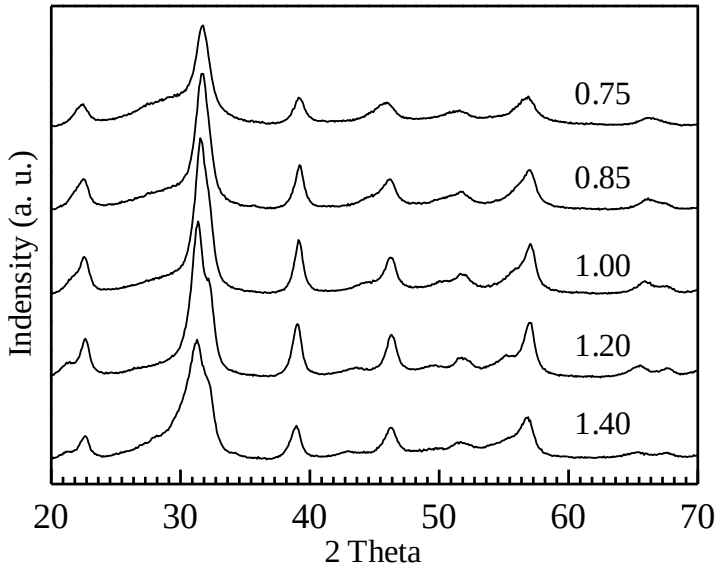
0.75
0.85
1.00
1.20
1.40
Indensity (a. u.)
20
30
40
50
60
70
2 Theta

Fig. 7

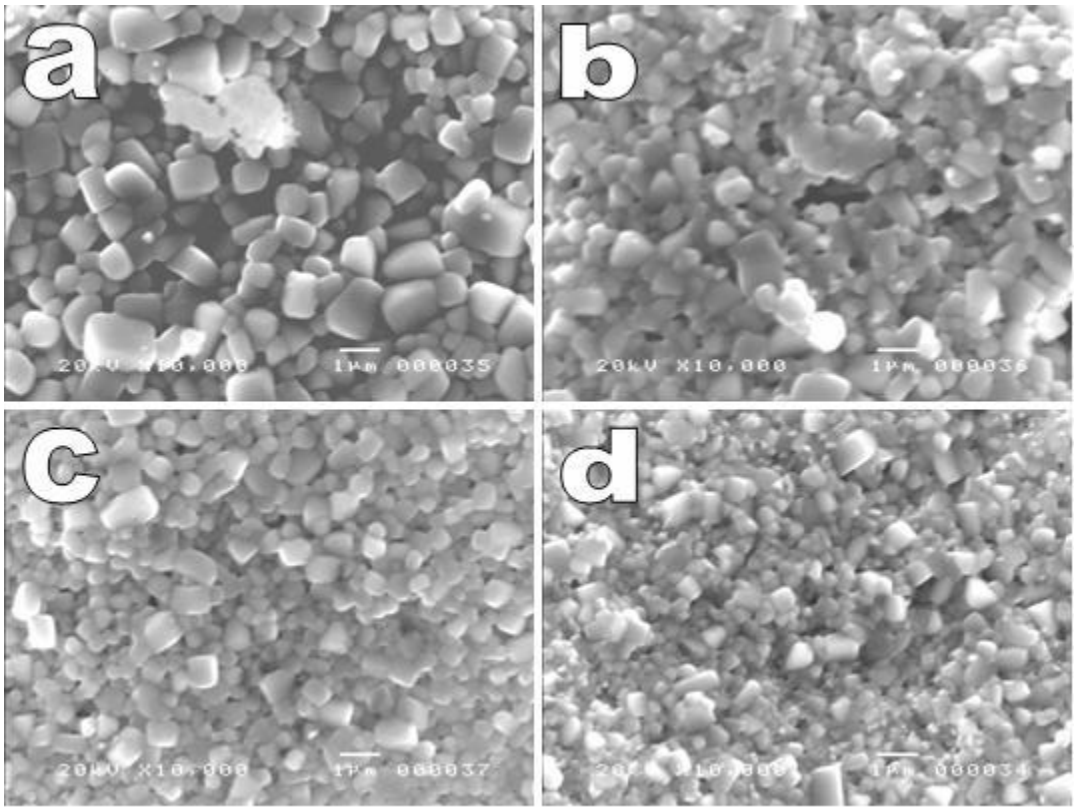
a
b
c
d

Fig. 8

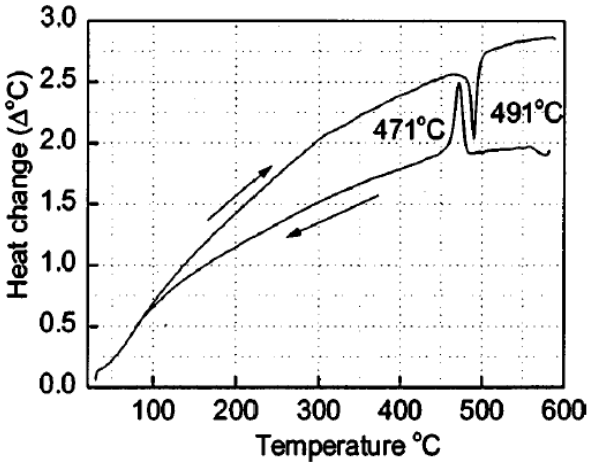
Heat change (Δ°C)
3.0
2.5
2.0
1.5
1.0
0.5
0.0
100
200
300
400
500
600
Temperature °C
471°C
491°C

Fig. 9

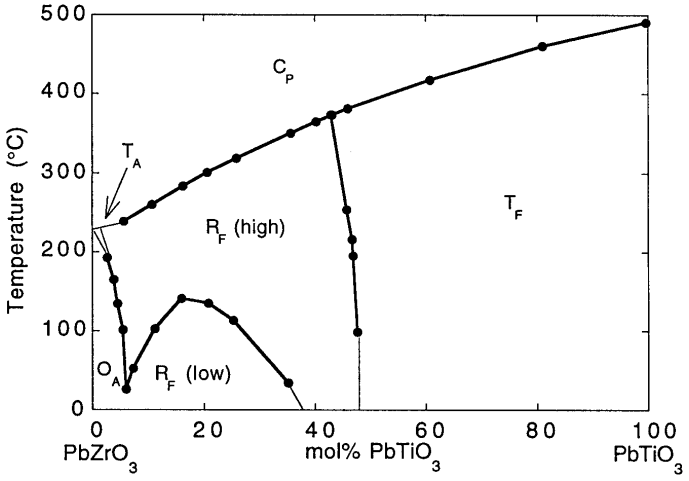
500
400
300
200
100
0
Temperature (°C)
C_P
T_A
R_F (high)
T_F
O_A
R_F (low)
0
20
40
60
80
100
PbZrO3
mol% PbTiO3
PbTiO3

Fig. 10

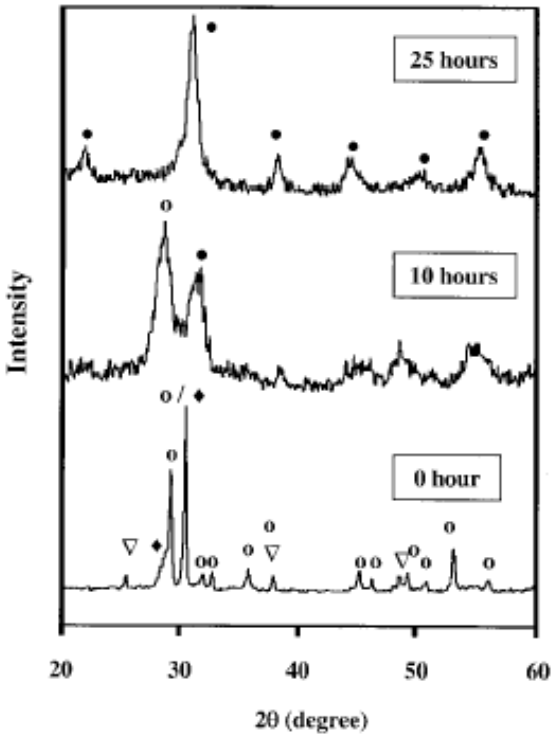
25 hours
10 hours
0 hour
Intensity
20
30
40
50
60
2θ (degree)

Fig. 11

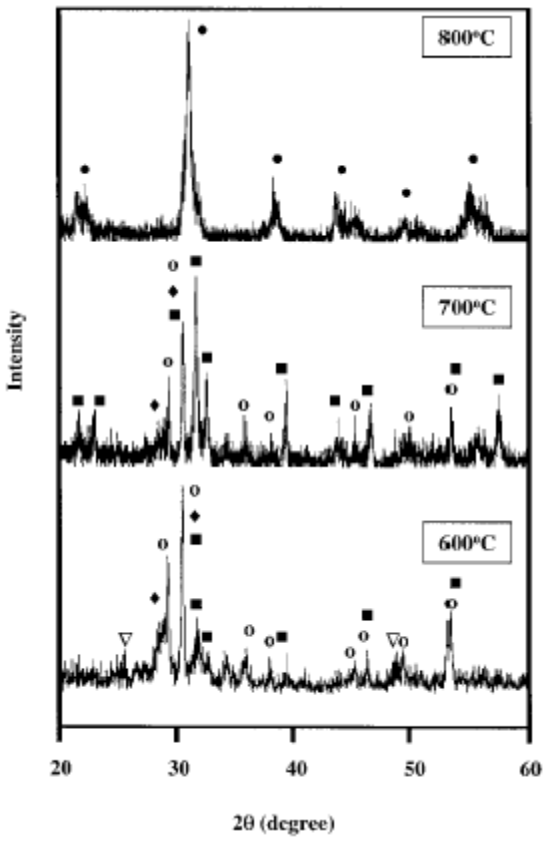

Fig. 12

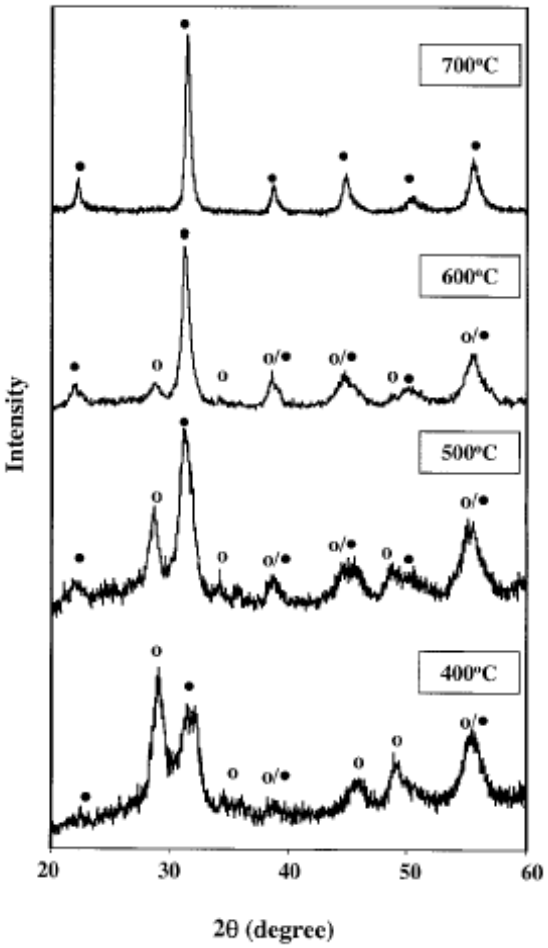

Fig. 13

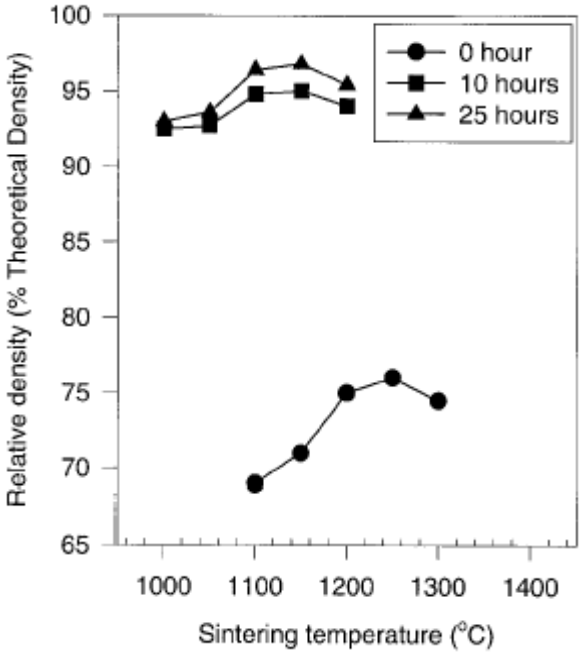
0 hour
10 hours
25 hours
Relative density (% Theoretical Density)
100
95
90
85
80
75
70
65
1000
1100
1200
1300
1400
Sintering temperature (°C)

Fig. 14

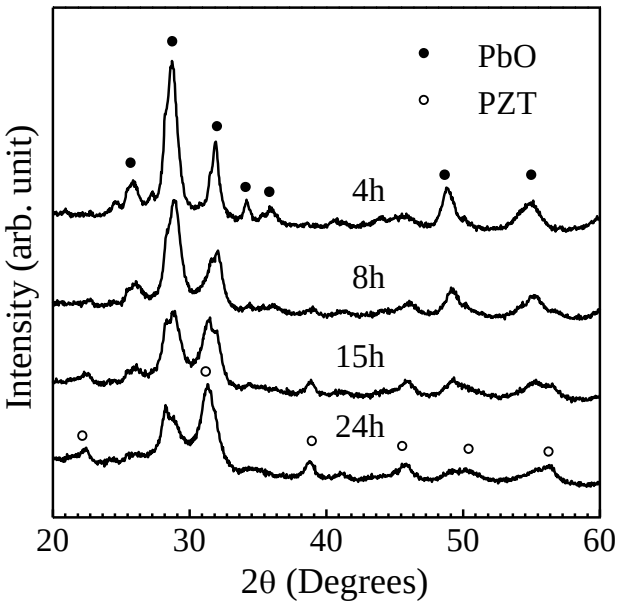
PbO
PZT
4h
8h
15h
24h
Intensity (arb. unit)
20
30
40
50
60
2θ (Degrees)

Fig. 15

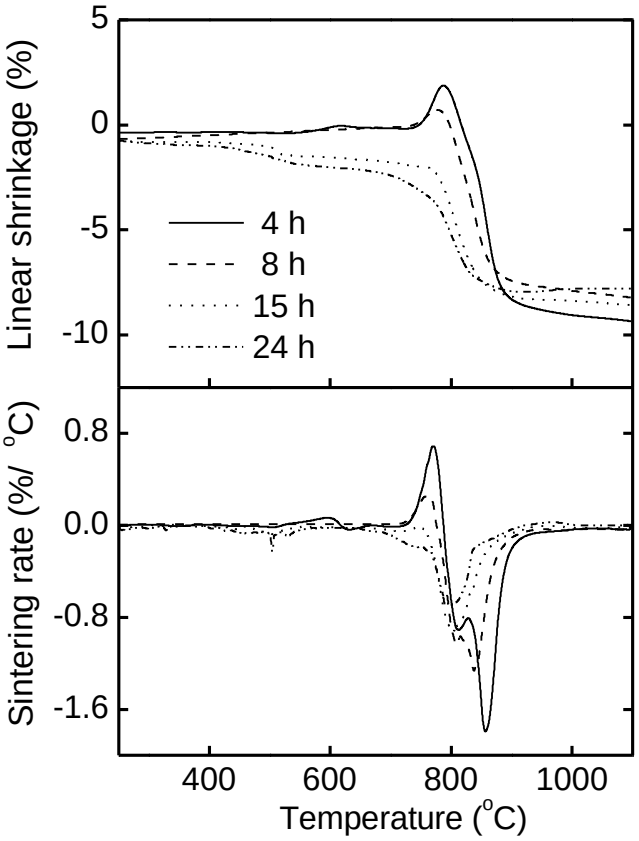
Linear shrinkage (%)
5
0
-5
-10
4 h
8 h
15 h
24 h
Sintering rate (%/ °C)
0.8
0.0
-0.8
-1.6
400
600
800
1000
Temperature (°C)

Fig. 16

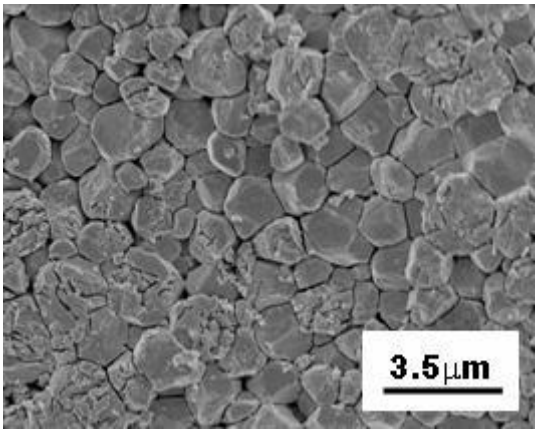
3.5μm

Fig. 17

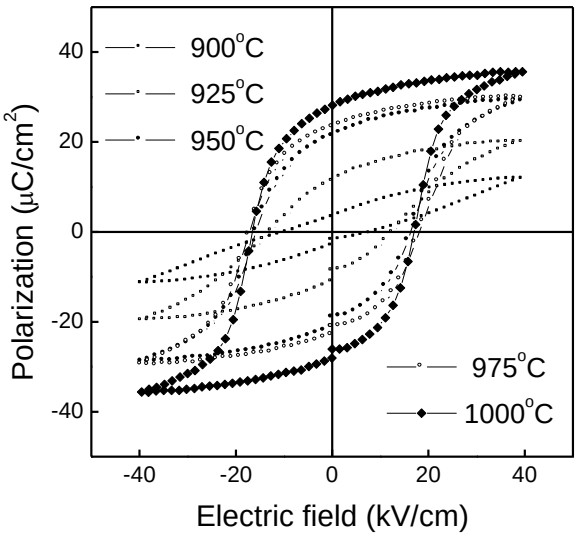
900°C
925°C
950°C
975°C
1000°C
Polarization (μC/cm²)
Electric field (kV/cm)
40
20
0
-20
-40
-40
-20
0
20
40

Fig. 18

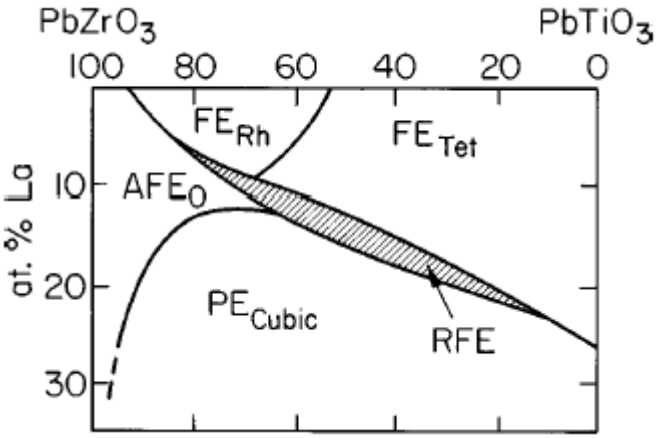
PbZrO3
PbTiO3
100
80
60
40
20
0
FERh
FETet
AFE0
PECubic
RFE
at. % La
10
20
30

Fig. 19

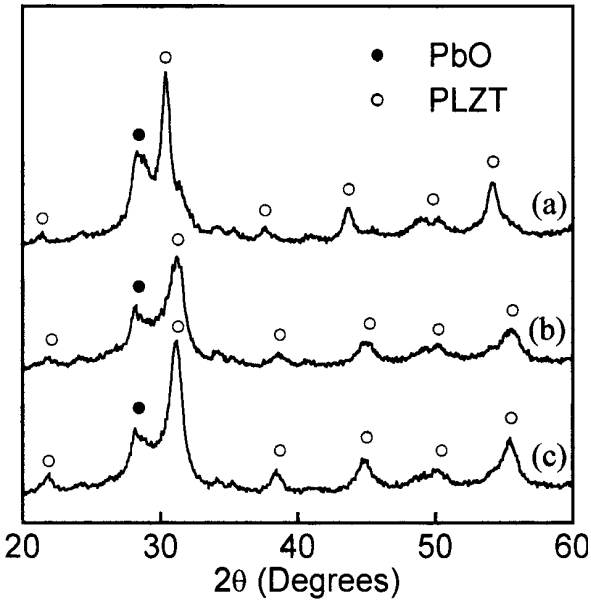
PbO
PLZT
(a)
(b)
(c)
20
30
40
50
60
2θ (Degrees)

Fig. 20

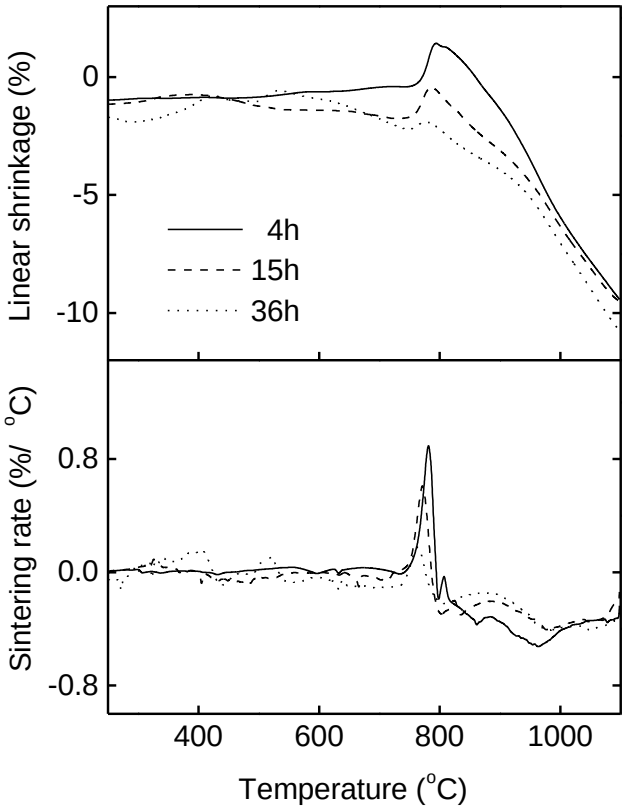
Linear shrinkage (%)
0
-5
-10
4h
15h
36h
Sintering rate (%/ °C)
0.8
0.0
-0.8
400
600
800
1000
Temperature (°C)

Fig. 21

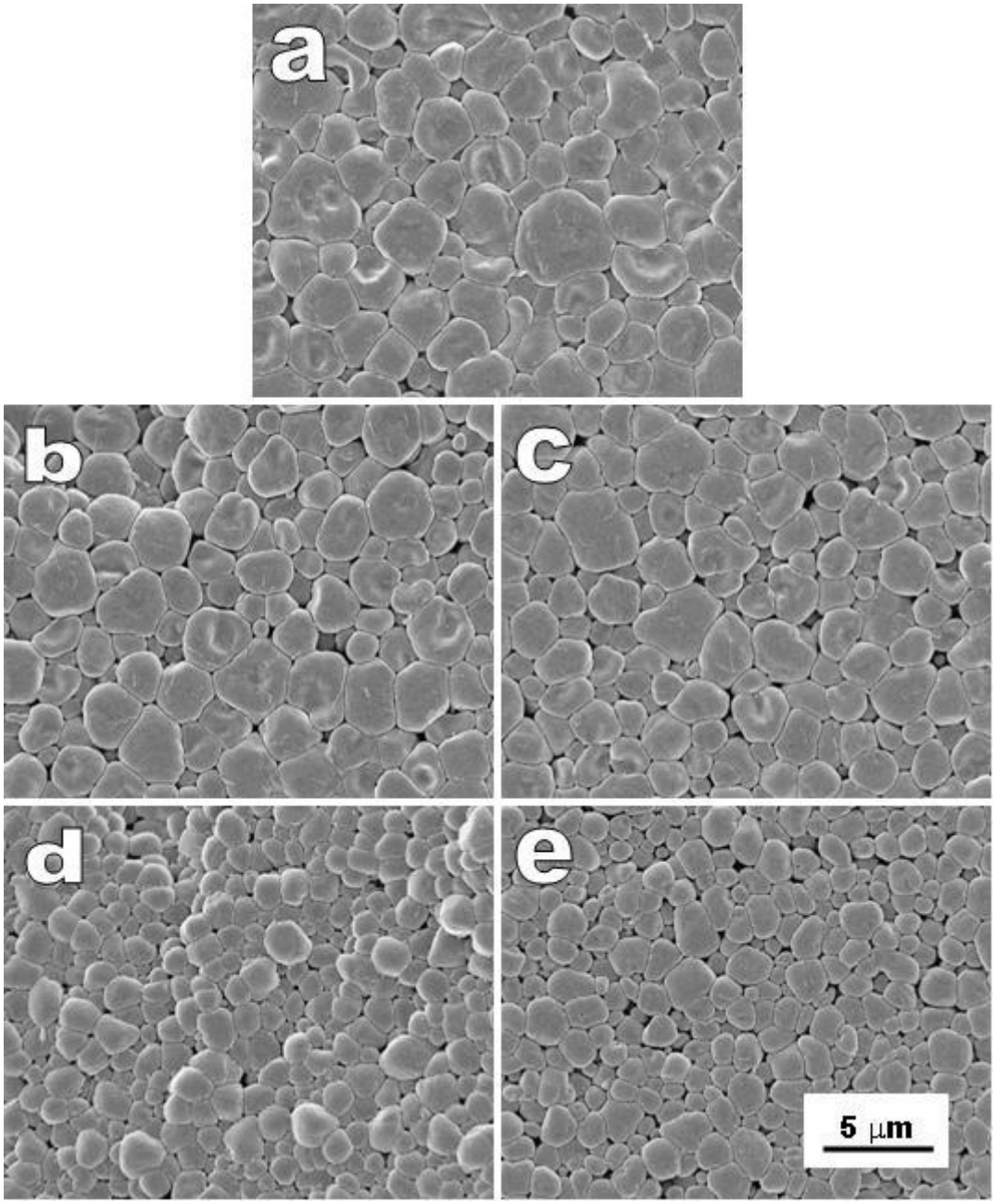

Kong *et al*, Fig. 22

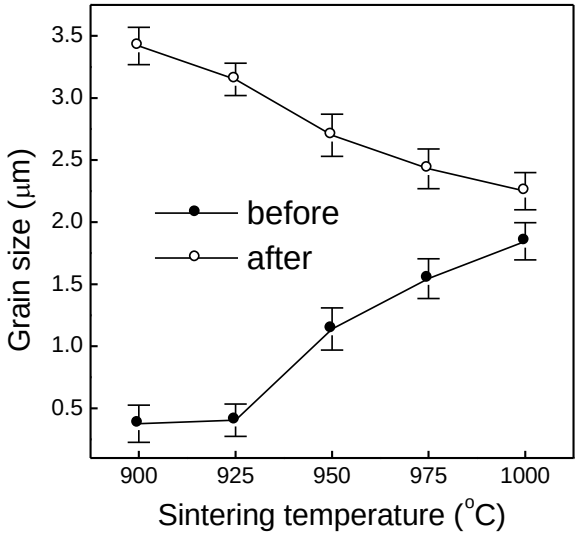

Kong *et al*, Fig. 23

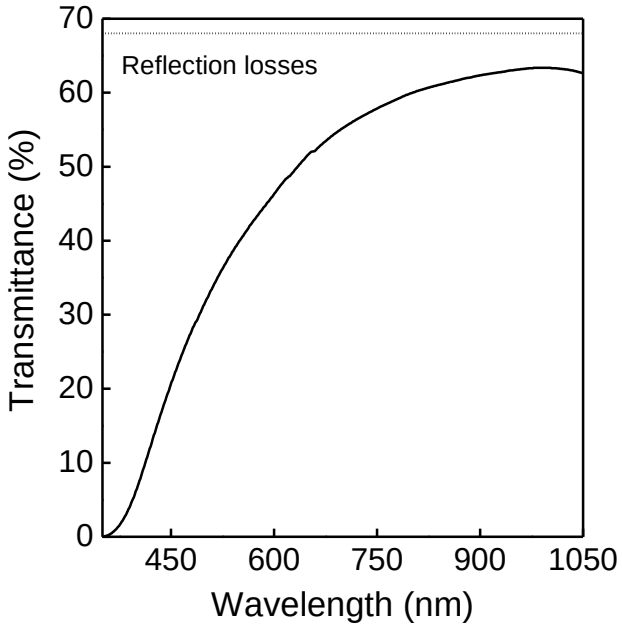

Fig. 24

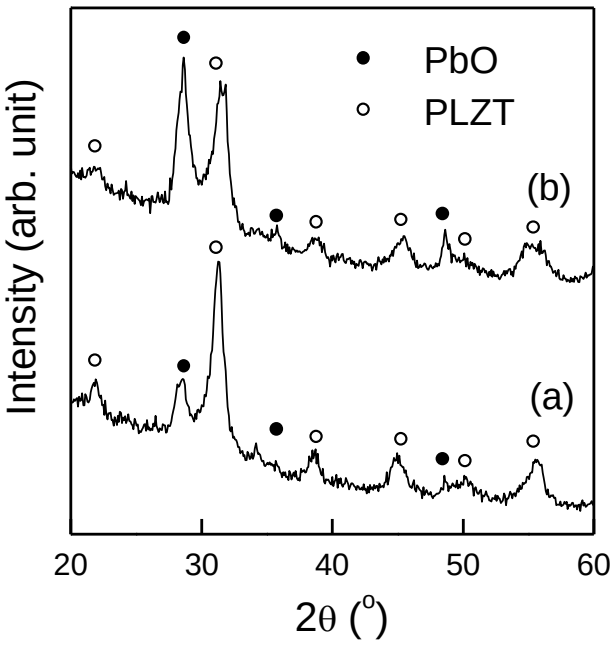

Fig. 25

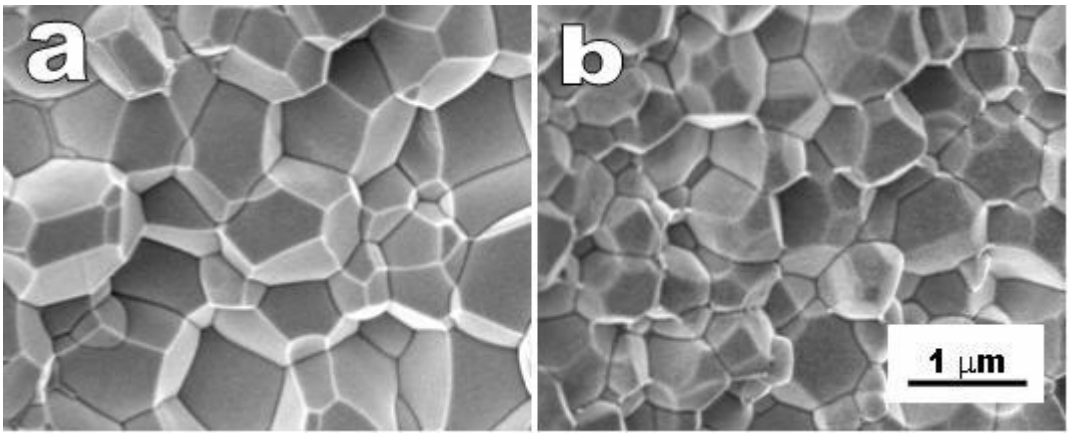

Kong *et al*, Fig. 26

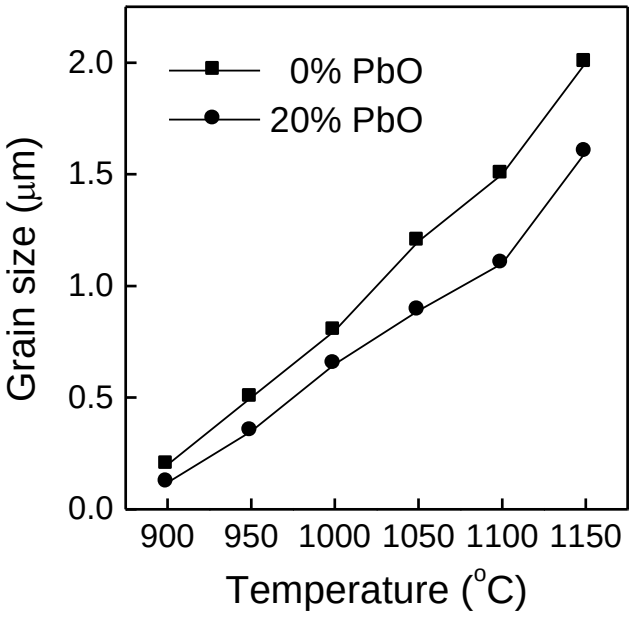

Fig. 27

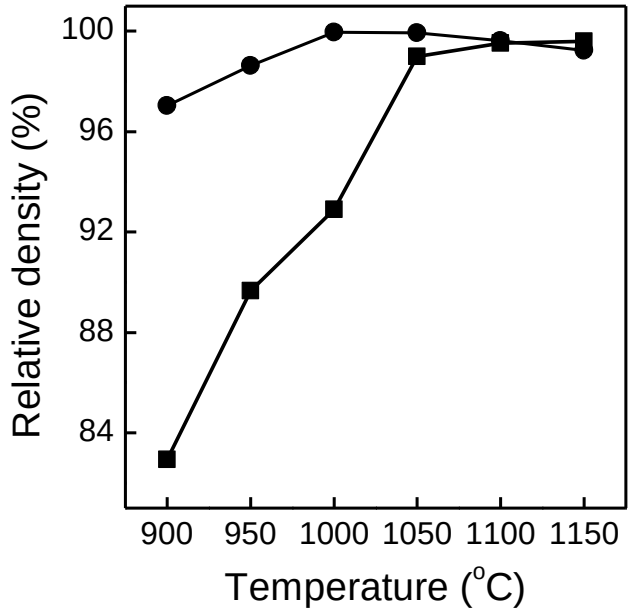

Kong *et al*, Fig. 28

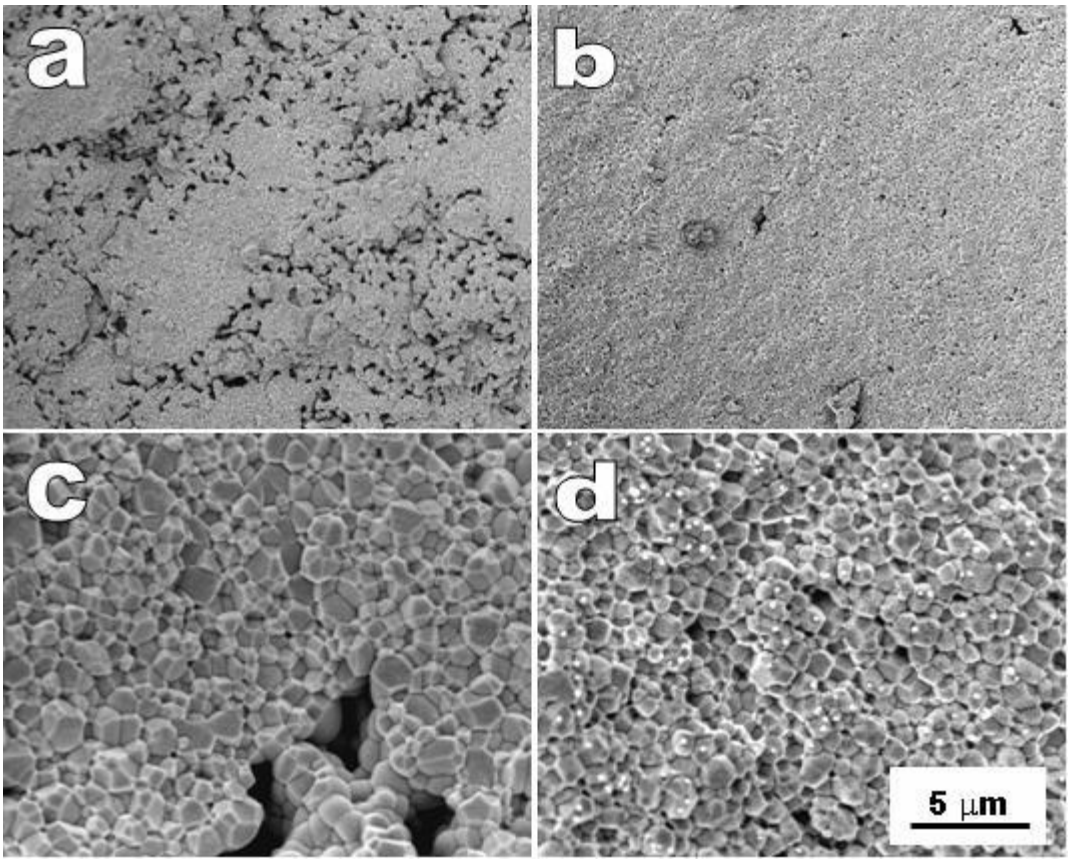

Kong *et al*, Fig. 29

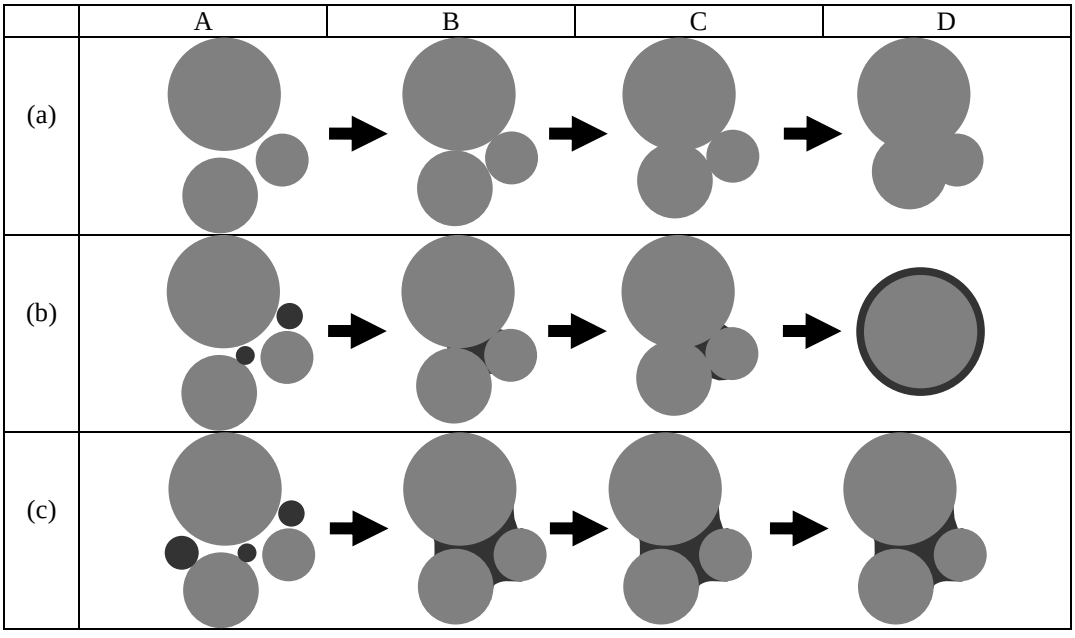

Fig. 30

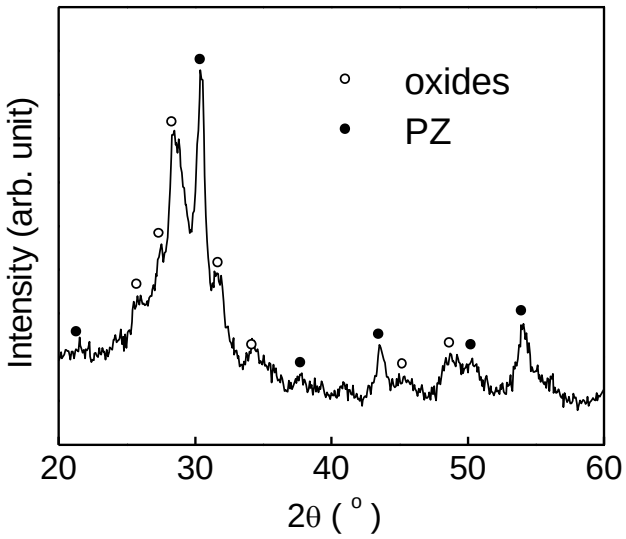
oxides
PZ
Intensity (arb. unit)
20
30
40
50
60
2θ (o)

Fig. 31

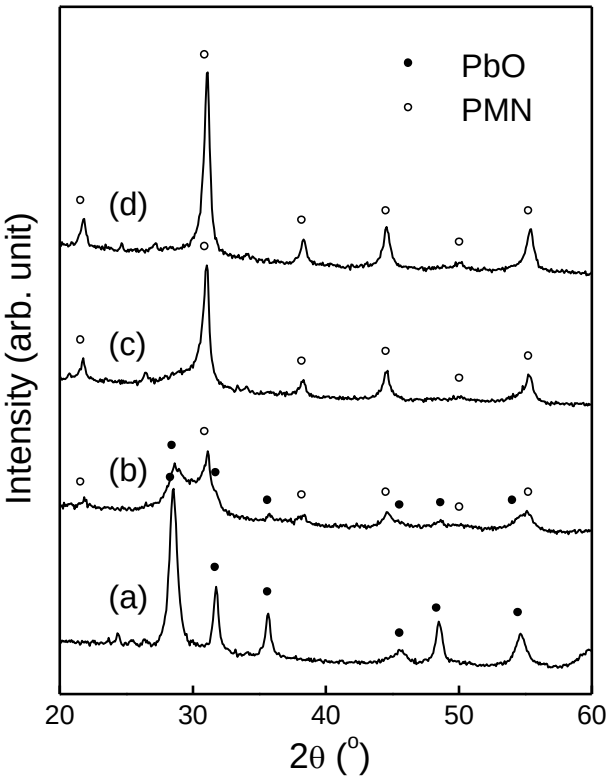
PbO
PMN
(d)
(c)
(b)
(a)
Intensity (arb. unit)
20
30
40
50
60
2θ (o)

Fig. 32

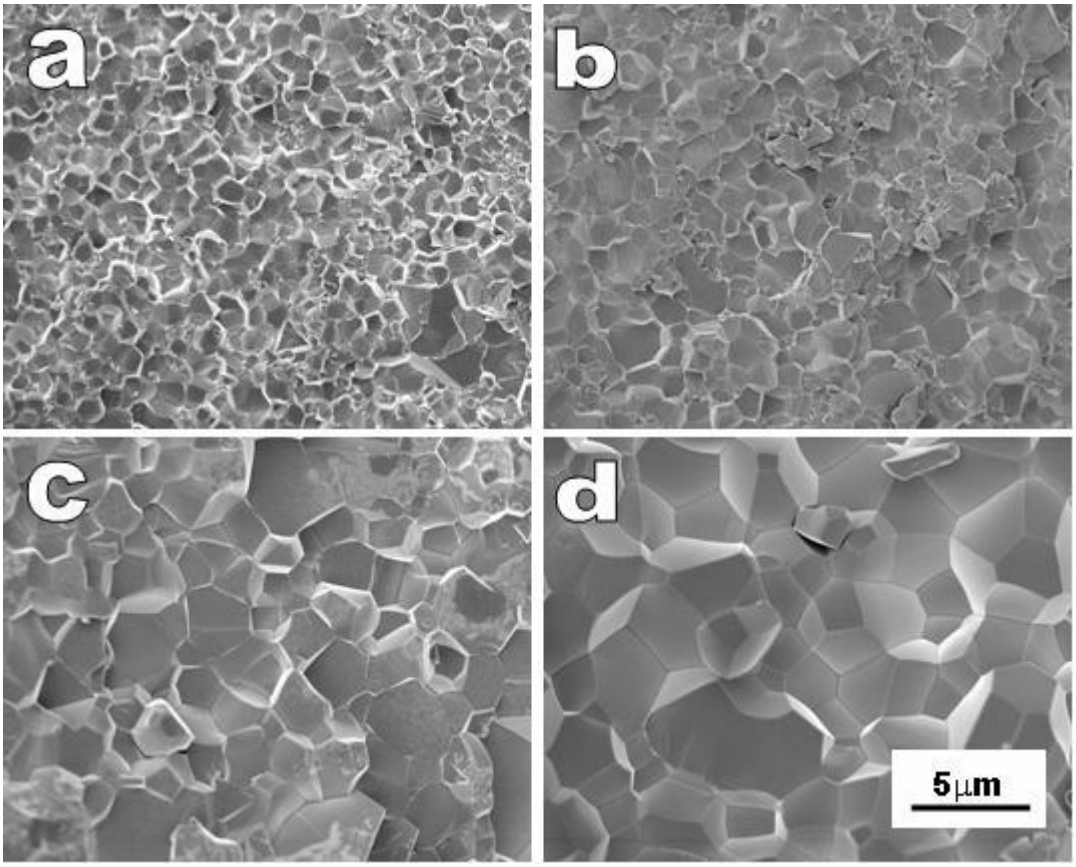

Fig. 33

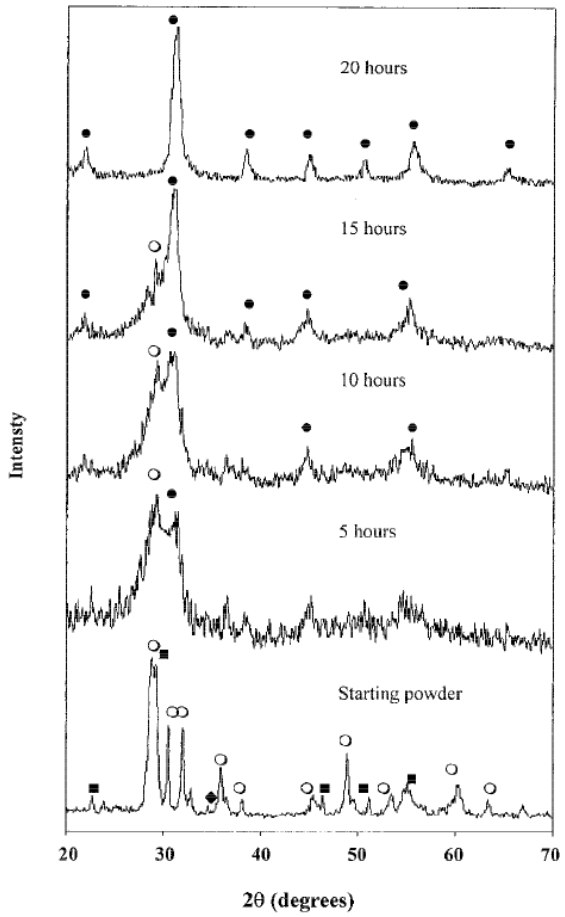
20 hours
15 hours
10 hours
5 hours
Starting powder
Intensty
20
30
40
50
60
70
2θ (degrees)

Fig. 34

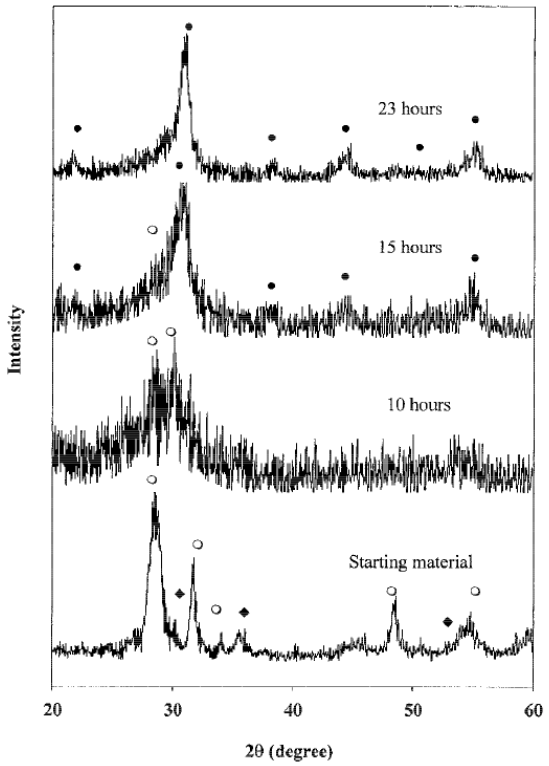
23 hours
15 hours
10 hours
Starting material
Intensity
20
30
40
50
60
2θ (degree)

Fig. 35

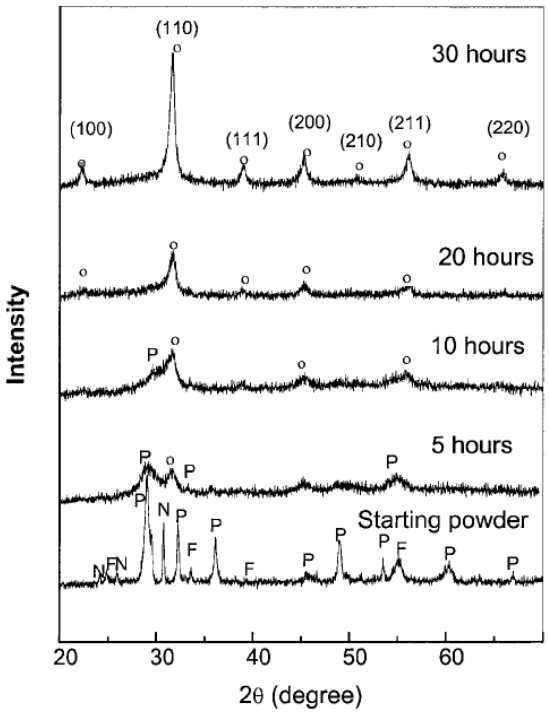
(110)
30 hours
(100)
(111)
(200)
(210)
(211)
(220)
20 hours
10 hours
5 hours
Starting powder
Intensity
20
30
40
50
60
2θ (degree)

Fig. 36

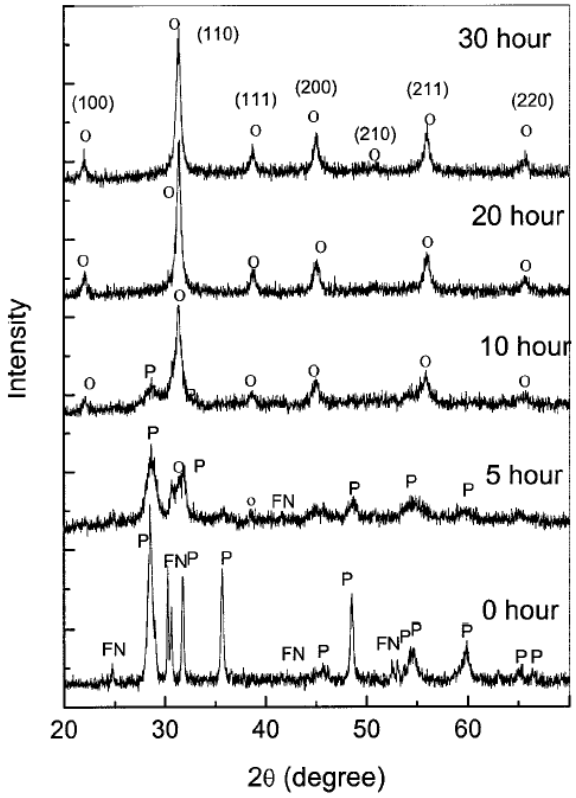
30 hour
20 hour
10 hour
5 hour
0 hour
(100)
(110)
(111)
(200)
(210)
(211)
(220)
O
P
FN
Intensity
20
30
40
50
60
2θ (degree)

Fig. 37

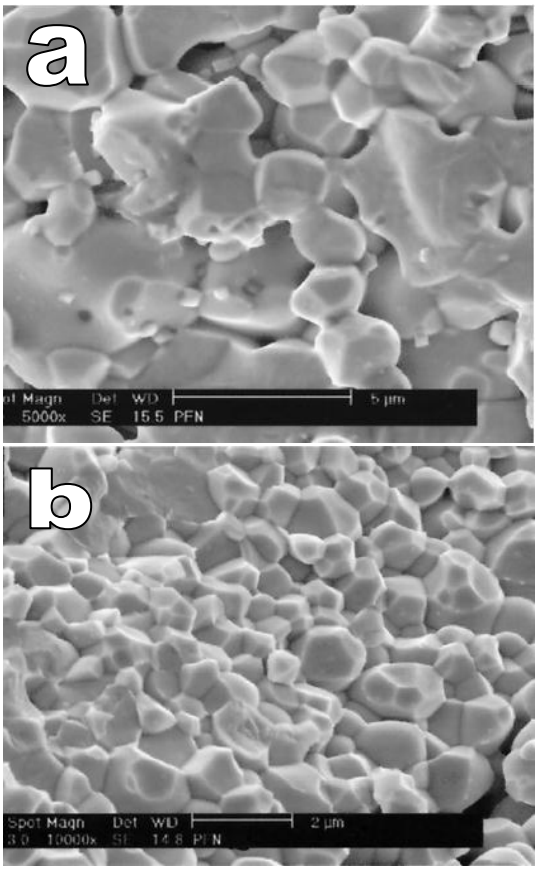
a
Magn Det WD 5 µm
5000x SE 15.5 PFN
b
Spot Magn Det WD 2 µm
3.0 10000x SE 14.8 PFN

Fig. 38

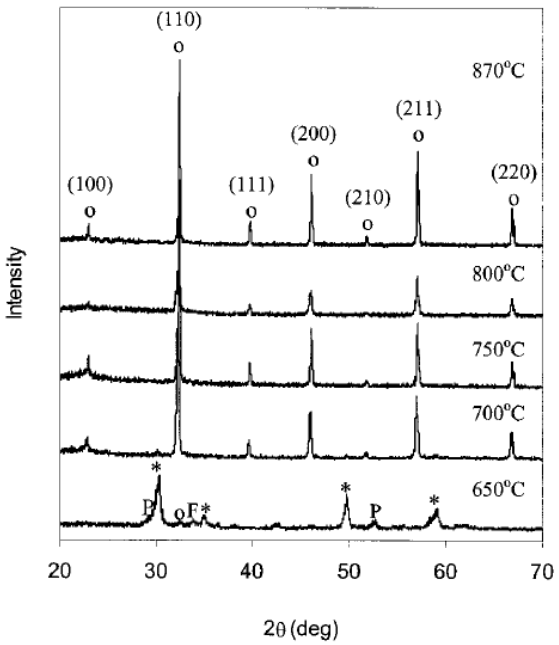
(110)
o
870°C
(211)
o
(200)
o
(100)
o
(111)
o
(210)
o
(220)
o
800°C
750°C
700°C
650°C
Intensity
20
30
40
50
60
70
2θ (deg)

Fig. 39

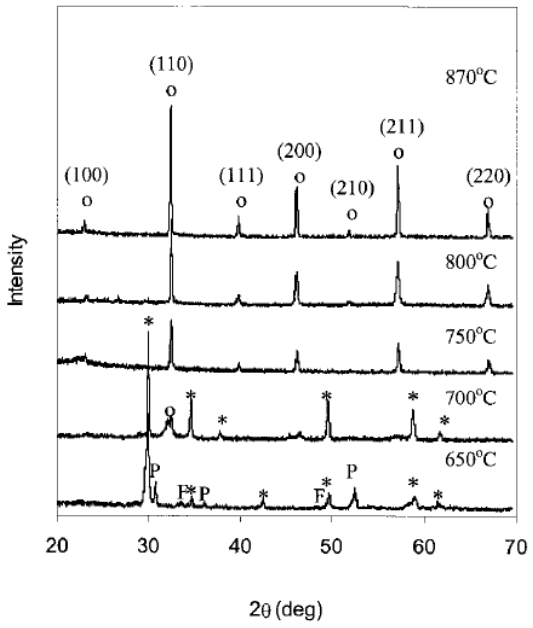
(110)
o
870°C
(211)
o
(200)
o
(100)
o
(111)
o
(210)
o
(220)
o
800°C
750°C
700°C
650°C
Intensity
20
30
40
50
60
70
2θ (deg)

Fig. 40

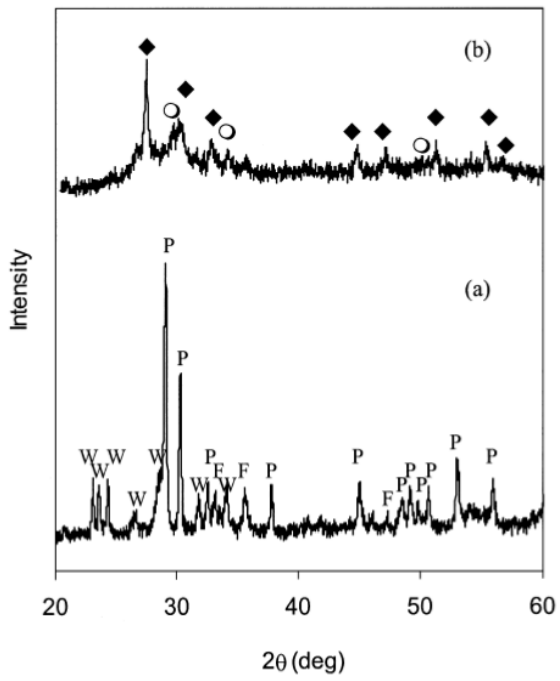
(b)
(a)
Intensity
2θ (deg)
20
30
40
50
60

Fig. 41

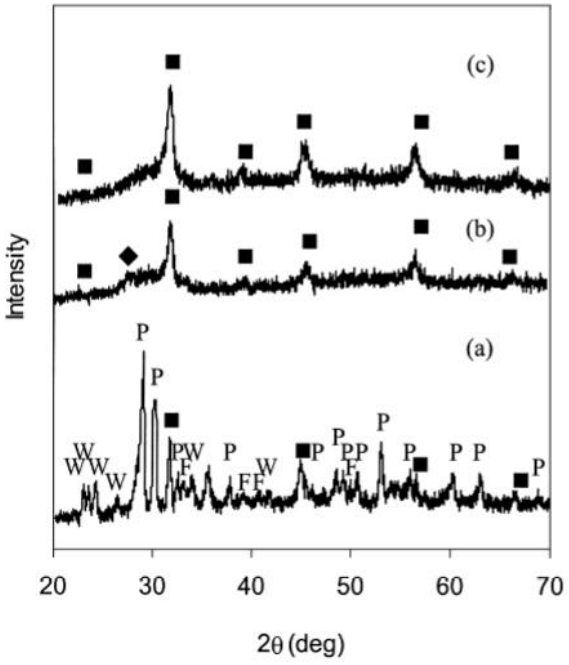
(c)
(b)
(a)
Intensity
2θ (deg)
20
30
40
50
60
70

Fig. 42

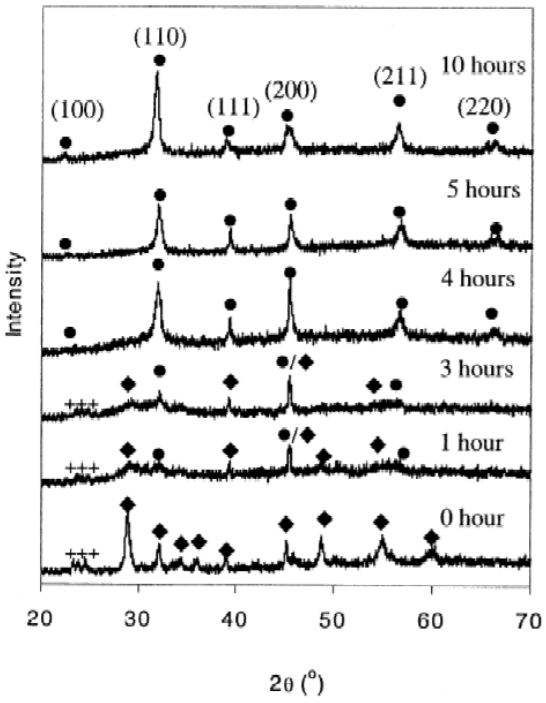
(110)
(100)
(111)
(200)
(211)
(220)
10 hours
5 hours
4 hours
3 hours
1 hour
0 hour
Intensity
20
30
40
50
60
70
2θ (°)

Fig. 43

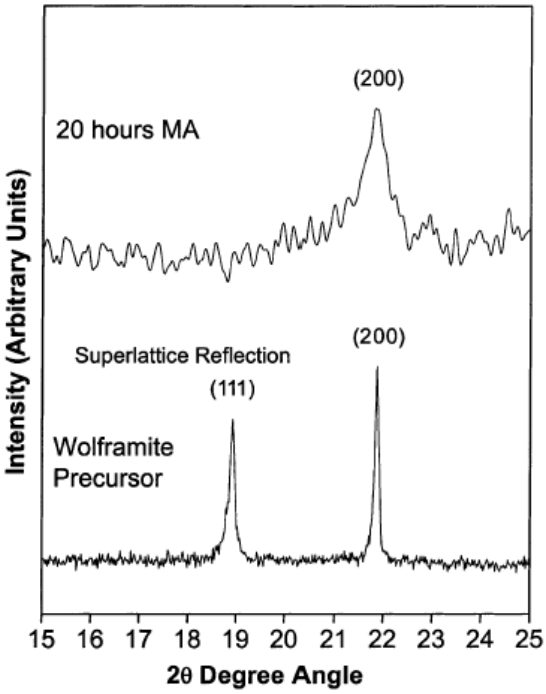
(200)
20 hours MA
Superlattice Reflection
(111)
(200)
Wolframite
Precursor
Intensity (Arbitrary Units)
15
16
17
18
19
20
21
22
23
24
25
2θ Degree Angle

Fig. 44

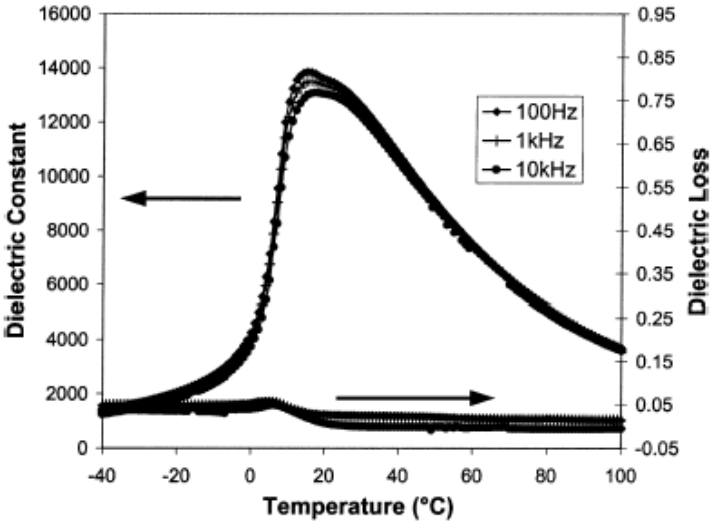
Dielectric Constant
Dielectric Loss
Temperature (°C)
100Hz
1kHz
10kHz
16000
14000
12000
10000
8000
6000
4000
2000
0
0.95
0.85
0.75
0.65
0.55
0.45
0.35
0.25
0.15
0.05
-0.05
-40
-20
0
20
40
60
80
100

Fig. 45

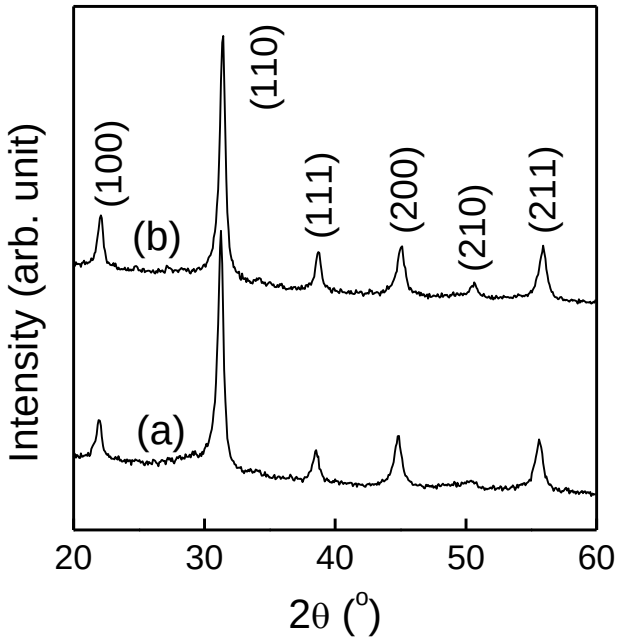
Intensity (arb. unit)
2θ (°)
(100)
(110)
(111)
(200)
(210)
(211)
(b)
(a)
20
30
40
50
60

Fig. 46

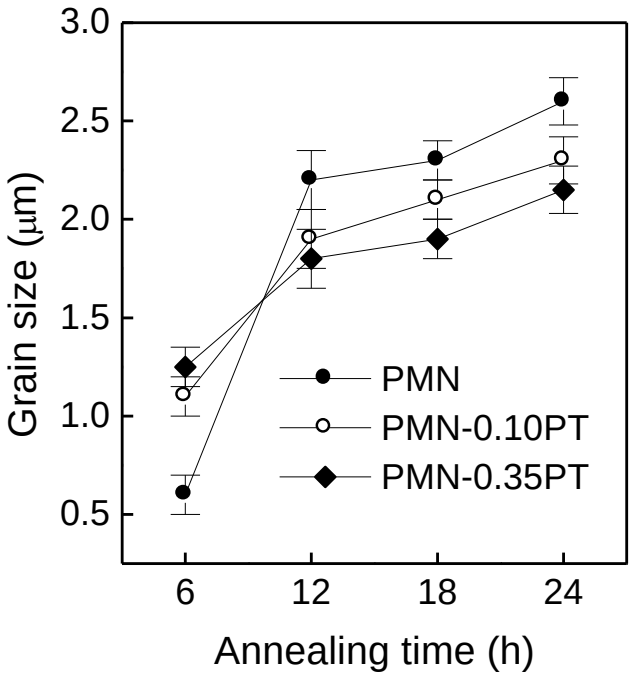
3.0
2.5
2.0
1.5
1.0
0.5
Grain size (μm)
6
12
18
24
Annealing time (h)
PMN
PMN-0.10PT
PMN-0.35PT

Fig. 47

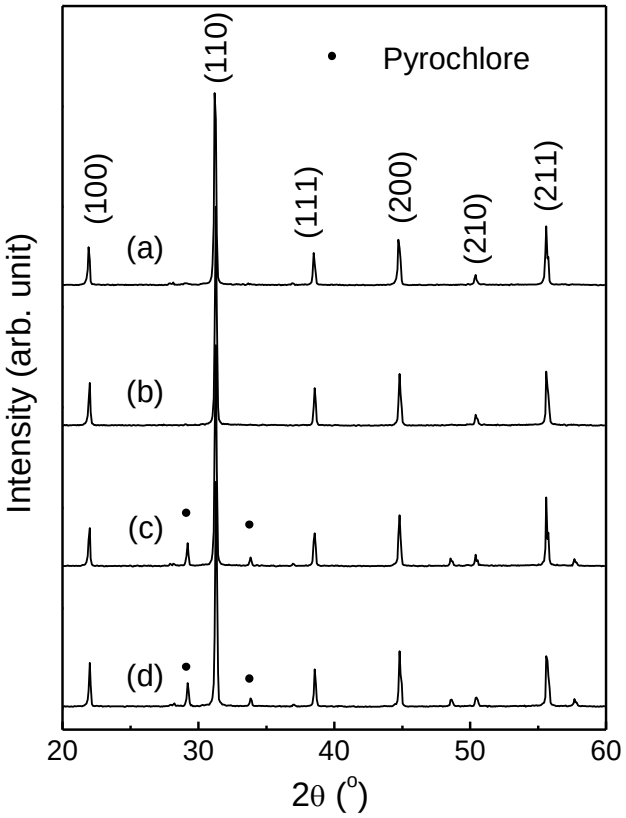
(110)
• Pyrochlore
(100)
(111)
(200)
(210)
(211)
(a)
(b)
(c)
(d)
Intensity (arb. unit)
20
30
40
50
60
2θ (°)

Fig. 48

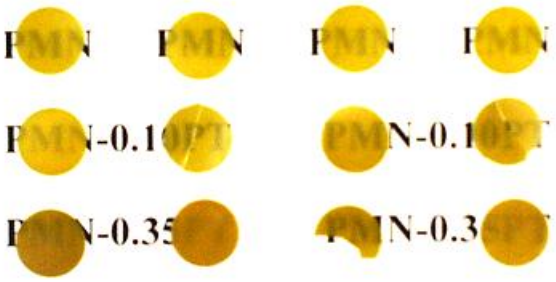
PMN
PMN
PMN
PMN
PMN-0.1
PMN-0.1
PMN-0.35
PMN-0.3

Fig. 49

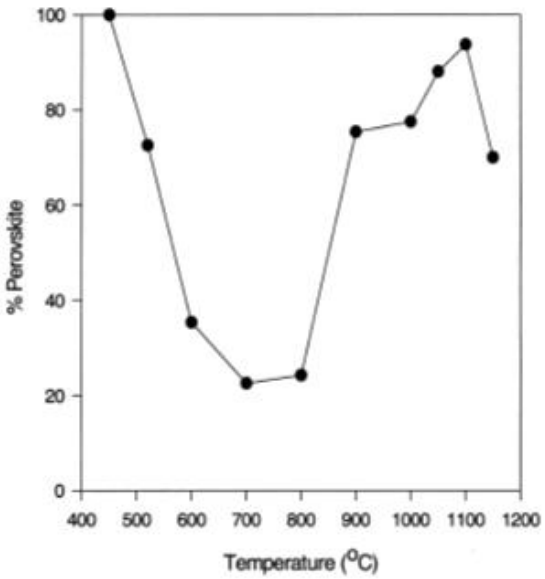
100
80
60
40
20
0
% Perovskite
400
500
600
700
800
900
1000
1100
1200
Temperature (°C)

Fig. 50

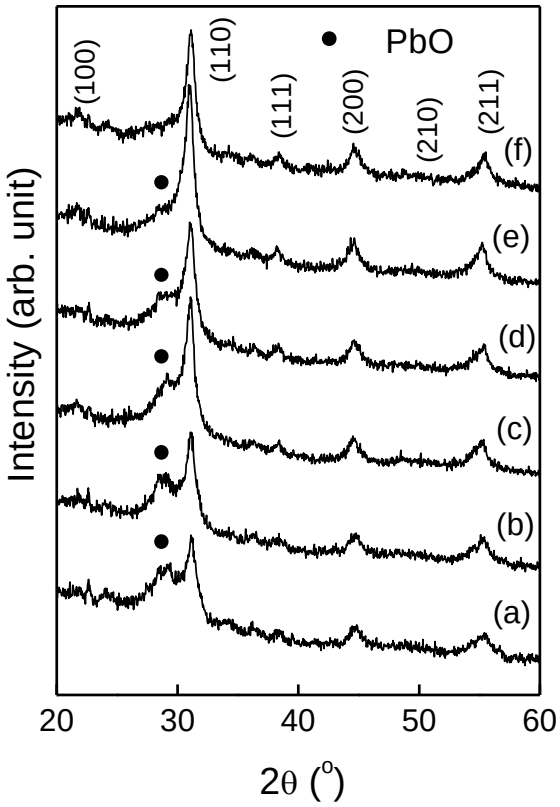
PbO
(100)
(110)
(111)
(200)
(210)
(211)
(f)
(e)
(d)
(c)
(b)
(a)
Intensity (arb. unit)
20
30
40
50
60
2θ (°)

Fig. 51

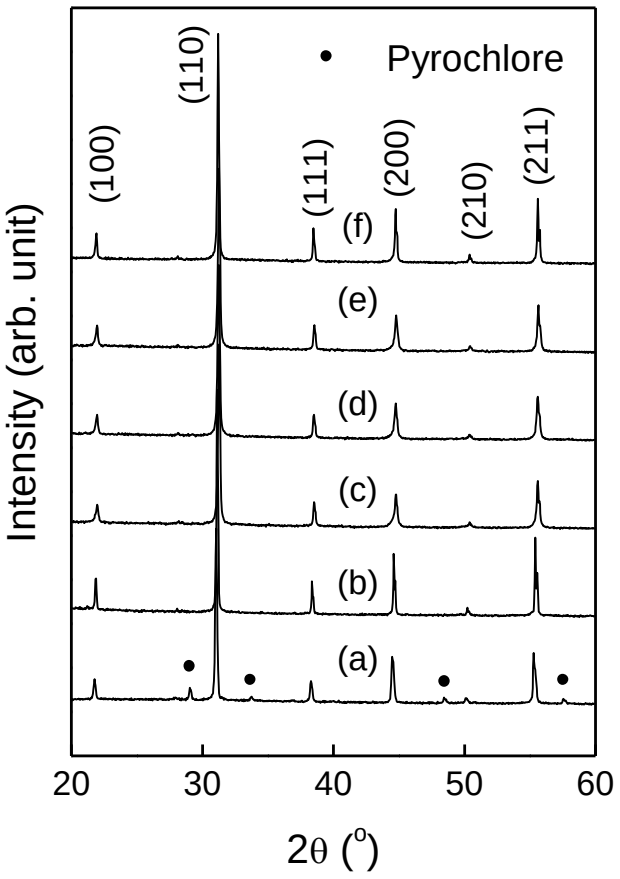
Pyrochlore
(100)
(110)
(111)
(200)
(210)
(211)
(f)
(e)
(d)
(c)
(b)
(a)
Intensity (arb. unit)
20
30
40
50
60
2θ (°)

Fig. 52

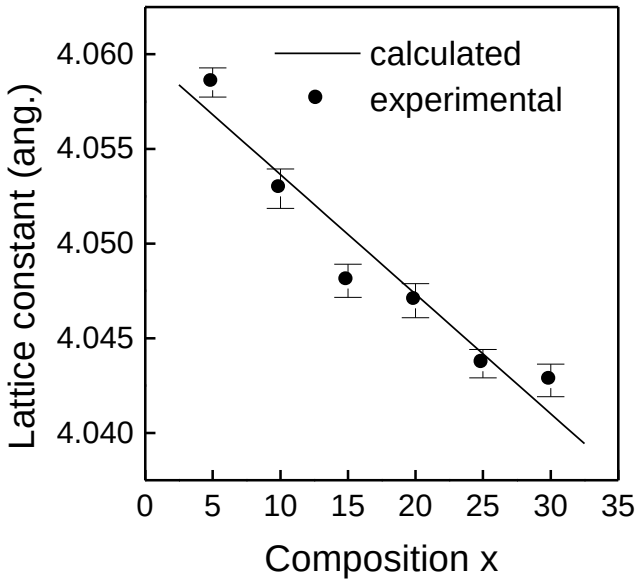
calculated
experimental
Lattice constant (ang.)
4.060
4.055
4.050
4.045
4.040
0
5
10
15
20
25
30
35
Composition x

Fig. 53

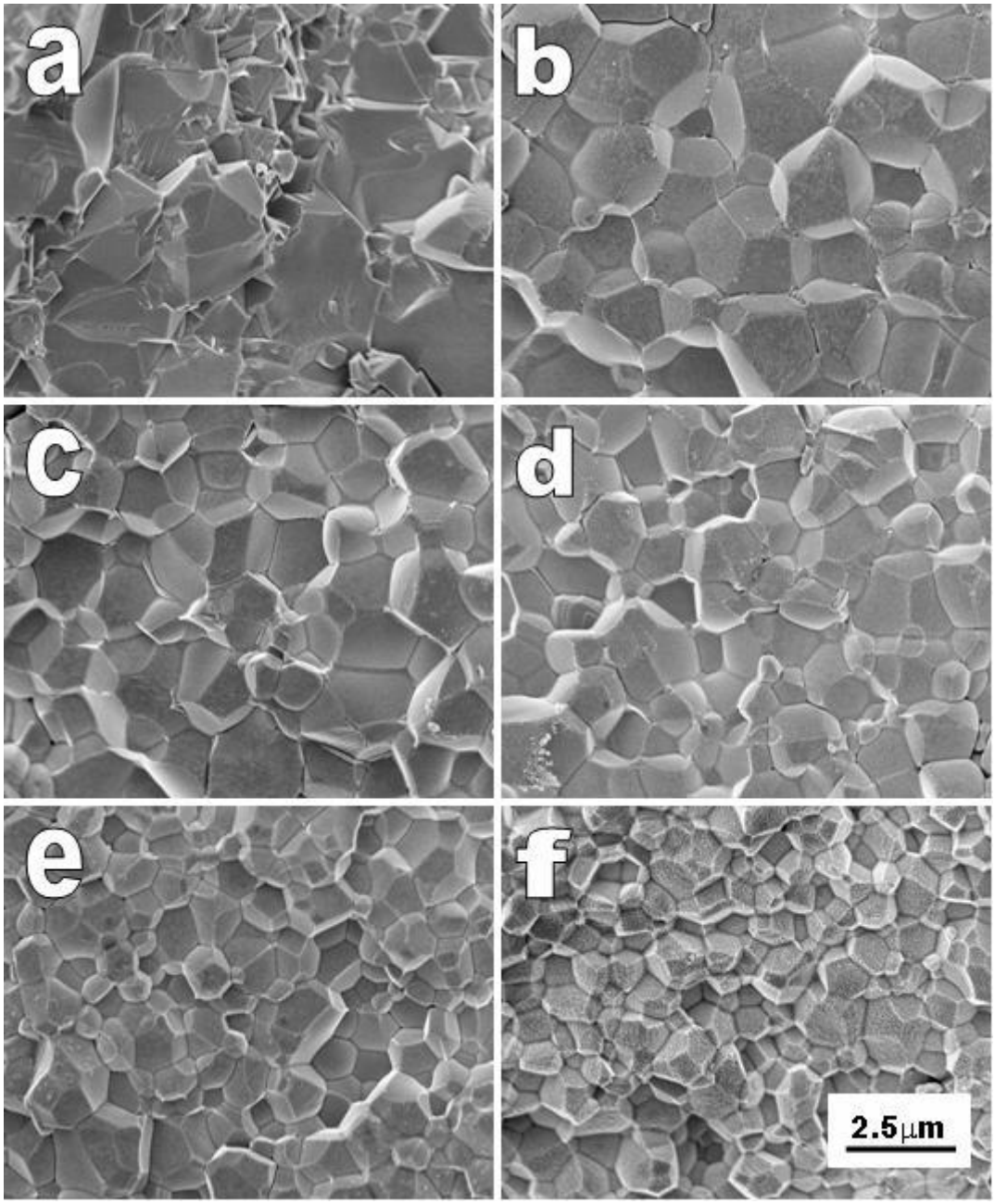

Fig. 54

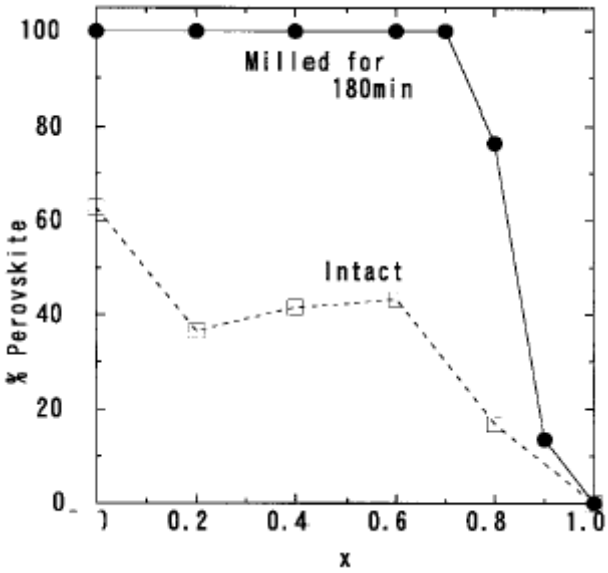
100
80
60
40
20
0
% Perovskite
Milled for
180min
Intact
0.2
0.4
0.6
0.8
1.0
x

Fig. 55

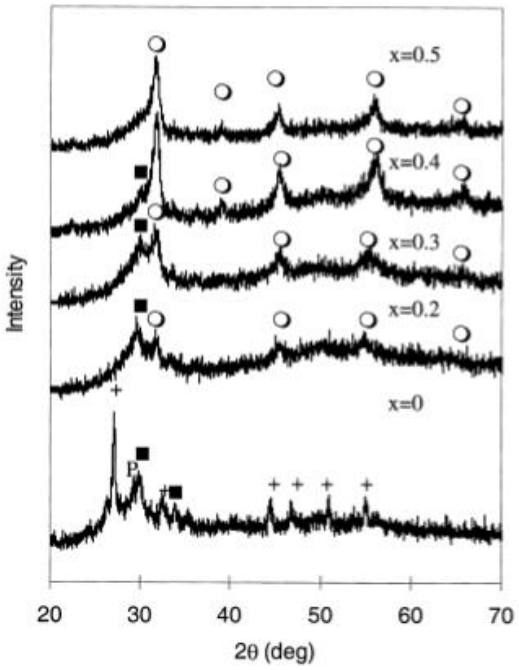
x=0.5
x=0.4
x=0.3
x=0.2
x=0
Intensity
20
30
40
50
60
70
2θ (deg)

Fig. 56

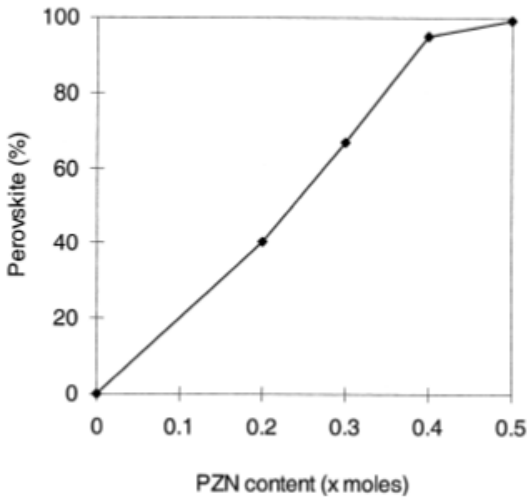

Fig. 57

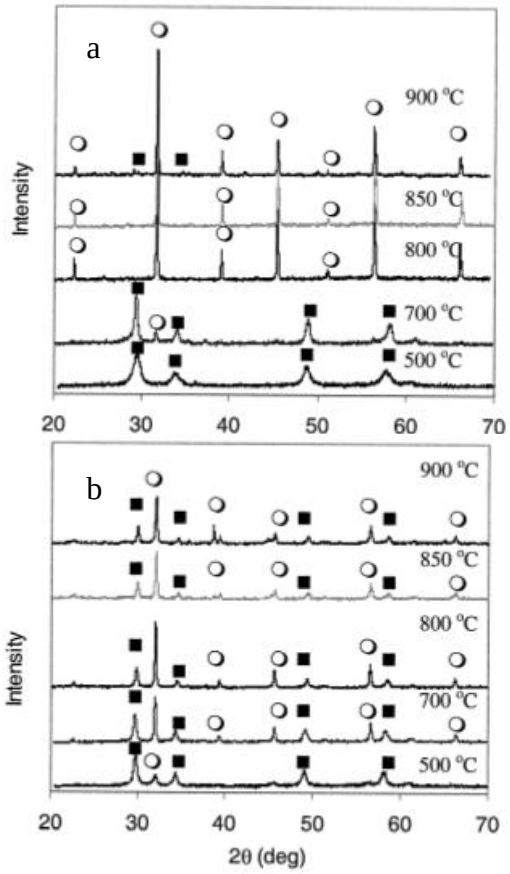
a
900 °C
850 °C
800 °C
700 °C
500 °C
Intensity
20
30
40
50
60
70
b
900 °C
850 °C
800 °C
700 °C
500 °C
Intensity
20
30
40
50
60
70
2θ (deg)

Fig. 58

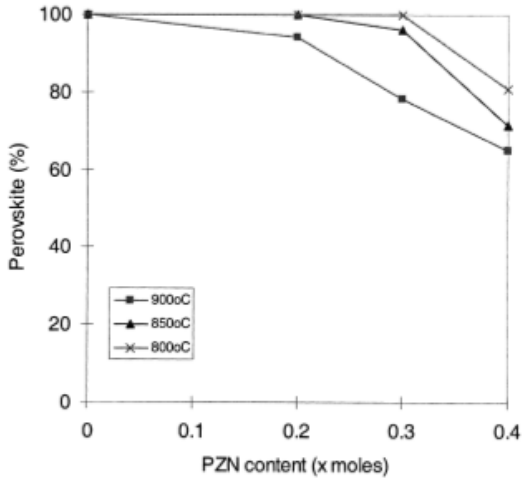
100
80
60
40
20
0
Perovskite (%)
900oC
850oC
800oC
0
0.1
0.2
0.3
0.4
PZN content (x moles)

Fig. 59

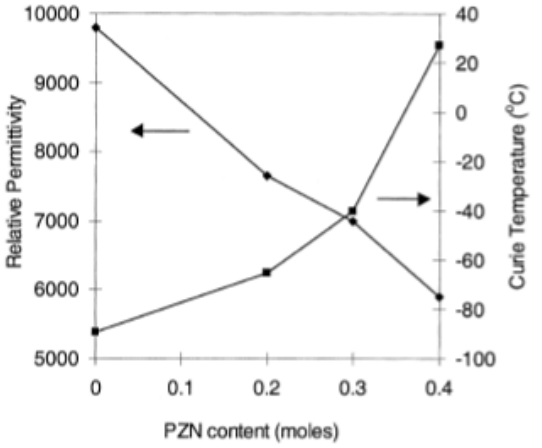
10000
9000
8000
7000
6000
5000
Relative Permittivity
40
20
0
-20
-40
-60
-80
-100
Curie Temperature (°C)
0
0.1
0.2
0.3
0.4
PZN content (moles)

Fig. 60

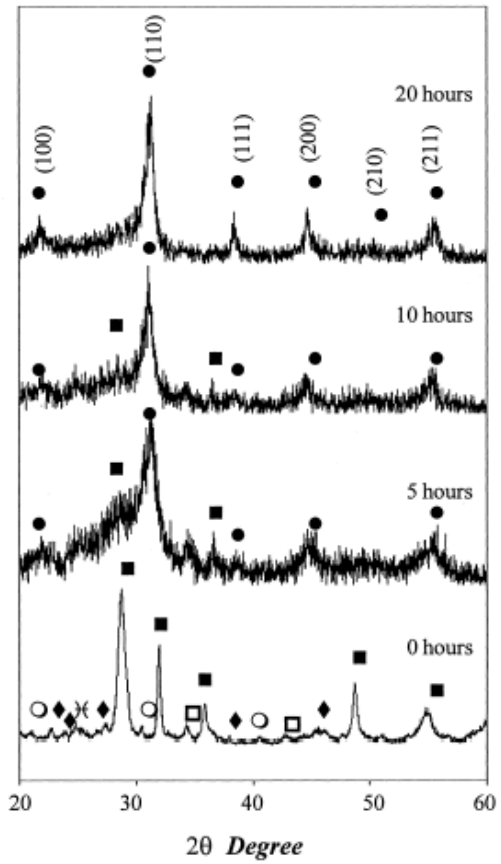
(110)
(100)
(111)
(200)
(210)
(211)
20 hours
10 hours
5 hours
0 hours
20
30
40
50
60
2θ Degree

Fig. 61

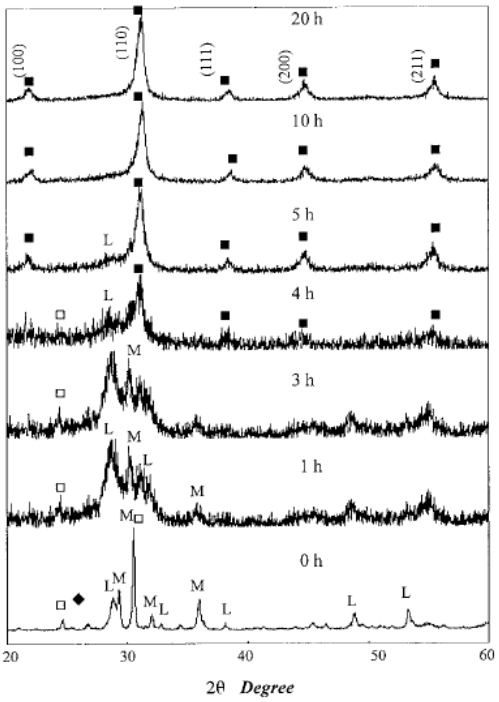
20 h
(100)
(110)
(111)
(200)
(211)
10 h
5 h
L
4 h
L
M
3 h
L
M
1 h
L
M
M
0 h
L
M
M
L
M
L
L
L
20
30
40
50
60
2θ Degree

Fig. 62

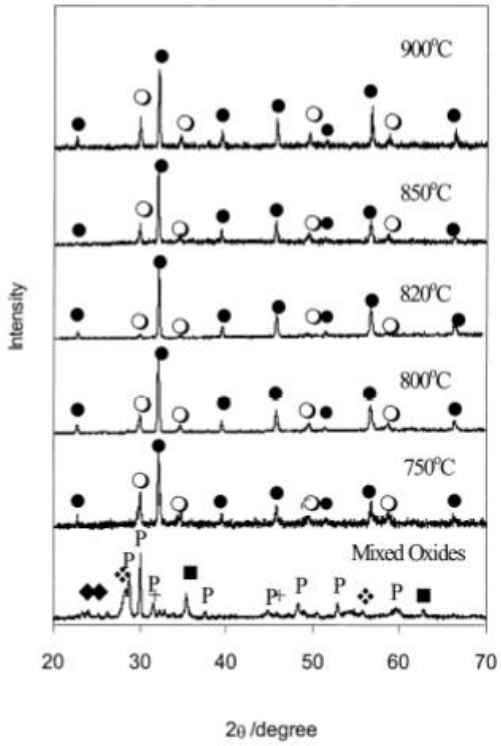
900°C
850°C
820°C
800°C
750°C
Mixed Oxides
Intensity
20
30
40
50
60
70
2θ /degree

Fig. 63

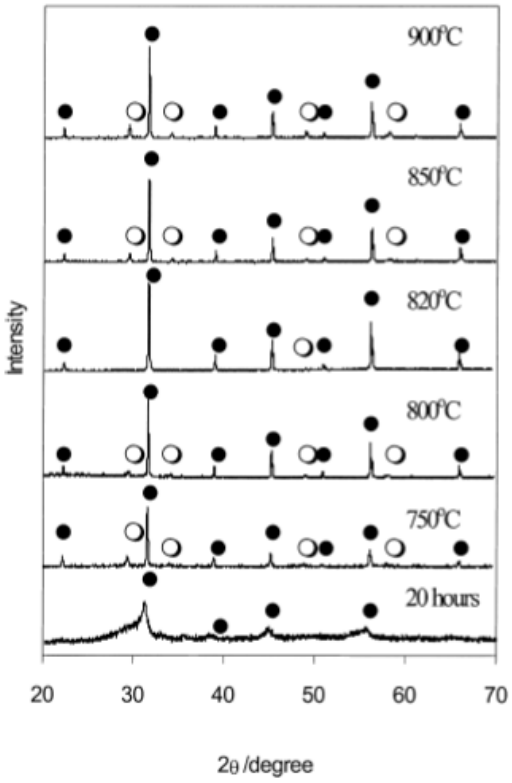
900°C
850°C
820°C
800°C
750°C
20 hours
Intensity
20
30
40
50
60
70
2θ /degree

Fig. 64

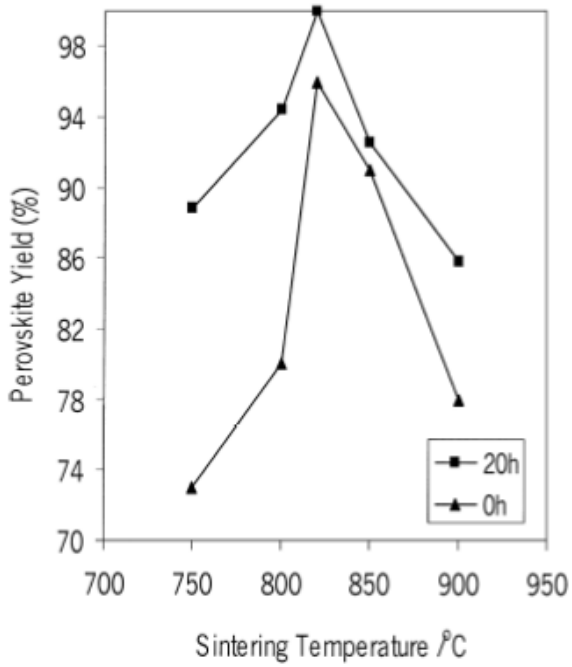
Perovskite Yield (%)
98
94
90
86
82
78
74
70
700
750
800
850
900
950
Sintering Temperature /°C
20h
0h

Fig. 65

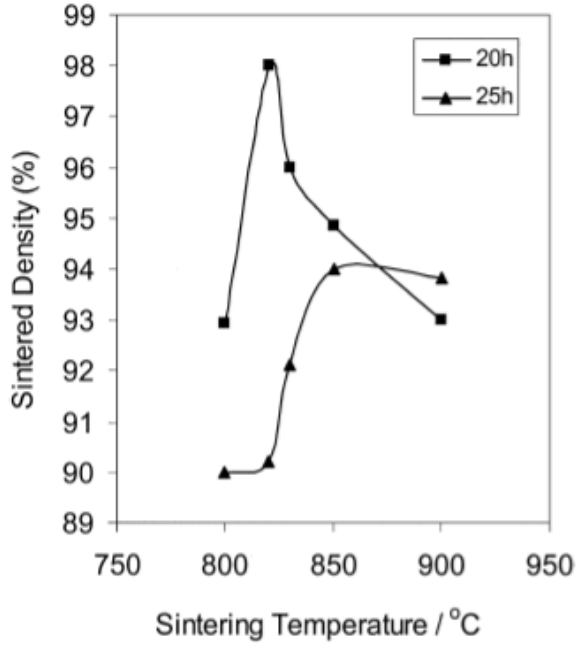
Sintered Density (%)
99
98
97
96
95
94
93
92
91
90
89
750
800
850
900
950
Sintering Temperature / °C
20h
25h

Fig. 66

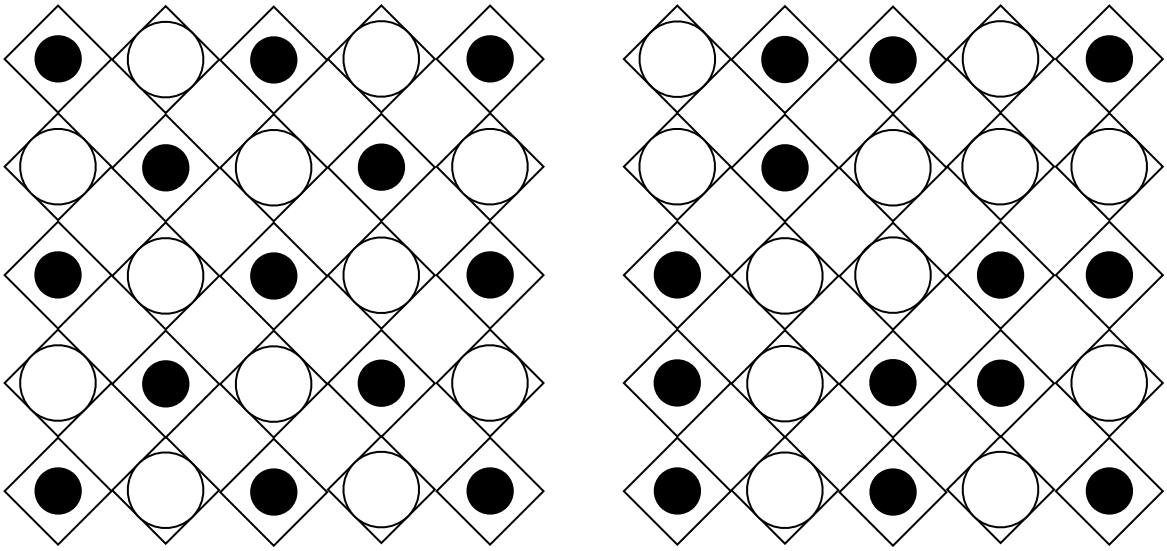

(a) Ordered (b) Disordered

Fig. 67

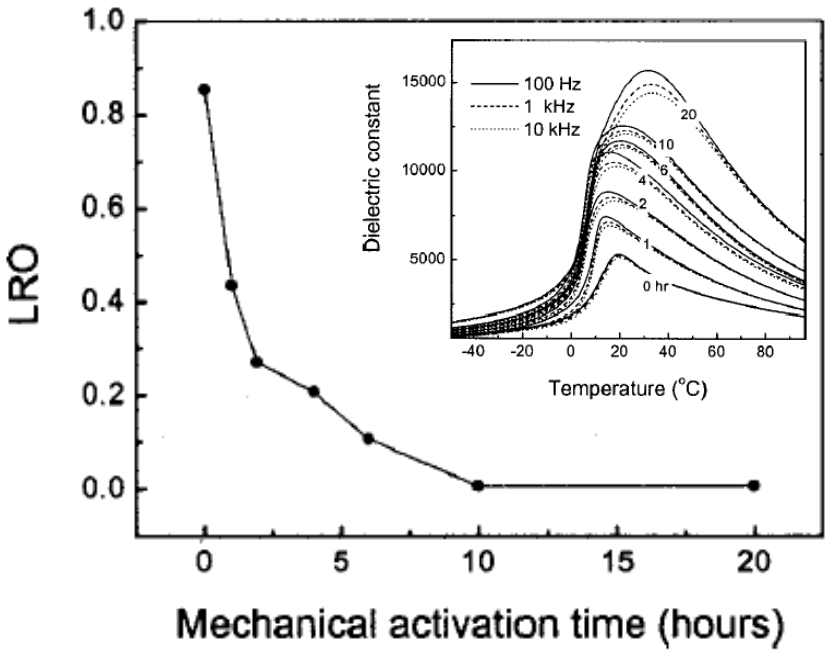

Fig. 68

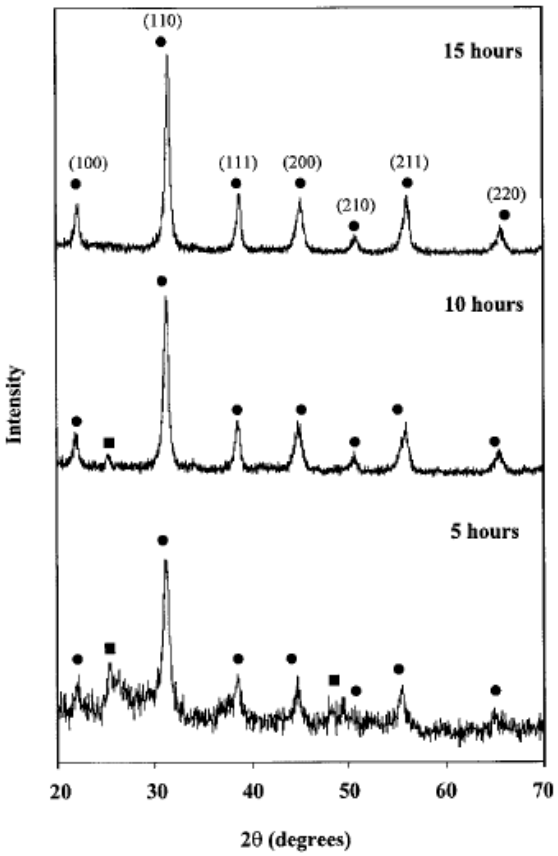
(110)
15 hours
(100)
(111)
(200)
(211)
(210)
(220)
10 hours
5 hours
Intensity
20
30
40
50
60
70
2θ (degrees)

Fig. 69

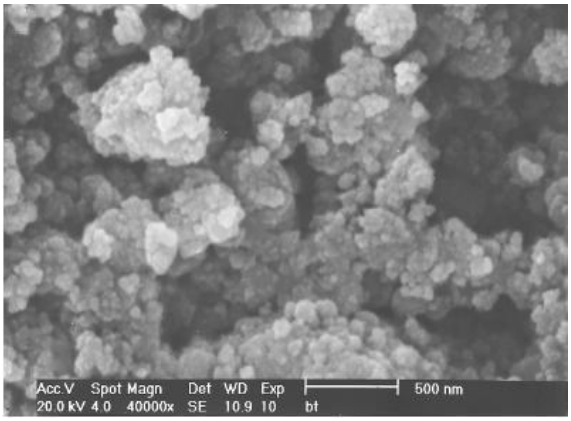
Acc.V Spot Magn Det WD Exp
20.0 kV 4.0 40000x SE 10.9 10
500 nm
bt

Fig. 70

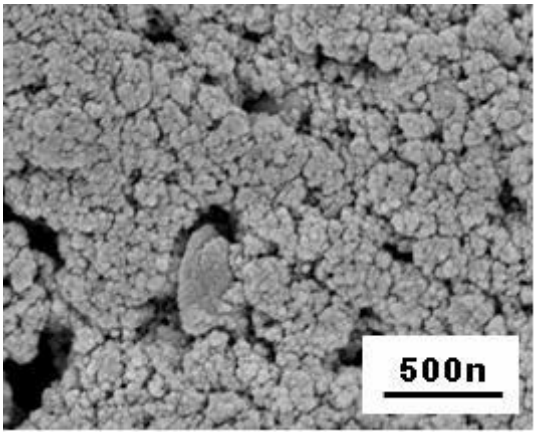
500n

Fig. 71

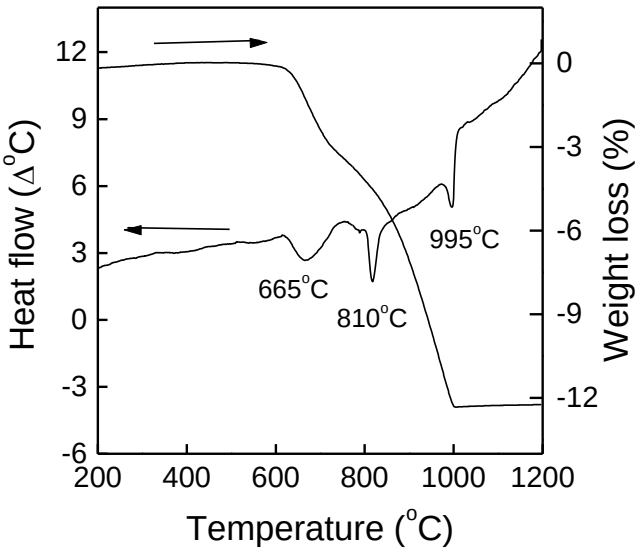
Heat flow (ΔoC)
Weight loss (%)
Temperature (oC)
665oC
810oC
995oC
12
9
6
3
0
-3
-6
0
-3
-6
-9
-12
200
400
600
800
1000
1200

Fig. 72

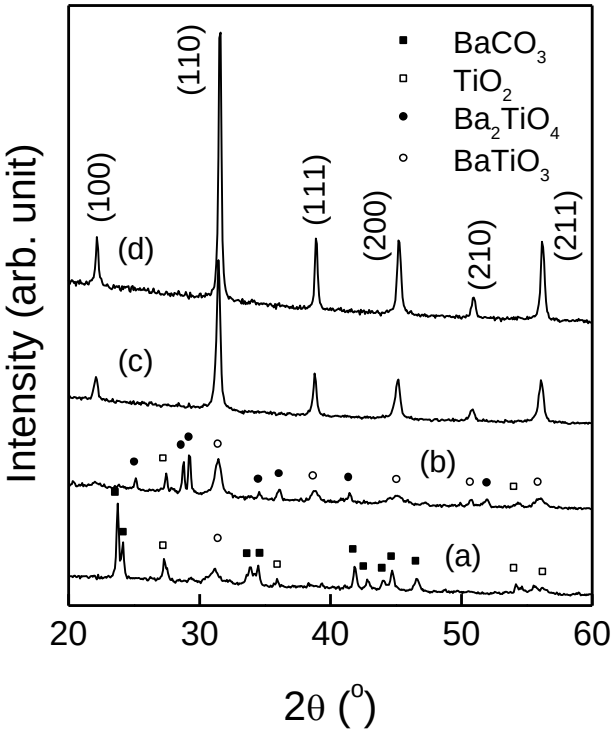
BaCO3
TiO2
Ba2TiO4
BaTiO3
(100)
(110)
(111)
(200)
(210)
(211)
(d)
(c)
(b)
(a)
Intensity (arb. unit)
2θ (o)
20
30
40
50
60

Fig. 73

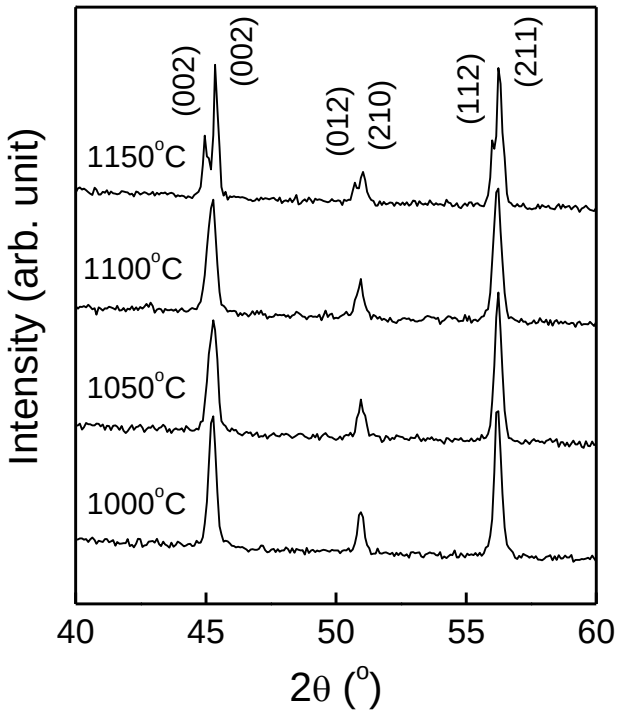
(002)
(002)
(012)
(210)
(112)
(211)
1150°C
1100°C
1050°C
1000°C
Intensity (arb. unit)
40
45
50
55
60
2θ (°)

Fig. 74

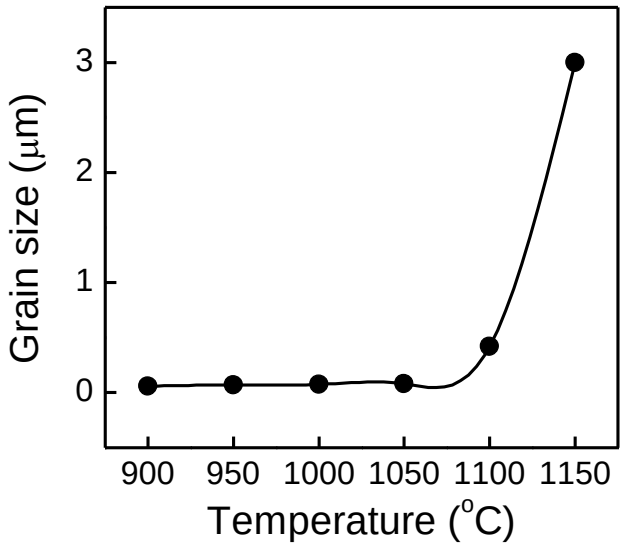
Grain size (μm)
0
1
2
3
900
950
1000
1050
1100
1150
Temperature (°C)

Fig. 75

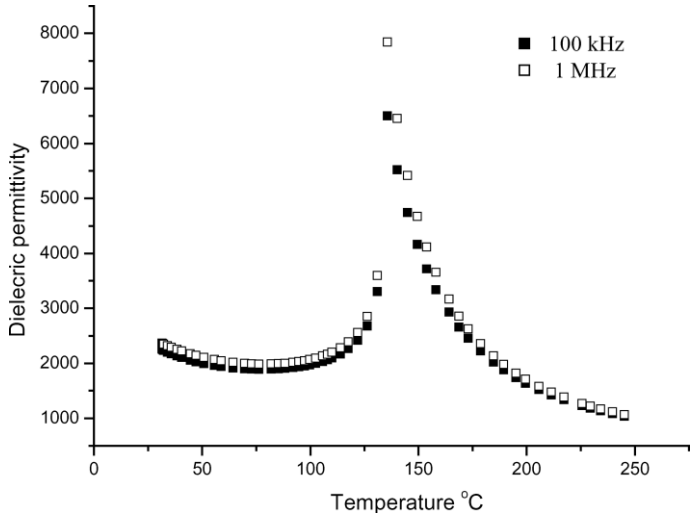
100 kHz
1 MHz
Dielecric permittivity
Temperature °C
8000
7000
6000
5000
4000
3000
2000
1000
0
50
100
150
200
250

Fig. 76

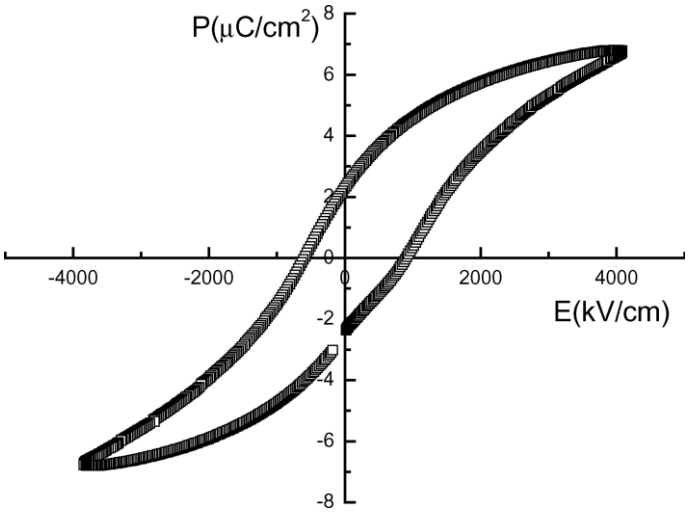
P(μC/cm²)
E(kV/cm)
8
6
4
2
0
-2
-4
-6
-8
-4000
-2000
0
2000
4000

Fig. 77

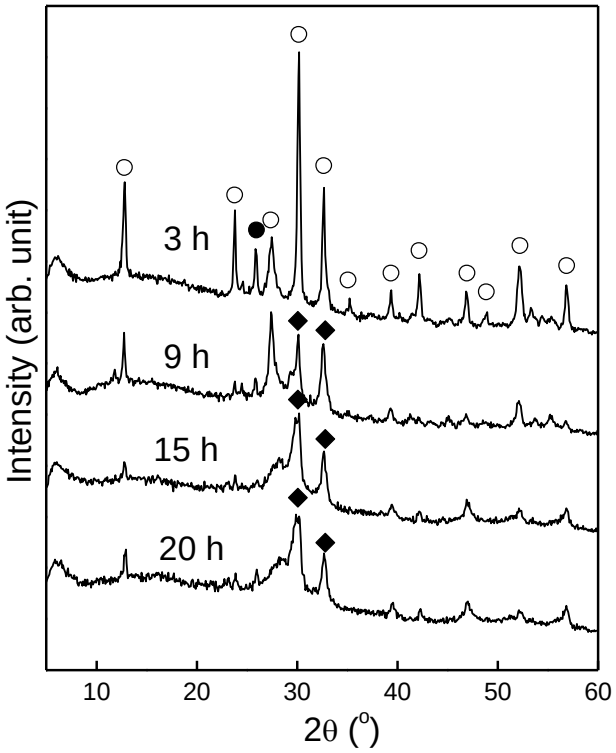
Intensity (arb. unit)
3 h
9 h
15 h
20 h
10
20
30
40
50
60
2θ (°)

Fig. 78

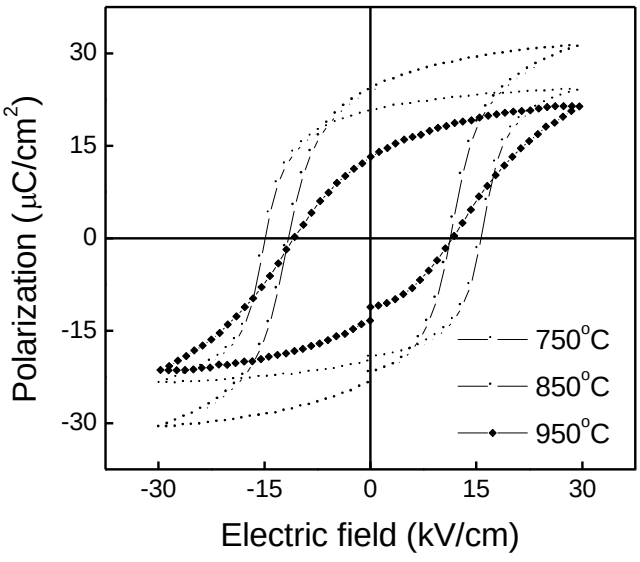
Polarization (μC/cm²)
30
15
0
-15
-30
750°C
850°C
950°C
-30
-15
0
15
30
Electric field (kV/cm)

Fig. 79

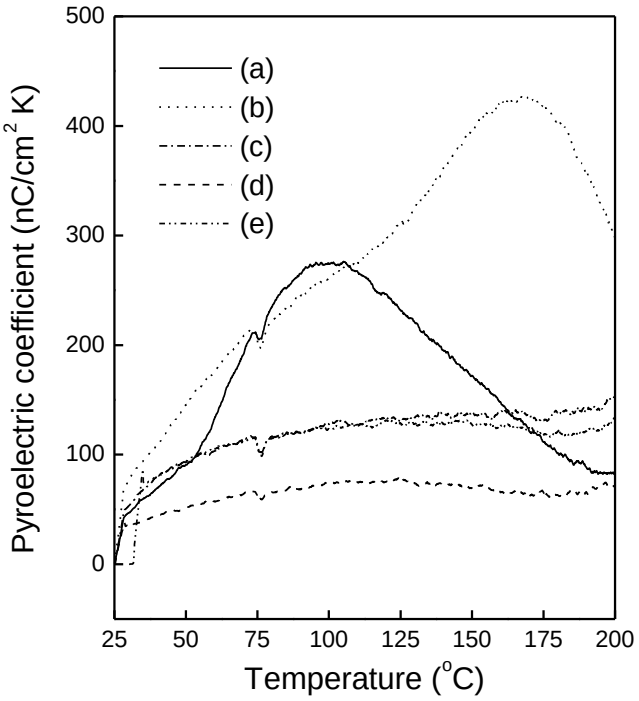
Pyroelectric coefficient (nC/cm^2 K)
Temperature (^{o}C)
(a)
(b)
(c)
(d)
(e)
500
400
300
200
100
0
25
50
75
100
125
150
175
200

Fig. 80

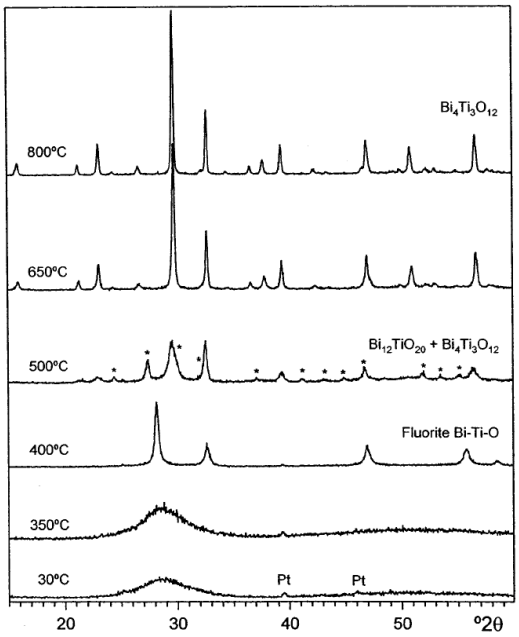
$Bi_4Ti_3O_{12}$
800°C
650°C
$Bi_{12}TiO_{20}$ + $Bi_4Ti_3O_{12}$
500°C
Fluorite Bi-Ti-O
400°C
350°C
30°C
Pt
Pt
20
30
40
50
°2θ

Fig. 81

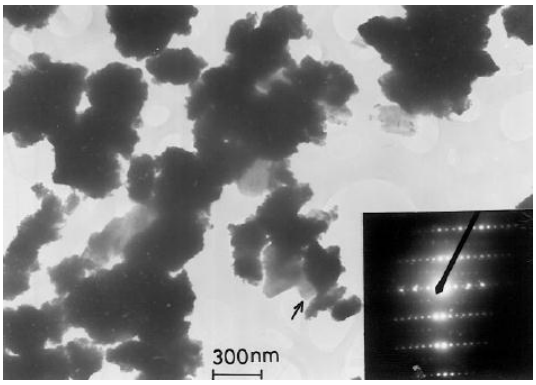
300nm

Fig. 82

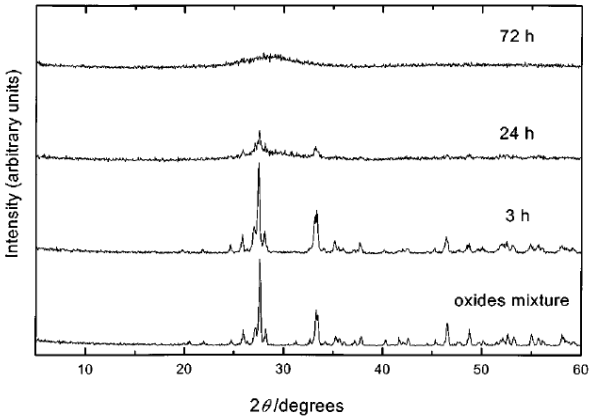
72 h
24 h
3 h
oxides mixture
Intensity (arbitrary units)
10
20
30
40
50
60
2θ/degrees

Fig. 83

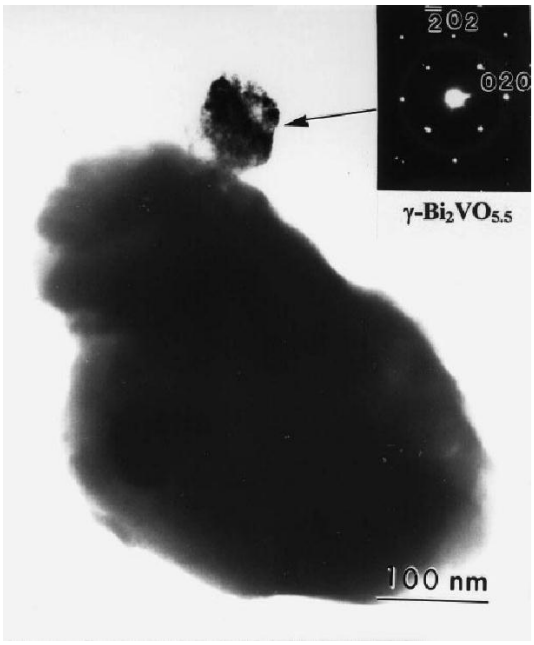

Fig. 84

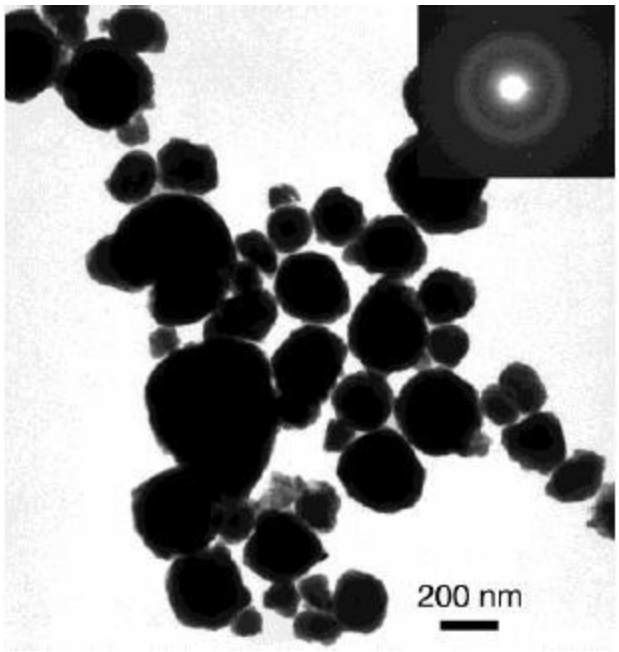

Fig. 85

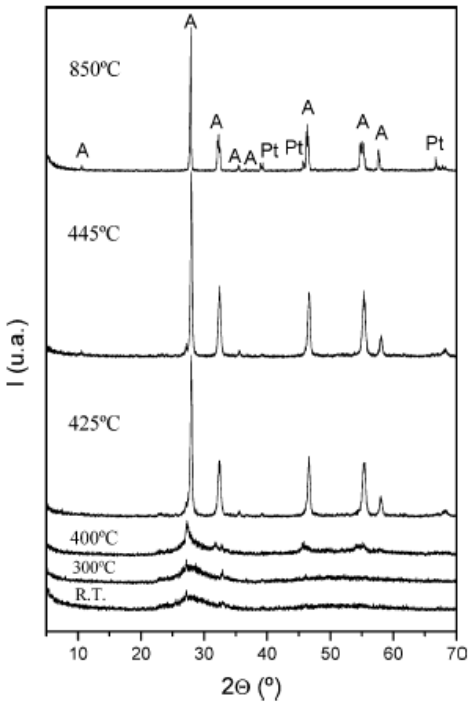
850ºC
445ºC
425ºC
400ºC
300ºC
R.T.
A
A
A
A
A
A
Pt
Pt
Pt
I (u.a.)
10
20
30
40
50
60
70
2Θ (º)

Fig. 86

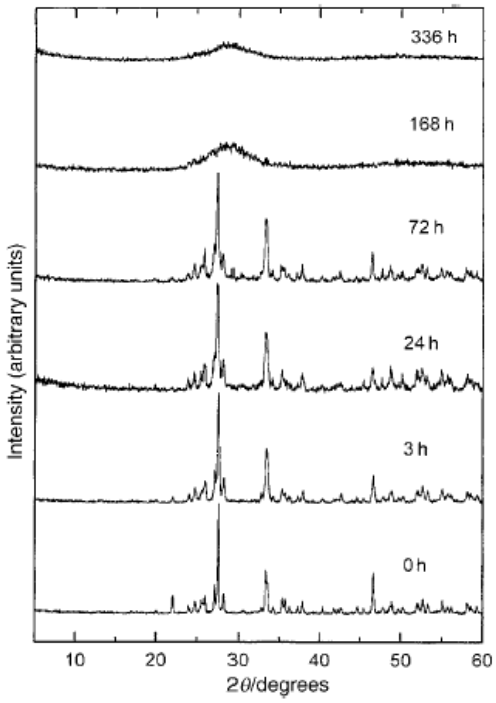
336 h
168 h
72 h
24 h
3 h
0 h
Intensity (arbitrary units)
10
20
30
40
50
60
2θ/degrees

Fig. 87

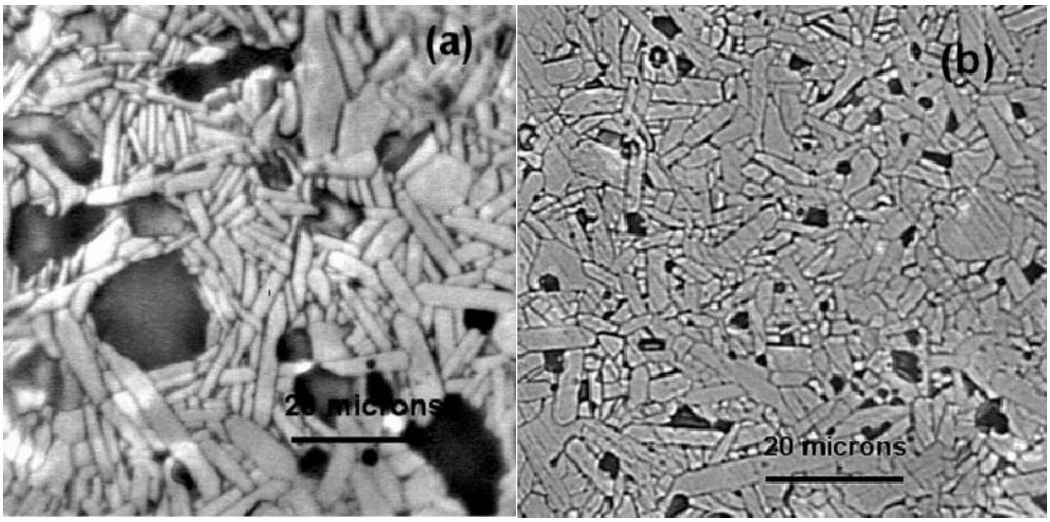

Fig. 88

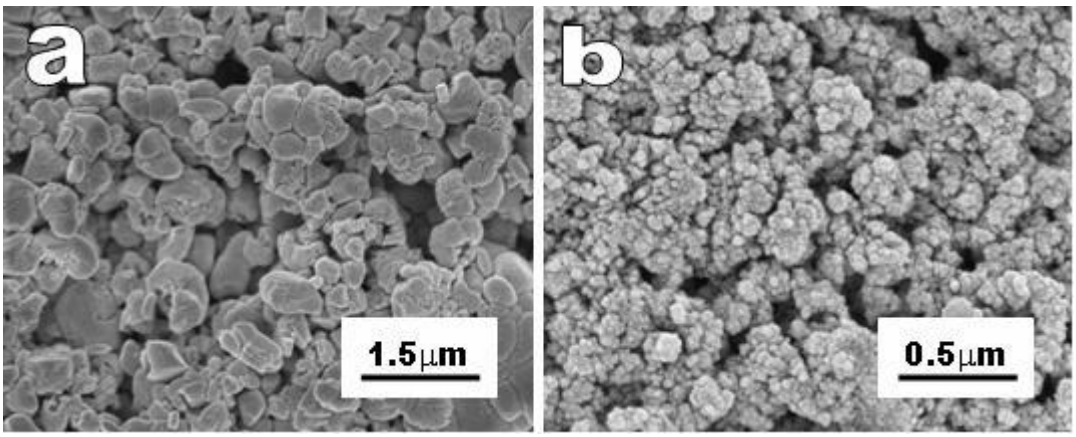

Fig. 89

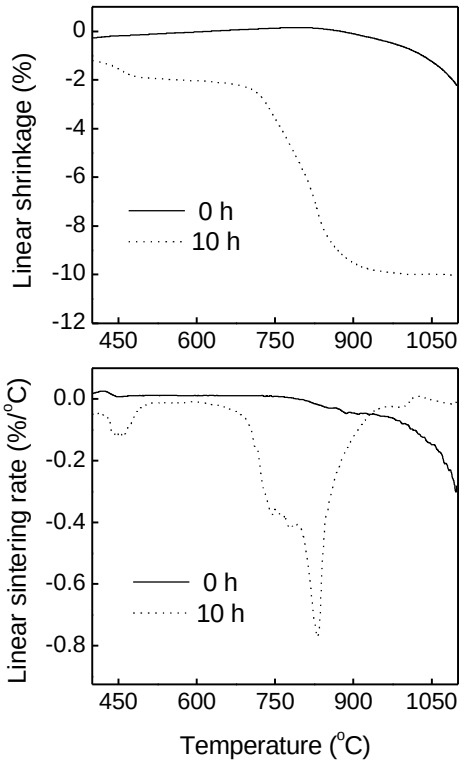
Linear shrinkage (%)
0
-2
-4
-6
-8
-10
-12
0 h
10 h
450
600
750
900
1050
Linear sintering rate (%/°C)
0.0
-0.2
-0.4
-0.6
-0.8
0 h
10 h
450
600
750
900
1050
Temperature (°C)

Fig. 90

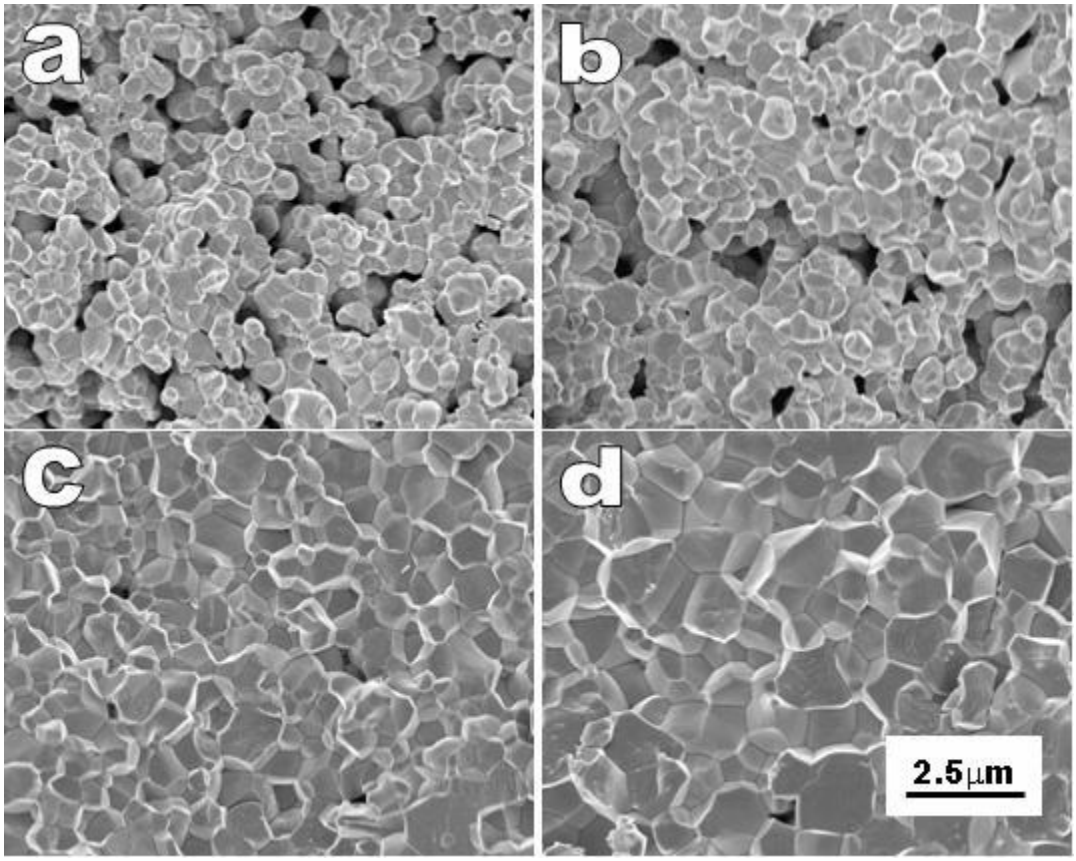

Fig. 91

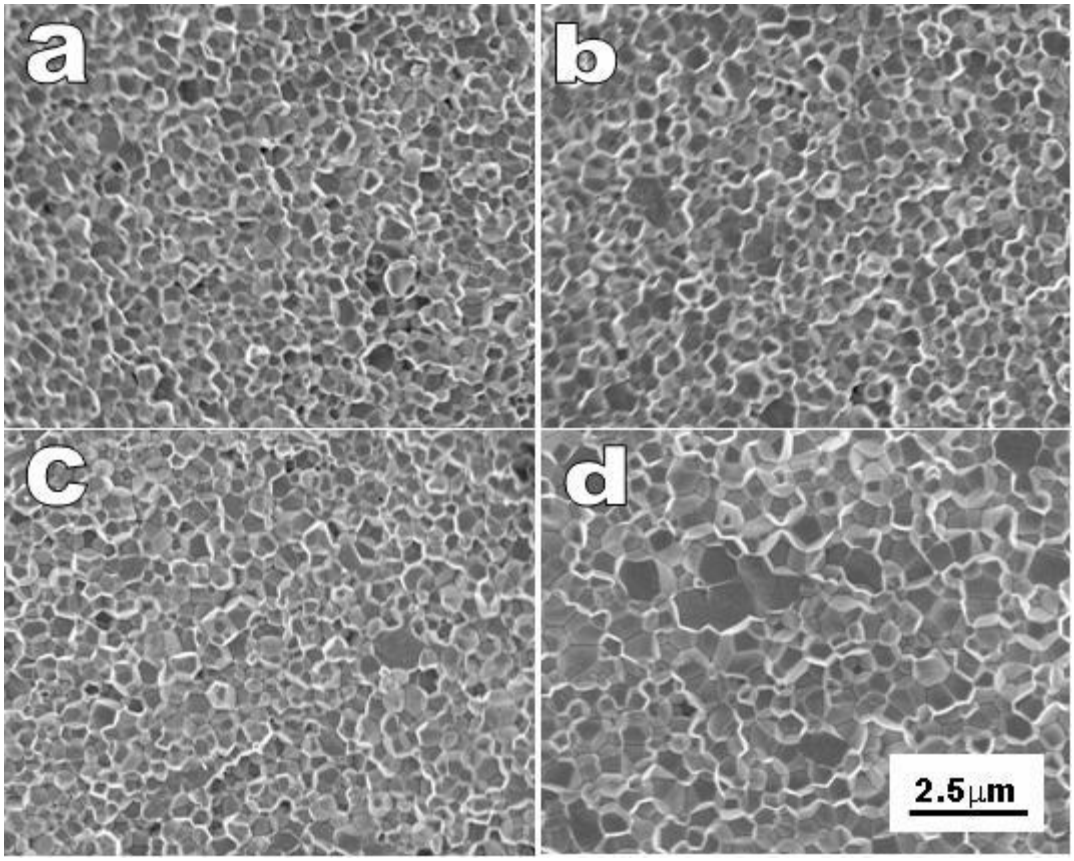

Fig. 92

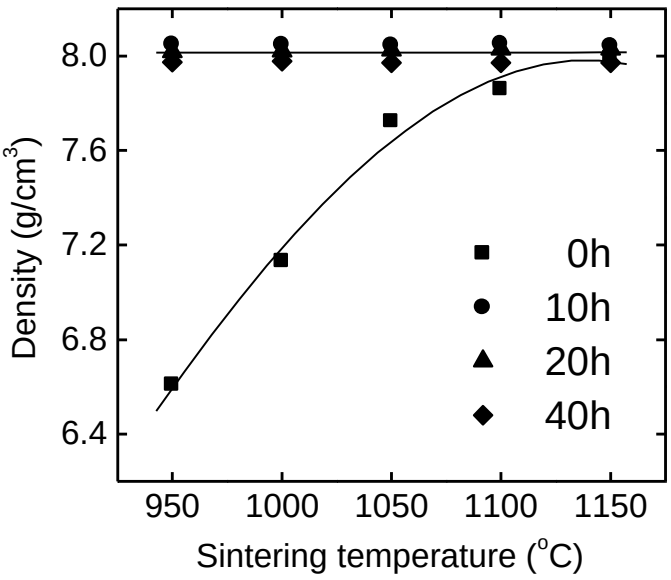
8.0
7.6
7.2
6.8
6.4
Density (g/cm3)
950
1000
1050
1100
1150
Sintering temperature (oC)
0h
10h
20h
40h

Fig. 93

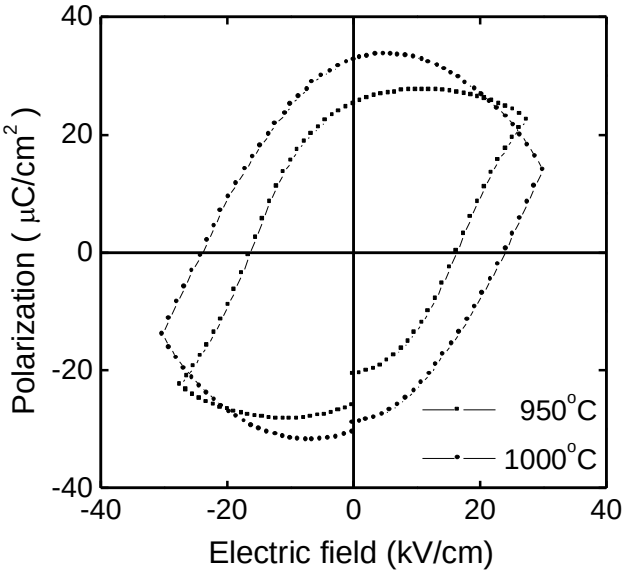
40
20
0
-20
-40
Polarization (μC/cm2)
-40
-20
0
20
40
Electric field (kV/cm)
950oC
1000oC

Fig. 94

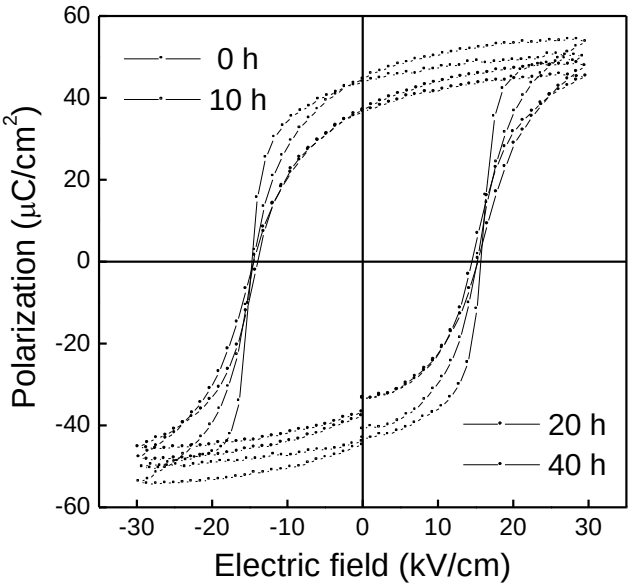
0 h
10 h
20 h
40 h
Polarization (μC/cm²)
Electric field (kV/cm)
60
40
20
0
-20
-40
-60
-30
-20
-10
0
10
20
30

Fig. 95

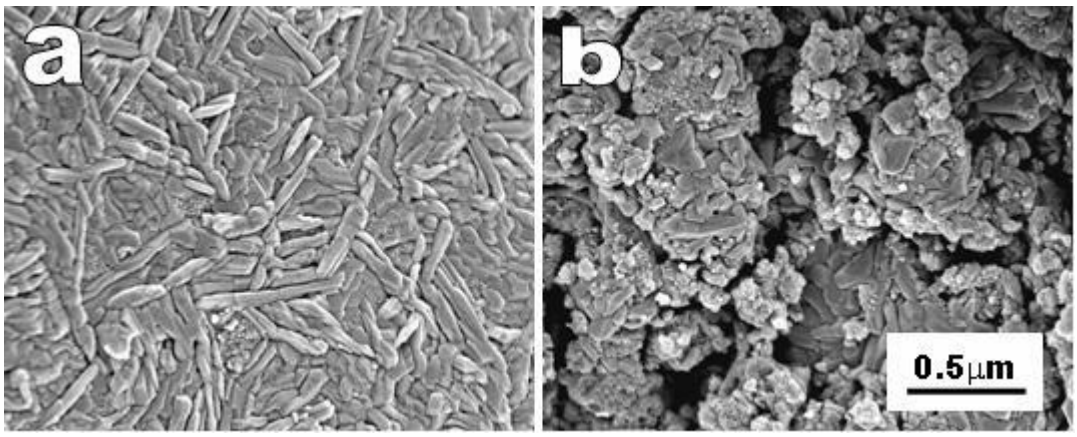
a
b
0.5μm

Fig. 96

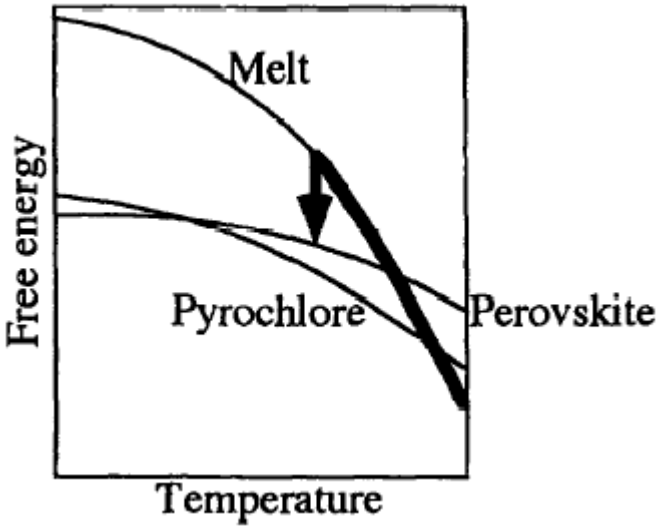

Fig. 97